U.PORTO
FEUP FACULDADE DE ENGENHARIA
UNIVERSIDADE DO PORTO

Departamento de Engenharia Mecânica

Design of a Belt Transmission Test Rig

Pedro José de Freitas

Porto 2018

Pedro José de Freitas

Design of a Belt Transmission Test Rig

Thesis submitted to the
Faculdade de Engenharia da Universidade do Porto
for the *Mestrado Integrado em Engenharia Mecânica*

Supervisor	Doctor Ramiro C. Martins
Co-supervisor	Doctor Carlos M. G. C. Fernandes
Co-supervisor	Professor Jorge H. O. Seabra

Departamento de Engenharia Mecânica
Faculdade de Engenharia
Universidade do Porto

The work presented in this dissertation was performed at CETRIB
Department of Mechanical Engineering
Faculty of Engineering
University of Porto
Porto, Portugal.

Pedro José de Freitas
E-mail: pjfreitas14@gmail.com

Faculdade de Engenharia da Universidade do Porto
Departamento de Engenharia Mecânica
CETRB

Rua Dr. Roberto Frias s/n, room M111
4200-465 Porto
Portugal

Acknowledgements

The past six months have been a period of intense learning for me, not only in the scientific arena, but also on a personal level. Writing this dissertation has had a big impact on me. I would like to reflect on the people who have supported and helped me throughout this period.

Foremost, I would like to express my gratitude to my supervisors Prof. Ramiro Martins, Prof. Carlos Fernandes and Prof. Jorge Seabra for giving me their continuous support, motivation, and immense knowledge that helped me during the research and writing of this thesis.

I would like to thank my mother Emília de Freitas for giving me the opportunity to study and for supporting me in my pursuits throughout my life.

I would like to thank my grandparents António de Freitas and Emília Pereira for their continuous support throughout my life.

My time at FEUP was made enjoyable in large part due to the friends that became a part of my life. I am grateful for the leisure time spent together.

Last but not least I would like to express my gratitude to CETRIB for providing a suitable workplace to carry out this work.

To my mother

Abstract

Power transmission efficiency relies on multiple variables such as mechanical transmissions. Belt transmissions are a source of power loss many times underestimated, and therefore constitutes an area where improvements can have significant impacts. The losses of power in belts transmission generated by multiple factors such as excessive pretension, misalignments, small pulleys, etc.

In this purpose, CETRIB Unidade de Tribologia, Vibrações e Manutenção Industrual has interest in manufacturing a test bench to evaluate these losses under different operating conditions.

This thesis describes the mechanical design of a belt transmission test bench.

Objectively, this test bench measures the torque and speed applied to the input and output shafts of the belts transmission. With these values it is possible to compute the power loss.

Optibelt belt transmission components were used as reference because of their worldwide presence.

After a review of mechanical power transmission test rigs, it was concluded that a test rig with a closed mechanical power circuit, as the FZG for example, was not possible to implement due to the slippage between the pulleys and the belt. This implies that a drive and load elements were incorporated in the design.

Three types of load elements were considered: an hydraulic system, a mechanical break system and a electric generator system. Considering this application the electric generator system was selected as the most appropriated due to its efficiency when compared with the others.

Most of the components were selected, namely the motors, motors modules, line modules, load cells, couplings, linear guidance system and lead screws.

An angular guidance and positioning system to impose angular misalignment between the pulleys was designed. A mechanical structure was also designed.

Contents

List of Figures

List of Tables

Chapter 1

Introduction

Power transmission between shafts can be achieved in a variety of ways. Besides rigid systems such as gears, flexible elements such as belts and chains are commonly used[1].

A belt drive, or belt transmission, is a set of pulleys, usually attached to parallel shafts, connected by an encircling flexible belt that can serve to transmit power and modify motion from one shaft to the others [2].

An important quantity in belt transmission is the pitch velocity witch correspond to the linear velocity of the belt between pulleys and is given by

$$V_{pitch} = \omega_1 R_1 = \omega_2 R_2 \tag{1.1}$$

where ω stands for angular velocity in $[rad/s]$, R stands for the pulley radius and the subscripts 1 and 2 represent the driving and driven pulleys respectively. This quantity can be theoretical or not depending on the belt type. For non-toothed pulleys the pitch velocity is a theoretical quantity because this elements slips in relation to the pulleys when transmitting power. For timing or toothed belts this quantity is not theoretical and correspond to the real liner velocity of the belt.

Another important quantity is the theoretical speed ratio between the driving and driven shafts witch is dependent on the correspondent pulleys radius and is given by

$$i = \frac{\omega_1}{\omega_2} = \frac{R_2}{R_1} \tag{1.2}$$

As happened to the pitch velocity the speed ratio can also be theoretical or not for the same reasons. For the case of timing belts the speed ratio can be also be given by

$$i = \frac{z_2}{z_1} \tag{1.3}$$

where z is the number of teeth of the respective sprocket.

These flexible systems allow power to be transmitted by shafts that are separated by a considerable distance, thus providing greater flexibility in the relative placement of driving and driven equipment. Belt transmissions, due to their flexibility, present good capabilities of damping vibrations and reduce shock transmissions [3]. Belt drives also permit design configurations where the axis of the driving and driven pulleys are not parallel such as in Figure 1.1a. Other benefit of belt drives is the easy change of speed ratio through the selection of different diving and driven pulleys sizes on the driving and driven axis as show in Figure 1.1b.

In all cases the belts are installed by approximating the shafts, wrapping the belt(s) over the pulleys and then moving the shafts back to their original position. In the simple

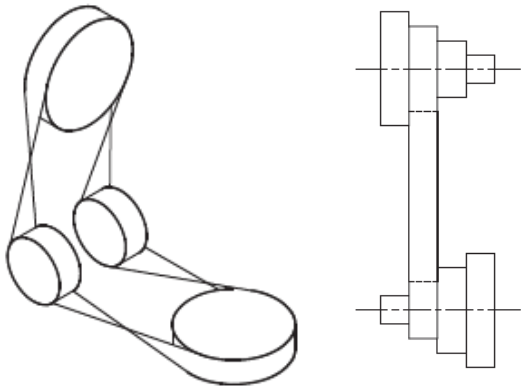

(a) Relative placement and orientation of the shafts

(b) Different transmission ratios

Figure 1.1: Versatility in the of belt drive systems

case of a belt drive with only two parallel shafts there are two possibilities of wrap the belt around the pulleys, the open configuration and the close configuration as shown in Figures 1.2a and 1.2b respectively. The dimensions characteristic of both configurations are also shown. In the open configuration both pulleys rotate in the same direction while in the close they rotate in opposite directions. In order for the close configuration to operate properly the two shafts must be misaligned, more precisely they must have vertical angular misalignment that will be presented later, due to the belt overlap or cross it self in between the pulleys.

Belts are designed with a fixed lifespan, at the end of which they must be replaced [4]. During design, these components are subject to durability tests.

1.1 Different types of belts

Belts can be flat belts running on cylindrical pulleys, with V-shaped cross section (V-belts) or circular cross section, running on grooved pulleys (sheaves), or timing belts which are flat belts with evenly spaced transverse teeth that fit in matching grooves on the correspondent toothed wheels or sprockets [2]. The main types of belts can be divided in three groups, flat belts, V-belts and timing belts [3]. In all cases, the pulley axes must be separated by a certain minimum distance, depending upon the belt type and size, to operate properly.

1.1.1 Flat belts

A flat belt consist of a elastic core surrounded by an elastomer[3]. A flat-belt transmission has an efficiency of about 98 percent, which is about the same as for a gear drive. Flat belts are quiet, efficient at high speeds, can transmit large amounts of power over long center distances, and can absorb more torsional vibration from the system than either V-belt or gear drives. Flat belts are made of urethane of rubber-impregnated fabric reinforced with steel wire or nylon cords to take the tension load. One or both surfaces may have a friction surface coating. Usually, flat belts are purchased by the roll, cut to length and the ends are joined by using special kits furnished by the manufacturer. Two or more flat belts running side by side, instead of a single wide belt, are often used to form a conveying system.

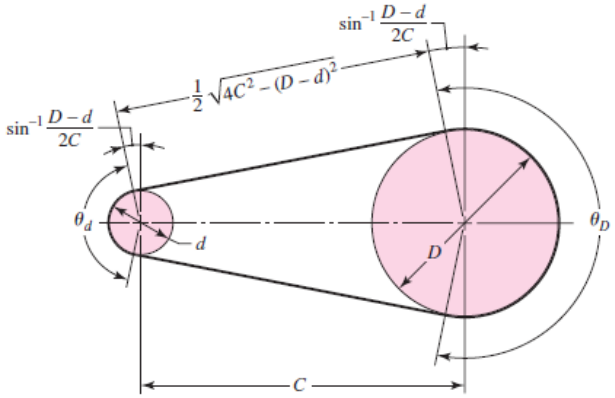

(a) Open configuration

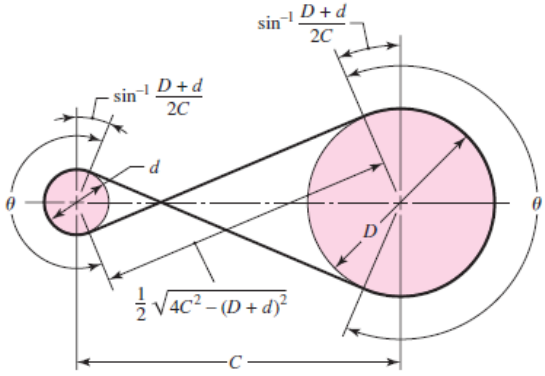

(b) Close configuration

Figure 1.2: Types of configurations in a two pulleys drive system

1.1.2 V-belts

V-bets, as it's name indicates, are characterize by having a V shape cross section. This type of belts are comprised of two main parts, the tensile material or fibers and the envelope material. The tensile material consists of cord or fibers positioned closer to the outside perimeter and is responsible to carry the load between pulleys. The envelope material correspond to the main body of the belt, is usually made of rubber and is responsible to adhere to the pulleys grooved walls with the aim of transferring the load form the pulleys to the tensile elements.

In contrast with flat belts, V belts are used at shorter center distances. V belts are made only in certain lengths and have no joints. The efficiency of a V-belt drive ranges from about 70 to 96 percent [3].

A variant cross section geometry for V-belts is the wedge belt, shown in Figures 1.3. The V or wedge shape causes the belt to penetrate in the corresponding groves, promoting friction and increasing torque capacity [5]. It is also possible to use multiple belts placed side by side making a smaller global cross section for it's power capability.

An more elaborated type of V-belts are the V-ribbed belts. They are made up of individual V-belts rigidly connected by a joining band [6]. This compact drive element with single belt characteristics is also known as a joined V-belt. V-ribbed belts are capable of combining advantages of both flat belts and V-belts. Figure 1.4 presents the cross section

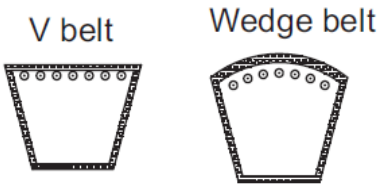

Figure 1.3: Typical and wedge V-belts [5]

of both single and ribbed V-belts.

1.1.3 Timing belts

Also called toothed belts, timing belts are made of rubberized fabric and steel wire and have teeth that fit into grooves cut on the periphery of the sprockets [3]. The timing belt does not slip and consequently transmits power at a constant angular-velocity ratio. The fact that the belt is toothed provides several advantages over ordinary belting. One of these is that no initial tension is necessary, so that fixed-center drives may be used. Another is the elimination of the restriction on speeds. Disadvantages are the cost of the belt, the necessity of grooving the sprockets and the attendant dynamic fluctuations caused at the belt-tooth meshing frequency.

When constant velocities are required, toothed belts are used [4]. However, due to belt elasticity, their length must be limited or there is the risk of mismeshing. Pre-loading is not generally used in these applications, but for other belt types it can increase the transmissible power.

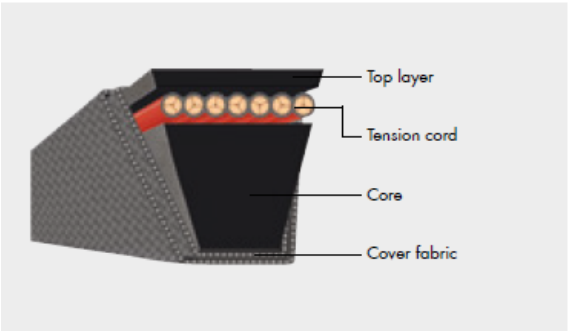

(a) Single V-belt

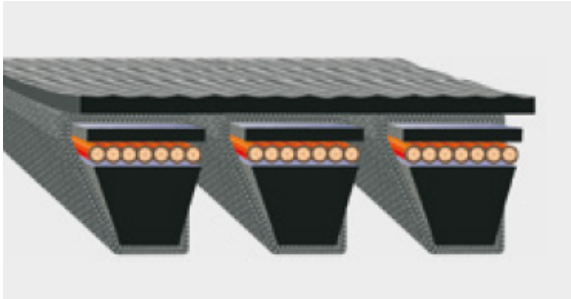

(b) V-ribbed belt

Figure 1.4: V-belts [6]

1.2 Power losses in belt transmission

The large majority of belt transmissions uses V-belts, which are the cheapest, presenting an efficiency curve that drops rapidly when the load moves away the design load [7].

The efficiency of a belt transmission can be defined by equation (1.4)

$$\eta = \frac{W_{out}}{W_{in}} \tag{1.4}$$

where η represents the efficiency of the mechanical transmission and W_{out} and W_{in} correspond to the mechanical power from the driven and driving devices respectively in $[W]$, or more specifically by (1.5)

$$\eta = \frac{T_{out} \times \omega_{out}}{T_{in} \times \omega_{in}} \tag{1.5}$$

where T stands for torque in $[Nm]$ and ω in $[rad/s]$. The losses in belt transmissions are a combination of torque losses and speed losses[7].

1.2.1 Torque losses

The torque losses include the hysteresis losses and the frictional losses. The hysteresis losses are due to the belt bending and unbending around the pulley and occur at four flexing positions of the belt working cycle (Figure 1.5). Hysteresis losses per cycle are function of the stress imposed on the belt, which for the same load, may vary with the belt thickness, pulley diameter and the material damping factor. The friction losses are due to the contact between the side walls of the belt and the inside walls on the pulley or due to viscus resistance with the surrounding air. The friction losses due to contact occur when the belt enters or leaves the pulley and are particularly significant in V-belts since they rely on mechanical grip with the walls of the pulley for torque transmission.

1.2.2 Speed losses

The speed losses do not occur in timing belts and include slip losses and creep losses. Slippage occurs when there's not enough belt tension to provide static friction between the belt and the pulley. Creep losses are due to different belt elongation entering and leaving the pulley. Due to increased tension in the section of the belt pulled by the driver pulley, a slightly longer and narrower belt leaves the driven pulley than enters it. This difference causes the belt to creep around the pulley, which reduces the speed of the driven shaft.

Slippage characteristics can be used as advantage by permitting the pulleys to be moved closer in order to disengage the drive if nedded [1].

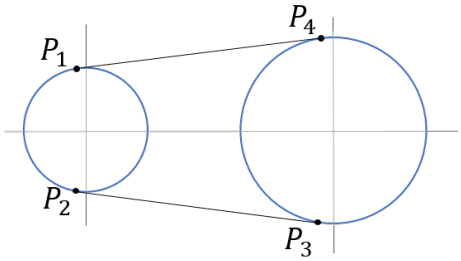

Figure 1.5: Belt drive showing the four flexing points [7]

1.3 Misalignment

Misalignment is one of the most common causes of premature belt failure, see Figure 1.6 [8]. The problem gradually reduces belt performance by increasing wear and fatigue. Depending on severity, misalignment can destroy a belt in a matter of hours.

1.3.1 Misalignment in co-linear shafts

Misalignment in theoretical co-linear shafts is very common in couplings and can manifest itself in two ways. The first one is a parallel offset, as shown in Figure 1.7a, and it's often found in small equipment [9]. The second type is angular misalignment, as shown in Figure 1.7b. Both the first and second types of misalignment are very unlikely to occur on their own, but rather as a combination of both.

1.3.2 Misalignment in parallel non co-linear shafts

Misalignment in belt drives result in severe wear of these components [9]. In multiple-belt or V-ribbed belt transmissions misalignment can alter the tension of the different belts, decreasing in some of them and increasing in others, causing some to slip and others to be overload, which can lead to premature belt failures.

Similarly to the misalignment in co-linear shafts, the misalignment in belt drives can be described as combination of independent misalignments, one of them being parallel offset between the sheaves, as shown in Figure 1.8a, and the other being angular misalignments. In belt transmission, due to the shafts being non co-linear, the angular misalignment can assume two distinct independent configurations, horizontal angular misalignment or toe and vertical angular misalignment or camber. The first one resulting in the shafts being co-planar and coincident, as shown in Figure 1.8b, and the other resulting in the shafts being non co-planar and keeping their minimal distance equal to the parallel configuration, as shown in Figure 1.8c.

Angular misalignment results in accelerated belt/sheave wear, instability in individual V-belts and uneven belt and cord loading in multiple belt drives. Wide belts are more sensitive to angular misalignment than narrow belts.

Parallel misalignment also results in accelerated belt/sheave wear and instability problems with individual belts. Uneven belt and cord loading is not as significant concern as angular misalignment. This misalignment is typically more of a concern with V-belts. They run in fixed grooves and cannot move axially as synchronous or flat belts can.

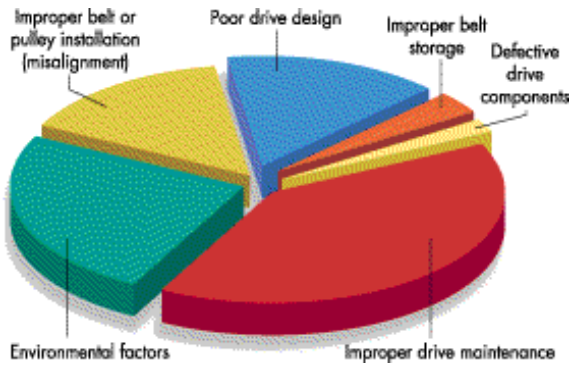

Figure 1.6: Sources of problems in belt drives

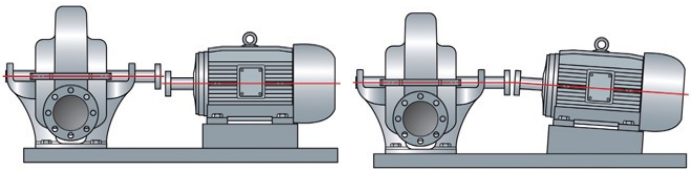

(a) Parallel offset (b) Angular misalignment

Figure 1.7: Types of misalignment in colinear shafts [10]

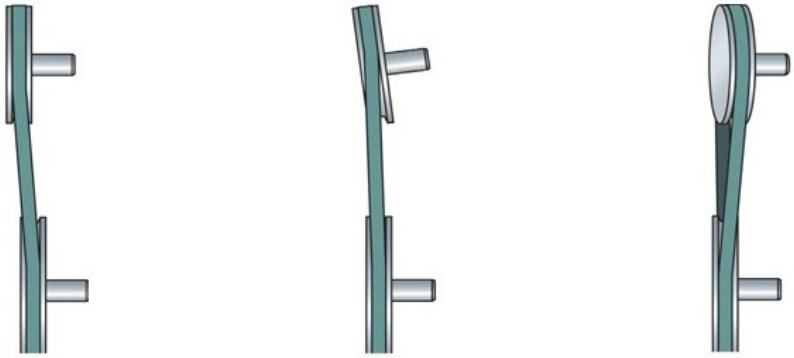

(a) Parallel misalignment (b) Horizontal angular misalignment (c) Vertical angular misalignment

Figure 1.8: Types of misalignment in non colinear parallel shafts [10]

Each type of misalignment can be quantified through an independent degree of freedom as shown in Figure 1.9.

The effect of camber misalignment is related to pulley diameter and belt span. For the same camber a combination of large diameter pulley and short belt span has significant impact in the operating conditions of the belt drive.

1.4 Contact mechanics of belt-pulley

The attempts to explain the mechanical behaviour of ropes and belts goes as far back as 1762 made by Euler [11]. Because of it's importance the mechanics of belt friction relating the pull-force and the hold-force applied at the two ends of the belt are discussed

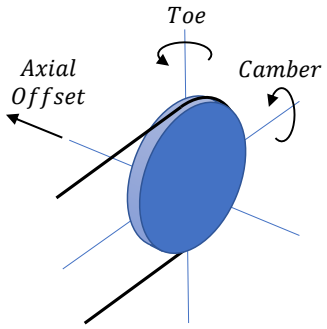

Figure 1.9: Offset, toe and camber of a pulley

in most textbooks of mechanical engineering [12]. Consider a flat belt of negligible thickness wrapped around a fixed circular disk with a warp or contact angle θ, as shown in Figure 1.10a, being T_1 the hold-force and T_2 the pull-force at the instant of impending slip (incipient sliding). The belt warped around the pulley, pulled against it by the forces T_1 and T_2 builds a local pressure $p(\varphi)$ and a local friction force $f(\varphi)$, both per unite length, over the entire contact angle θ.

From the static equilibrium of an infinitesimal element with length $R\mathrm{d}\varphi$ (see Figure 1.10b) in the normal and tangential directions it's possible, neglecting the quantities of second order, to conclude

$$\sum F_n = 0 : T = pR \tag{1.6}$$

$$\sum F_t = 0 : \mathrm{d}T = fR\mathrm{d}\varphi \tag{1.7}$$

In this moment the problem is statically indeterminate since there are two equations for three unknowns $T(\varphi)$,$p(\varphi)$,$f(\varphi)$. Adopting the Coulomb law of dry friction, the local friction force is now a function of the contact pressure, i.e. $f = f(\varphi) = \mu p(\varphi)$, where μ is the static friction coefficient. From here a system of two equations can be reduced to the following expression

$$\mathrm{d}T = \mu T\mathrm{d}\varphi \tag{1.8}$$

Integrating this expression over φ from 0 to θ results in the Euler formula, also known as the Euler-Eytelwein equation or capstan equation

$$T_2 = T_1 \mathrm{e}^{\mu\theta} \tag{1.9}$$

This result can be reached using other approaches, such as the virtual work approach [12] and can be used to analyze static problems such as structures. To characterize dynamic systems, where motion is of paramount importance, more sophisticated models have to be established.

The contact mechanics between a belt and pulley can be included in the realm of contact mechanics. On 1875 Reynolds studdied rolling friction between different objects and concluded that a rubber cylinder moved forward, in one revolution, more than its undermanned circumference when rolling over a plane of a harder material [13]. He explain this result supporting it with the influence of the Poisson's ratio in the tangential strain

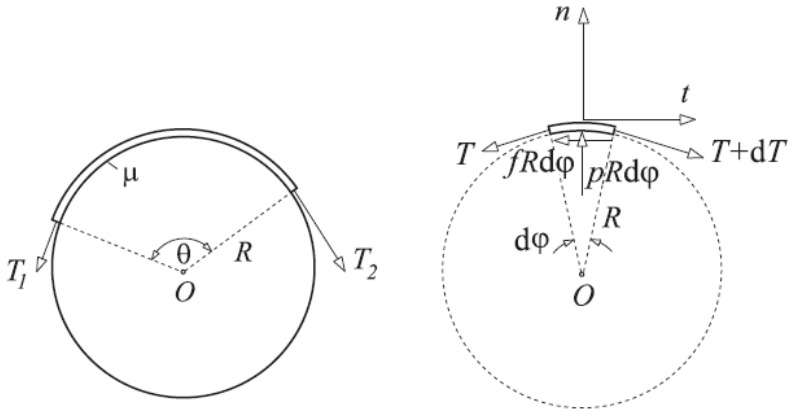

(a) Tensions in a belt

(b) Free body diagram of a belt's infinitesimal length element

Figure 1.10: Flat belt warped in pulley [12]

due to the compression load in the radial direction. He also concluded that a smaller disc rolling over a larger one of the same material would travel a larger distance per revolution than its circumference, and that the larger would travel a smaller distance per revolution than its circumference. However it follows from the Hertz theory that the tangential strain is, in general, compressive [14]. The anomaly in Reynolds' results relies on the use of a relatively thin rubber cover on more rigid hub.

The most elementary example of creep in roling contact is provided by a flexible elastic belt transmitting power between two pulleys as shwon in Figure 1.11 [14]. The elastic creep theory considers that the belt is extensible, flexible and thin enough so that the bending and shear strains can be negligible [15]. This model uses the Coulomb friction law with assumes that the frictional force q is proportional to the friction coefficient μ times the normal force n. Being $T_1 = T_0 + t$ and $T_2 = T_0 - t$ the forces on the tight and slack sides respectively. Solving for T_0 leads to

$$T_1 - T_2 = 2t = M/R \tag{1.10}$$

were M is the torque being transmitted. Using the Euler formula it's possible to determine the arc angle ϕ over witch there's slip as

$$\mathrm{e}^{\mu\phi} = \frac{T_1}{T_2} = \frac{T_0 + M/2R}{T_0 - M/2R} \tag{1.11}$$

Being λ the extensibility of the belt given by $\lambda = \varepsilon/T$, being ε the longitudinal strain such that the infinitesimal element of length $\mathrm{d}x$ when unstretched has the length $\mathrm{d}l = (1 + \varepsilon)\mathrm{d}x$ when under tension. The velocity of the element can be given by

$$v = \frac{\mathrm{d}l}{\mathrm{d}t} = (1 + \varepsilon)\frac{\mathrm{d}x}{\mathrm{d}t} = (1 + \lambda T)V \tag{1.12}$$

where $V = \mathrm{d}x/\mathrm{d}t$. Since the tension T of tight side of the belt is greater than that of the slack side, it's straightforward the conclusion that v_1 is greater than v_2.

The creep ratio for this simple system can be defined as

$$C \equiv \frac{(\omega_1 - \omega_2)R}{V} = \frac{v_1 - v_2}{V} = \lambda(T_1 - T_2) = \lambda M/R \tag{1.13}$$

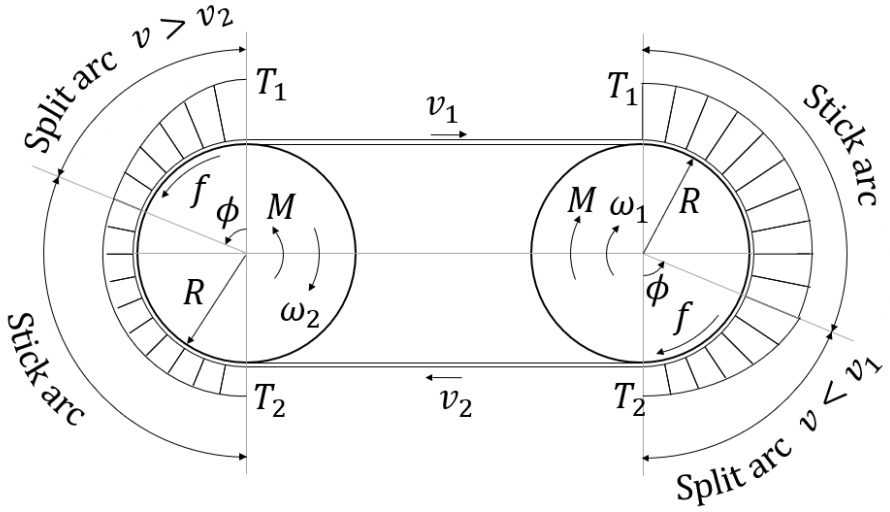

Figure 1.11: Creep on a thin flexible belt [14]

This expression does not depend on the initial pre-tension t but rather relay on the extensibility λ.

A lot of modern belts are composed by a load carrying component, made of fibers or steel cords, enclosed in an envelope, made of a resilient material. The dissimilarities in the two materials and the inextensibility of the tensile material go against the assumptions in witch the creep theory is based on, special in V-belts since these are considerable more thick then the others. For this reason this more classic approach is not always suitable and more elaborated theories were developed.

In 1970 Firbank developed a new theory, now known as shear theory, in which he considered a flat belt composed of a thin flexible and inextensible load-caring material in the outside perimeter and a thick softer envelope material in the inner perimeter that can be subjected to shear stress [14]. In his work he assumed that a transverse plane section of the belt remains a transverse plane if no tangential forces are applied. He also assumed that the kinetic friction coefficient to be constant, the static friction coefficient to have a maximum limiting value and did not consider any inertia effects. He claims that, at the beginning of the contact, the belt enters with no shear deformation and, after the contact, as the belt is tangentially pulled by the pulley shear deformation occurs. The same way as in the classic creep theory, in this model the contact is characterized by a stick and a slip region.

In 1991 Gerbert revisited the creep and shear theories and take into consideration dynamic effects [16]. He claims that, in the driving pulleys, the behaviour in the bending and unbending regions changes the directions of the friction forces in those regions. Such rapid bending and unbending of the belt into and from the pulley affects both the contact angle and the radial compliance between the belt and the pulley. A few years later in 1996 Gerbert presents an unified slip theory for V belts considering creep, shear, seating/unseating and compliance [17]. In the same paper he compares his theory with experimental data and find a good agreement between the two.

More recently, due to the development of computing capabilities, finite element methods has been used with the purpose of characterizing the mechanisms of contact between the pulley and the belt.

J. Hu et al. in 2009 develop a 3D finite element module with the purpose of representing the non-linear elastic behavior in V-belts and the effects of misalignment in V-ribbed drive systems [18]. In their work they concluded for the driving pulley that toe and camber causes uneven distribution of belt slip and friction force and that toe is more influential than camber on the tangential friction force distribution. They also concluded that for the driven pulley that both toe and camber cause more biased contact than that on the driver case.

1.5 Review on belt drive test rigs

Many experimental works can be found about mechanical transmission systems. About belt transmissions in particular there's a great recent focus in serpentine drive systems commonly use in front end accessories of vehicles due to it's general hybridization, e.g. the development of technologies such as the starter/alternator [19][20].

The studies can be roughly separated into two categories, the contact mechanics between the belt and the pulley and the dynamic behavior of belt drive.

B. Balta et al. in 2015 investigated experimentally the influence of pulley diameter, pulley speed, belt length, belt pre-tension, belt material and braking torque on the slip behavior of a V-ribbed belt drive with two equal-sized pulleys [21]. Their test rig allows

them to study a transmission power up to 3[kW] or 10 [Nm] of braking torque. They varied one factor at a time and incorporated the results in a response surface method. In their experimental set up an AC motor with a frequency inverter was used to control the angular velocity of the driver pulley. The breaking element consists of an hydraulic circuit composed of a pump and a valve, by adjusting the valve the breaking torque was controlled. The electric motor and driver pulley were mounted in a moving platform used in combination with a spring to adjust the belt tension. The angular velocities of the pulleys were measured with two optical encoders. They observed that the smaller the pulley size the larger the slip and that below a certain level of belt pre-tension, slip increase rapidly under all types of test conditions. They also observed that increasing the braking torque causes a significant increase in slip. They concluded that the effects of belt drive parameters are interdependent of each other and their relationship with slip is non linear for some of them.

A. Tonoli et al. presented in 2016 a multipurpose test rig for study belt drive systems in hybrid powertrains [20]. Their aim is to describe the design and the main characteristic of a test rig whose purpose is to investigate the behaviour of belt drive systems in dynamic conditions. They manufactured a test rig that mimics the front-end accessories drive system of a modern day car. The layout reproduced the setup of real engine where the belt drive system connects to several components, being one of them the starter engine/generator. To properly simulate this system they have to design it such that (i)most of the time the power input is associated with the crankshaft, being the starter engine working as a load in generator mode; (ii) the power input being associated with the starter and the crankshaft working as a load. To achieve such behaviour they used two permanent magnets motors in a close loop controlled configuration using a proportional-integral (PI) controller for each motor. The motor simulating the crankshaft has a speed and torque rated at 2600 rpm and 140 Nm while the motor simulating the belt starter generator has 8000 rpm of rated speed and 20 Nm of rated torque. In their work a regenerative power scheme was implemented being the two motors inverters connected to the same common DC busbar. They used a load cell to measure the tension on the belt.

1.6 Purpose and Layout

1.6.1 Purpose

A large amount of information can be found characterizing the behaviour of belt drive systems, either static, dynamic or thermal, both numerical or experimental. However, not as much information is available explaining the influence of misalignment, combined or not with operating parameters, in efficiency and durability of belt drive systems. The aim of this work is to design a test rig capable of reproducing several independent operating condition, such as:

- Misalignments,
- Lack or excessive pre-tension,
- Excessive torque.

with the intent of understanding their influence on the efficiency of belt drive systems and on the durability of the belt. It would also be interesting to manufacture the test rig in such a way that the influence of other parameters in torque and speed losses could be analysed:

- Pulleys diameters,
- Transmission ratio,
- Number of belts,
- Belt length,
- Center distance.

In this way, the proper combination of the pulleys diameters and belt length could be studied, and the effects of the contact angle between the pulleys and the belt might be analysed. Furthermore, it would be interesting to combine these last parameters with the misalignments in order to study the close configuration shown in Figure 1.2b. The scale of the project was established *à priori* to a power of 5.5 kW.

1.6.2 Layout

The main topics of this work are the following:

Chapter 1: *Introduction* presenting a brief introduction of the types of belt drive systems, characteristics and main topics of research.

Chapter 2: *Power scheme* presents the study of the powering and breaking elements for the test bench as well as the description of the solution selected.

Chapter 3: *Overview* makes an superficial explanation of the main features of the designed test rig, a detailed explanation of the pulleys geometry and the working range of the several adjustable parameters of the test rig.

Chapter 4: *Instrumentation* examines the details associated with the measuring procedure, such as the explanation of the chosen load cells and computation of the power losses.

Chapter 5: *Shafts design* presents the designed shafts. It starts with the reactions calculation, followed with the shafts fatigue design, and concludes with the bearings calculation.

Chapter 6: *Base structure* presents the design of the supporting structure.

Chapter 7: *Misalignments implementation* discusses the details associated with the misalignments implementation, presenting the chosen solution for some and design solution for the rest.

Chapter 8: *Conclusions* summarise the important achievements of this work as well as the necessary future tasks to complete this work.

Figure 1.12 presents visually the work that will be discussed in the following chapters.

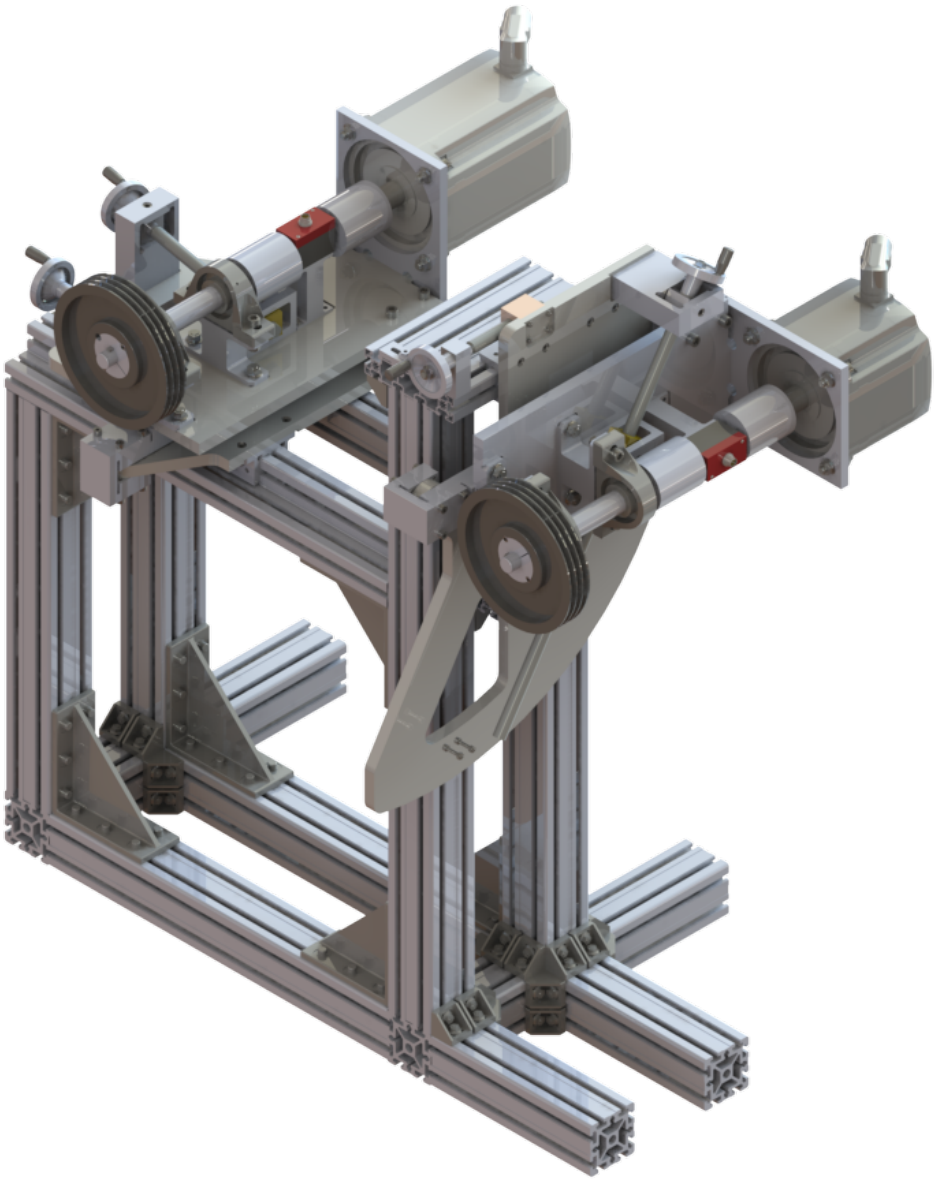

Figure 1.12: Designed belt drive test rig

Chapter 2

Power scheme

This chapter analyses possible solutions for the general layout of the test rig and for the powering and braking elements. It starts with a brief review on gear test rigs upon which will be studied the possibility of incorporating existing ideas to a belt test rig. It continues with the description of the selected layout and with the explanation of different solutions for the different parts related. To conclude the solution chosen for the powering and braking elements of this project is presented.

2.1 Gears transmission test rig

A common test rig that allows the evaluation of power loss in gear transmission is the FZG test rig, which is a particular case of the back-to-back test rig. As shown in Figure 2.1a, this rig is composed of two gearboxes, one is the test gearbox and the other is the slave gearbox, and two shafts placed parallel one to the other. One of the shafts is divided in two with the load clutch place in between while the other is continuous. The purpose of this clutch is to apply a static torque and this is done by fixing one half of the shaft to the foundation with a pin, while the other haft is twisted by means of a leaver and weights. After this, the clutch is locked by bolting the two plates together permitting the weights, leaver and pin to be removed and the shafts to rotate without losing the static torque in the system [22].

The working principle of this test rig consists in circulating mechanical power between the two shafts and the two gearboxes in a closed loop configuration. Due to the static torque applied in the system it is possible to simulate the transmission of power between two shafts without the need to provide it. The only input of power required to run the test is due to the power losses and is supplied by a motor connected to the solid shaft, as shown in Figure 2.1b. This is the big advantage of this test rig configurations. Not only it simplifies the powering architecture but also it reduces the implementation cost of it. It also allows the direct measure of the total power loss of the test rig by placing a torque and speed transducers ahead of the motor. This working principle is only possible to implement because gear mechanical transmissions, i.e. the test and slave gearboxes, maintain an average transmission ratio equal to the theoretical transmission ratio. In case of a belt transmission without timing belts this property is not present due to slippage between the belt and the pulleys. If a back-to-back test rig for non timing belt drives was implemented, the static torque resulting form an initial angular shaft deformation applied *a priory* would be lost quickly due to belt slippage. Furthermore the incorporation of test variables such as belt pre-tension and shafts misalignments would complicate the already quite complex mechanical project of a back-to-back test rig.

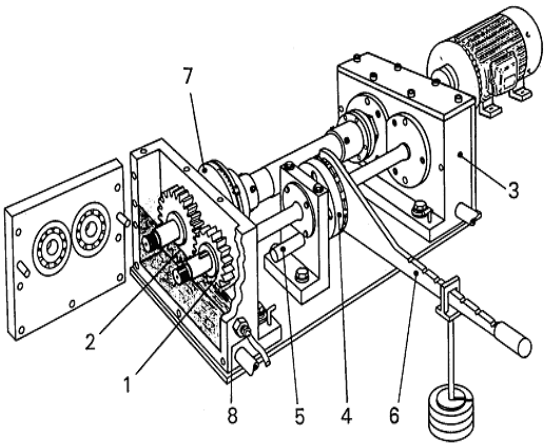

1 Test Pinion	5 Locking Pin
2 Test Wheel	6 Load Lever and Weights
3 Slave Gear	7 Torque Measuring Clutch
4 Load Clutch	8 Temperature Sensor

(a) Components [22]

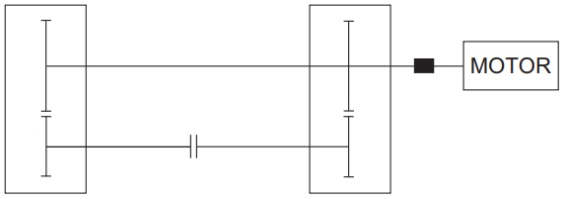

(b) Schematic representation

Figure 2.1: Back-to-back gear test rig

2.1.1 General transmission test rig

For the project in hands, an open mechanical power scheme configuration was chosen, rather than a close one, as shown previously. In this configuration two machines (M1 and M2) are necessary to simulate the driving and driven elements in a belt transmission (Figure 2.2). The machine M1 plays the role of the driving element of the transmission while machine M2 plays the role of the driven element.

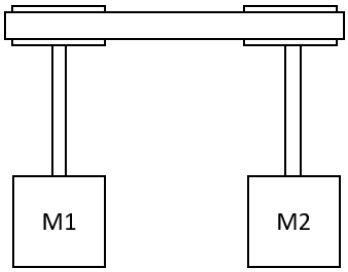

Figure 2.2: General scheme of the test rig

This configuration is the simplest, allowing a great design flexibility when incorporating the involved components. For a proper simulation of a belt drive, it should be possible to impose an operation speed in Machine M1 and to impose a load torque on the machine

M2, both at will.

One possibility for the machine M1 is to use an electric motor, wich is probably the best solution due to it's availability in the market, efficiency, cost and constant torque output in steady state.

On the other hand, for machine M2 it is possible to develop a load brake based on frictional, hydraulic, electromagnetic, etc. A frictional load can be provided simply by a brake composed of a disk and a caliper. An hydraulic load can be provided by hydraulic circuit composed of a pump and a valve, where by controlling the valve position the circuit pressure ahead of the pump can be defined and consequently the loading torque as done in [21]. An electromagnetic load can be provided by an Eddy current brake or Eddy dynamometer. These require an electrically conductive disc or shaft moving across a magnetic field to produce resistance to movement. In all this cases the power is consumed. If the power delivered by the belt transmission to the driven elements is consumed it could not be reused to other purposes and would be, eventually, converted into heat (Figure 2.3).

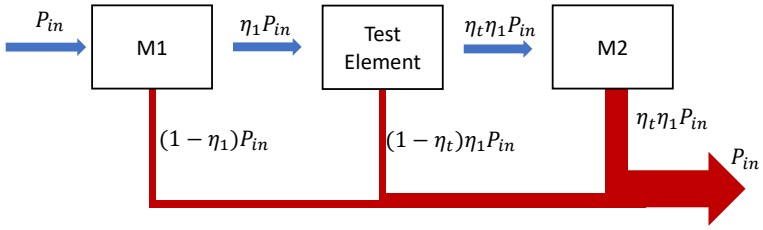

Figure 2.3: Power scheme in case of break load

2.2 Regenerative power circulation scheme

A more economically interesting solution, that can provide energy-saving, consist in replacing the driven element of the belt transmission by a regenerative element that can provide energy back to the driving element (Figure 2.4). SIEMENS is one of the companies providing this type of technology [23][24].

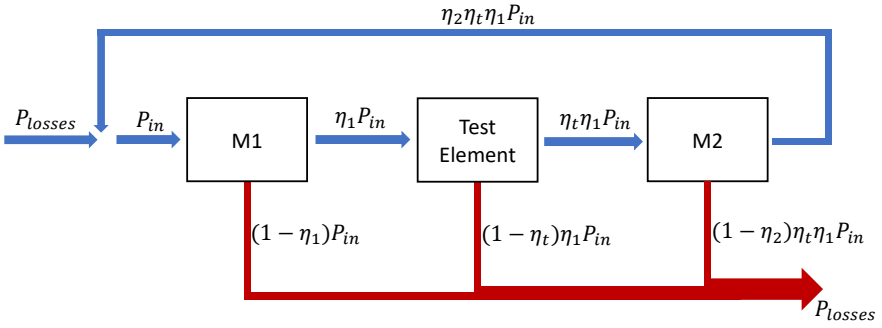

Figure 2.4: Power scheme in case of regenerative load

The chosen power solution for the test rig consists of a SINAMICS S120 system provided by SIEMENS using two electric motors, one working as a motor and the other working as an generator, in a regenerative power scheme.

The SIMOTION Motion Control systems in combination with the SINAMICS S120 drive system and the SIMOTION motors, all provided by Siemens, creating energy an

efficient solution that achieves considerable reductions in energy consumption. To get energy efficient processes an energy management is required. This initial process is divided in three phases: identification, evaluation and implementation. The first one consists in identifying the energy flows. Evaluation consists in the calculation of energy consumption. The third phase consists in the selection of the common DC link as well as the power supply. The power supply will feed the process power losses.

The SINAMICS S120 drive system is a modular system for high-performance application in single and multi-axle drives for a very board range of applications. They are capable of controlling drives in vector, servo and v/f modes, They also perform speed and torque control functions.

The SINAMICS S120 drive systems are composed of separated power and control units. The control unit is selected according to the required performance levels and the numbers of drives to be controlled, while the power units must be rated to satisfy the energy requirement of the application. The communication between the control unit and power units is made by a digital system interface called DRIVE-CLiQ.

As part of the SINAMICS S120 drive systems Siemens presents two types of control units: CU310-2 and CU320-2. The first one is to control a single drive, while the second one is used to control multiple drive systems.

The power units presented by Siemens are divided in two groups: power modules and motor modules. Power modules are designed for single drives witch are not capable of regenerating energy back to it's supply. Motor modules consist of a DC link and an inverter integrated together and are design to multi-axle drives. Several motor modules can be interconnected by a shared common DC busbar. Due to this they can exchange energy with one another, i.e. if one motor is operating in generator mode, the energy can be used to power another motor operating in motor mode.

To supply the motors modules a line module is used. This later generate a DC voltage from the grid and supply the DC link. Three types of line module exist: basic line modules, smart line modules and active line modules. The first one is used for infeed operation only and is not capable of recovering energy to the grid. Smart line modules can supply energy to the DC link and return regenerative energy back to the grid. The active line modules perform the same tasks as the other but generate a regulated DC voltage witch remain constant despite fluctuations on the grid. Figure 2.5 presents an overview the SINAMICS S120 systems

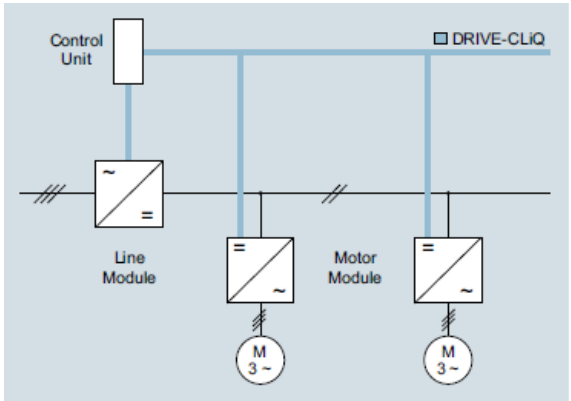

Figure 2.5: Overview of SINAMICS S120 control system

2.2.1 Electric motors

In the SINAMICS S120 systems the electric motors provided by Siemens are the Simotics servomotors and the Simotics main motors. This later are available in asynchronous/induction or synchronous versions. The asynchronous main motors have a range of power ratings from 2.8 to 1230 kW, while the synchronous form 15 to 310 kW. The minimum rated power from the synchronous motors exceeds greatly the rated power of the test rig (5.5 kW) so this type of motors are not the best suited for the test rig.

Figures 2.6 presents the characteristic performance curves of the asynchronous main motors and of the servomotors.

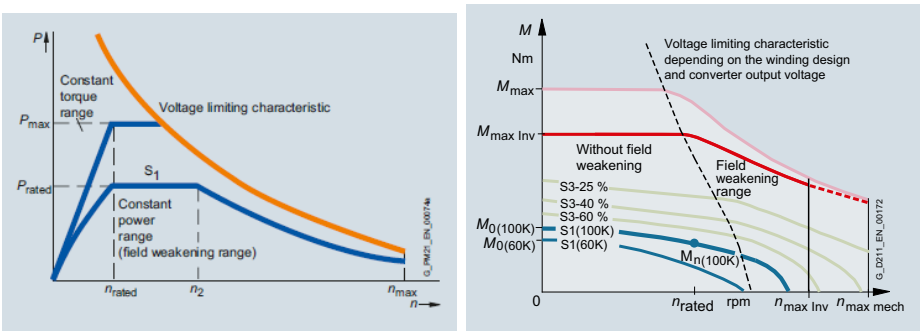

(a) Assynchronous (b) Servomoter

Figure 2.6: Typical charecteristic curves for SIMOTICS motors [24]

The motors selected for the test rig are servomotors because these, when compared with the asynchronous, are more compact and therefore lighter, have a smaller rotor moment of inertia and have a greater efficiency.

Figure 2.7 shows the selected motors, Table 2.1 their main characteristics and Figures 2.8 and 2.9 their performance curves.

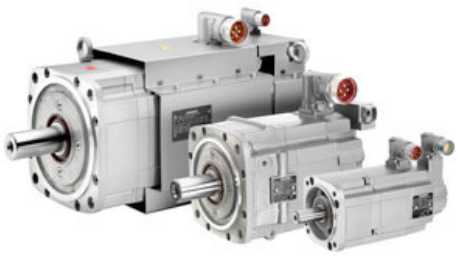

Figure 2.7: 1FT7 servomotors with natural cooling

The reason for the second motor to have a rated power significantly grater than the first one is to allow the testing of belt transmissions with transmission ratios larger then 1.0. From Figure 2.9, the second motor presents, for continuous operation, roughly 43 Nm at 1250 rpm. At these operating conditions the power transmitted to or from the second motor is 5.63 kW. With these combination the test rig can simulate a transmission ratio up to 2.4 at the power of 5.5 kW. Greater transmissions ratios can be achieved but at a lower transmitted power. So, for correctly use the motors, the operating conditions of the motors must be defined using, the transmission ratio and the input and output torques. The technical drawings of the motors can be found in Appendix A.

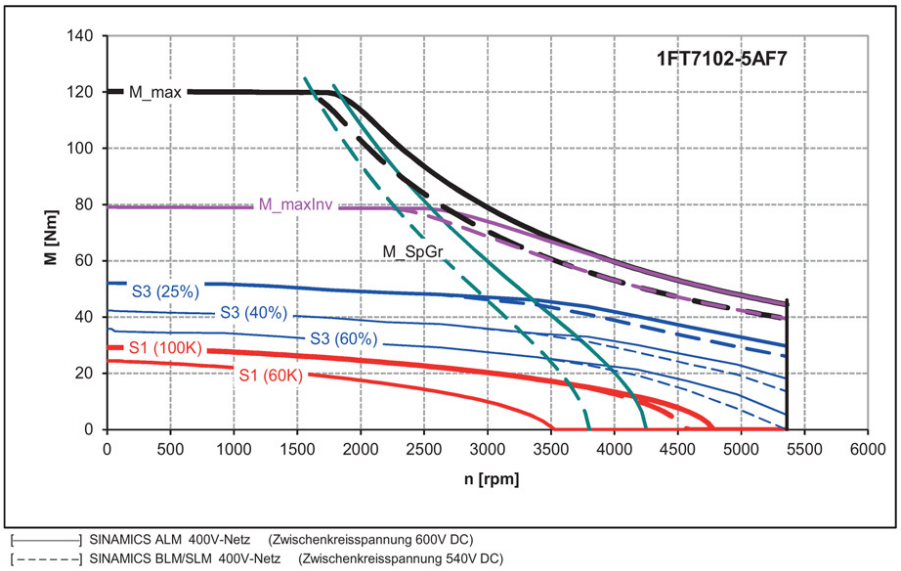

Figure 2.8: 1FT7102-5AF7 motor performance curves

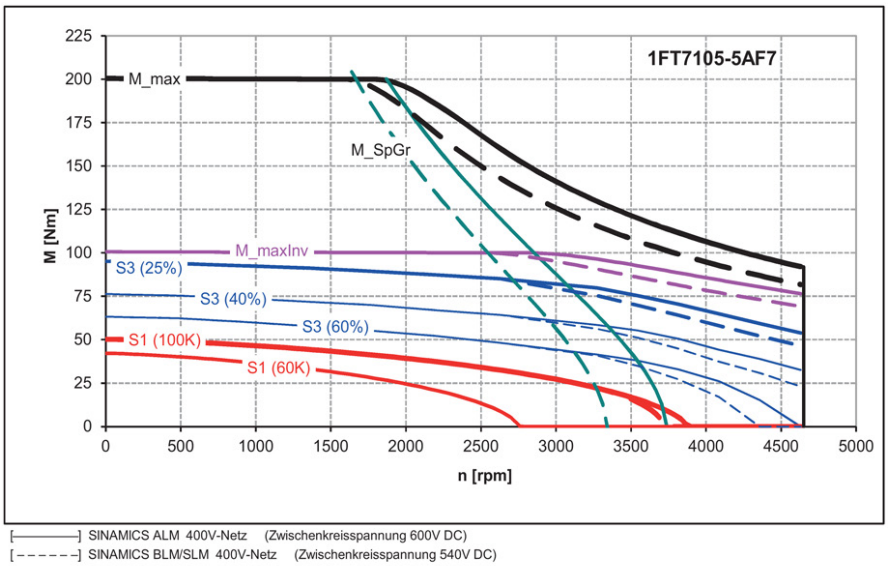

Figure 2.9: 1FT7105-5AF7 motor performance curves

Table 2.1: Main characteristics of the selected motors

Motor reference	Shaft height [mm]	Prated [kW]	M_0 [Nm]	M_{rated} [Nm]	J [kgm^2]	Weight [kg]	η %
1FT7102-5AF7 1-1BG1	100	6.28	30	20	91.4	26.1	93
1FT7105-5AF7 1-1BG1	100	8.8	50	28	178	44.2	94

2.2.2 Motor modules

For supplying the two motors presented previously two motor modules are required. The motor modules consist of a DC link and an inverter integrated together and are design to multi-axle drives. Figure 2.10 presents, as an example, the connection of the

single motor module in booksize format. The two motor modules were selected together with the motors. There main characteristics are presented in Table 2.2.

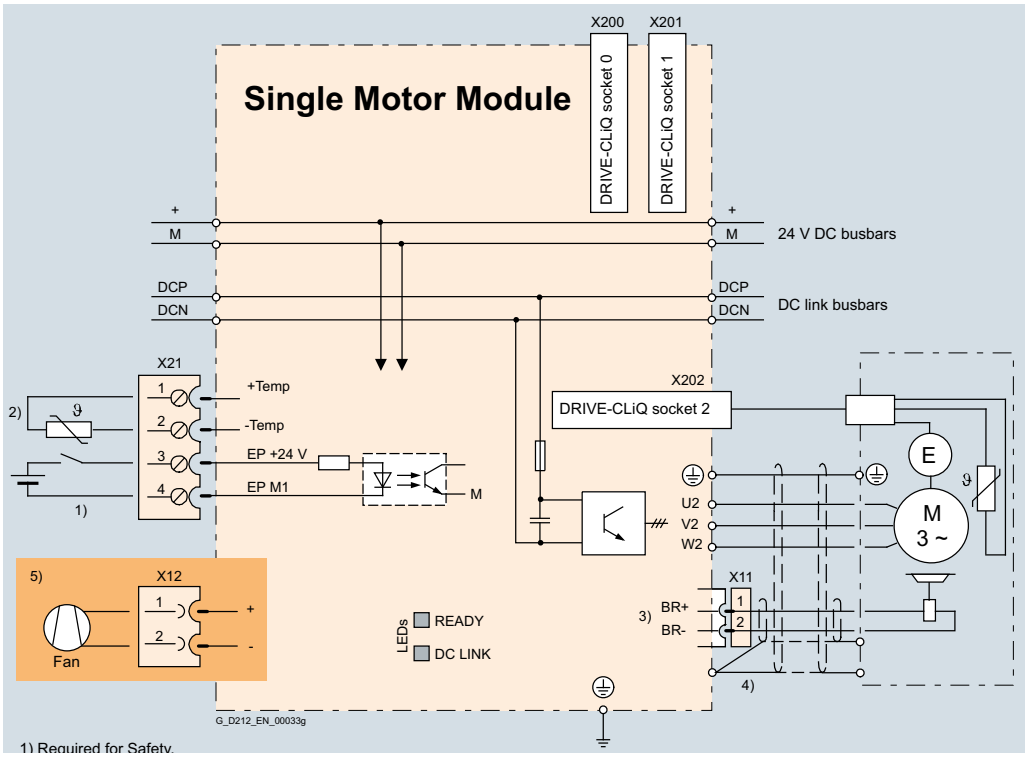

Figure 2.10: Example connection of a single motor module

Table 2.2: Motor module's thecnical specificatons

		M1	M2
Ref		6SL3120-7TE21-8AD	6SL3120- 1TE23-0AD
Cooling		Internal air cooling	Internal air cooling
Output rated current	A	18	30
Type rating based on I_{rated}	kW	9.7	16
DC link busbar capacity	A	100	100

2.2.3 Line module

The line module delivers energy to the motor modules by supplying the DC link busbar with the main line voltage.

An active line modules was selected. Siemens provides this component with different rated powers, being the minimum 16 kW. This is much larger than the most demanding working condition. By the way this occurs when M1 is working as a motor and when M2 is not generating energy, for example when the system is accelerating without a resistive load. Table 2.3 presents some information about this component. Figure 2.11 shows an example of an active line module connection.

Table 2.3: Active line module in booksize format

Ref		6SL3130-7TE21-6AA4
Cooling		Internal air cooling
Rated power @ 380V AC	kW	16
DC link current	A	27
Input current	A	26
Current carrying capacity DC link busbars	A	100

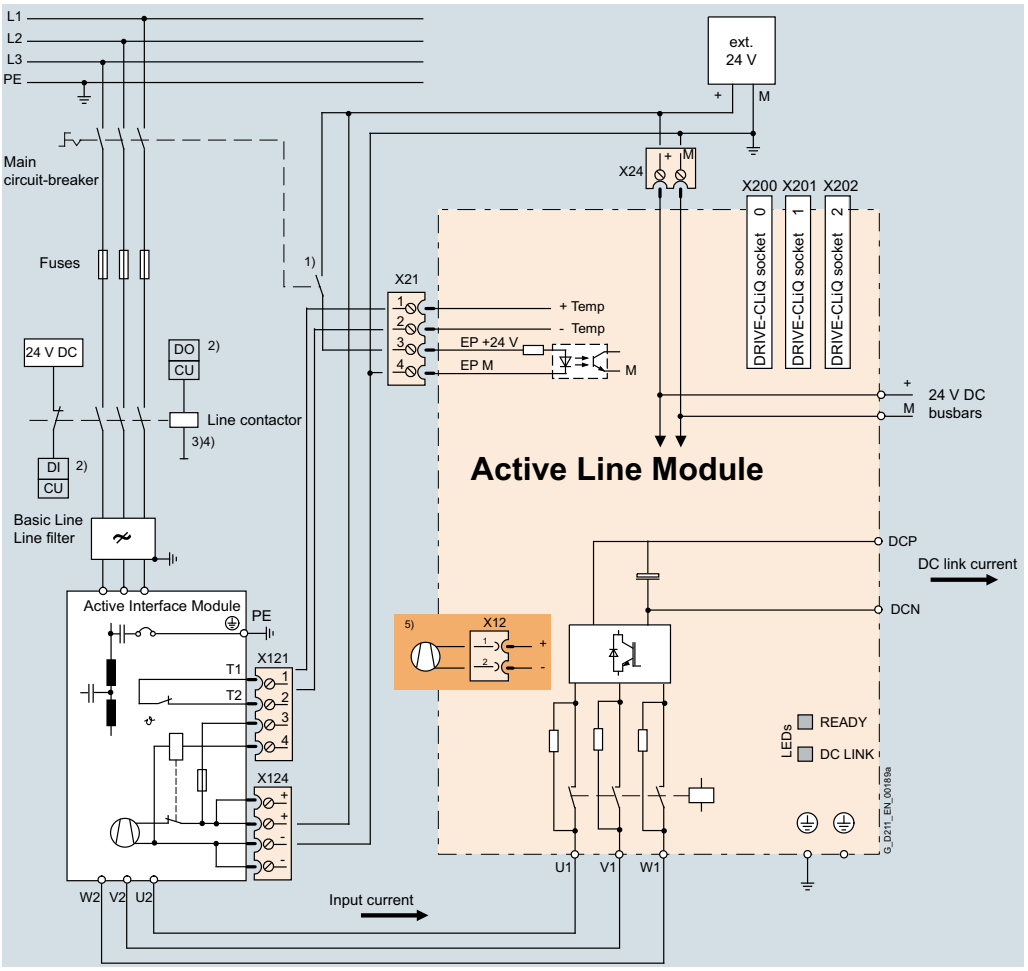

Figure 2.11: Example of an active motor module connection

Chapter 3

Overview

This chapter gives an simplified overview of the test rig. It starts with the presentation of the main components of the test rig. It continues with the definition of the minimum and maximum pulley diameter that are possible to use in the test rig. To conclude, the working range of the several misalignments and belt's pre-tension are presented.

3.1 Main components and parts

As mentioned before the designed test rig consists of an open mechanical power circuit. This architecture consists of two shafts placed side by side, being at one end the power and load elements and at the other end the test transmission elements, in this case pulleys and belts.

In order to measure the torque and speed loss from one shaft to the other is necessary to measure the torque and speed present in both shafts and then compute the difference. This is done by incorporating one load cell on each shaft. The load cells are design to measure axial torque and not bending torque or axial efforts, therefore the design of the test rig must be such that no bending efforts or axial loads reach the load cells. To prevent bending torques from reaching the load cells, the two supports of each shaft must be placed between the load cell and pulley (Figure 3.1). To connect the load cells shafts and motors together couplings are used.

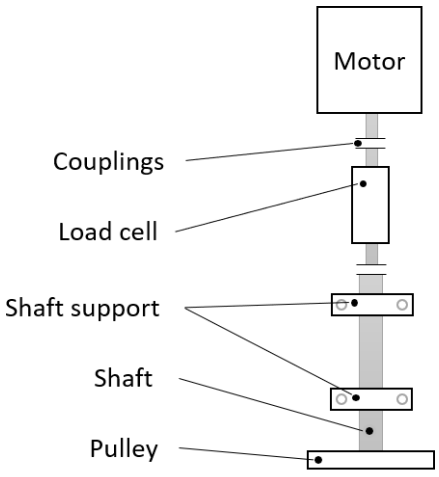

Figure 3.1: Main components associated with each shaft

In order to be able to impose misalignments between the two pulleys, the assembly

which drives each one of the pulleys must be mounted on a movable platform. In total there are three misalignments in belt transmissions, one of them is a linear misalignment, also known as axial offset, and the others are angular misalignments know as toe and camber. These make up three degrees of freedom that one of the movable bases must have in relation to the other. Beside these a fourth degree of freedom is needed to permit the mounting and dismounting of the belts and to impose its pre-tension. This degree of freedom is a linear one and corresponds to the center axis distance. In total there are two linear and two angular degrees of freedom. To implement them more easily these were separated evenly between the two pulleys, one linear and one angular for each pulley. Figure 3.2 shows the attribution of each degree of freedom to the corresponding pulley, where the center distance, axial offset, camber and toe are represented respectively by a, b, θ_c, θ_t.

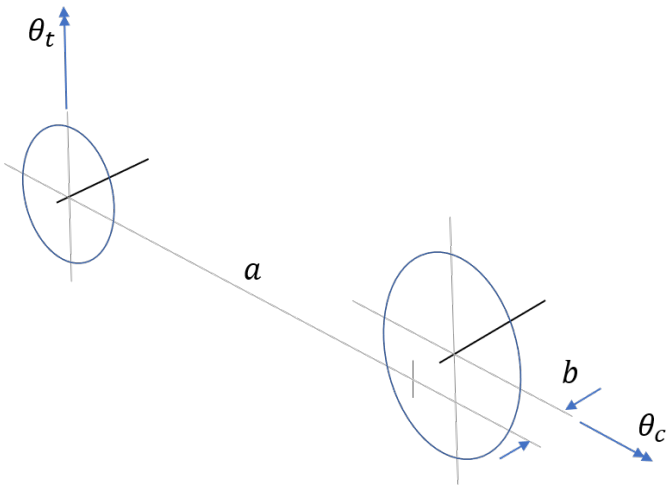

Figure 3.2: Separation of the degrees of freedom for pulleys

Each pulley is associated to one linear degree of freedom and one angular degree of freedom. The linear degrees of freedom were implemented directly on the base structure and the angular degrees of freedom were each implemented on top of the corresponding linear one, so the linear degrees of freedom are relative to the inertial reference frame and the angular ones are relative to the corresponding linear one.

To each degree of freedom there is a part associated with it. These parts are plates where other components are attached to. Each of these plates has a movement guiding mechanism to define its path. The linear guiding mechanisms are easily implementable on the base structure. On the other hand the angular ones are more easily implementable if they are mounted on a surface perpendicular to its axis of rotation. This leads the camber and axial offset to be mounted vertically and the toe and center distances to be mounted horizontally. Figure 3.3 presents the relative position of each one of these plates.

3.2 Belts and Pulleys

The set of pulleys selected for the test rig are provided by Optibelt. Optibelt is a brand capable of offering the parts needed to implement belt transmissions, namely the belts, pulleys and taper bushes.

Given the variety of products for belt drives made available by Optibelt, the chosen types of belts to be used in the test rig are the non-ribbed and non-toothed V-belts.

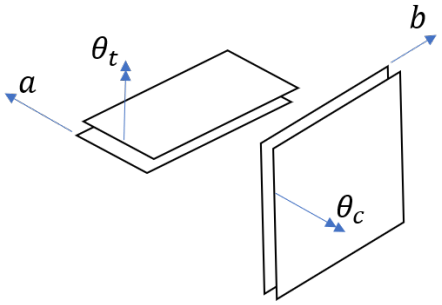

Figure 3.3: Relative position of each of the plates associated to the degrees of freedom

Nevertheless, the test rig was designed in such a way that allows for the easy substitution of the pulleys for other types of belts. The types of V-belts to be tested can be divided in 2 groups, the wedge V-belts and the classic V-belts. The main difference between the two lies on the height of the belt's cross section, being higher in wedge V-belts. Regarding the wedge V-belts, the cross section of these are produced based on two different unit systems, the metric system and the imperial system. Regarding the metric system, Optibelt wedge belts conform to BS 3790, DIN 7753 Part 1 and ISO 4184 standards. On the other hand, regarding the imperial system they conform to the USA RMA/MPTA standard. Figure 3.4 shows the generic cross section of these belts and tables Tables 3.1 and 3.2 present the dimensions of the standard cross sections according to the metric and imperial systems. The values of d_{dmin} and d_{amin} are just recommended values. Regarding classic belts,

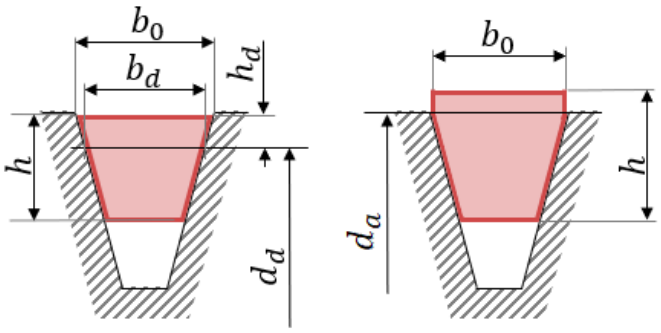

(a) Metric system (b) Imperial system

Figure 3.4: General cross section of wedge V-belt

Table 3.1: Standard wedge belts according to BS 3790, DIN 7753 Part 1 and ISO 4184

Section	SPZ	SPA	SPB	SPC
b_0[mm]	9.7	12.7	16.3	22
b_d[mm]	8.5	11	14	19
h[mm]	8	10	13	18
h_d[mm]	2	2,8	3,5	4,8
d_{dmin}[mm]	63	90	140	224

they present a cross section similar to the wedge belt according to the metric standards which dimensions can be found in Table 3.3. Optiblet offers one type of classic V-belts,

Table 3.2: Standard wedge belts according to USA Standard RMA/MPTA

Section	3V/9N	5V/15N	8V/25N
b_0 [mm]	9	15	25
h [mm]	8	13	23
d_{amin}[mm]	63	140	335

Table 3.3: Standard clasic belts according to DIN 2215, BS 3790 and ISO 4184

DIN 2215	(5)	6	(8)	10	13	17	(20)	22	(25)	32	40
BS 3790/ISO 4184	–	Y	–	Z	A	B	–	C	–	D	E
b_0[mm]	5	6	8	10	13	17	20	22	25	32	40
b_d[mm]	4.2	5.3	6.7	8.5	11	14	17	19	21	27	32
h[mm]	3	4	5	6	8	11	12.5	14	16	20	25
h_d[mm]	1.3	1.6	2	2.5	3.3	4.2	4.8	5.7	6.3	8.1	12
d_{dmin}[mm]	20	28	40	50	71	112	160	180	250	355	500

called *VB*, and two types of wedge V-belts called *SK* and *RED POWER II*. According to the manufacturer the wedge belts are capable of a grater performance and the *RED POWER II* belts are free of maintenance.

For the selection of the pulleys to be used in the test rig, the calculation software *CAD 6.0* provided by Optibelt was used. Their calculation software replicates the calculation procedure present in the technical manual [6]. The reports generated by the Optibelt software used in the selection of the pulleys can be found in Appendix B. The two calculations made correspond to a transmission ratio of 1 to 1 and of 1 to 2.4 both at 5.5 kW and an input speed of 3000 rpm. The corresponding input torque is 17.51 Nm and the output torque for the 2.4 transmission ratio is 42.02 Nm. In this calculation, the type of belt was not defined *a priori* and was the software that make this decision. The software suggested the same cross section, the SPZ, and the same number of belts to be used, 2 belts. In the first test it suggested two 90 mm diameter pulleys with a belt's perimeter of 772 mm, which corresponds to a center distance of 244.63 mm. In the second test the software suggested the pulleys to have diameters of 85 and 200 mm with a belt's perimeter of 1237 mm which corresponds to a center distance of 390 mm.

Accordion to Optibelt V-belt pulleys with grooves for wedge belts according BS 3790 and DIN 7753 Part 1 are also suitable for classical V-belts according to BS 3790 and DIN 2215 with the same datum width b_d. These are known as dual duty pulleys and are the chosen type of pulleys for the test rig.

Figure 3.5 represents the dual duty pulley's cross section and Table 3.4 the corresponding values. One detail to mention is that the angle α varies with the pulley datum diameter. Table 3.5 presents the angle α as a function of the pulley diameter. The standards DIN 7753 part 1 and DIN 2215 present different minimum pulley diameters so in order to test belts under both standards the reference diameter of the smaller pulley to be chosen must be at least the one given by DIN 7753 part 1, which has the largest minimum datum diameter, 63 mm.

For the test rig, one of the design criteria demand that pulleys with up to three belts must be used. The chosen belt cross-section for the rig was the SPZ cross section given that this is the smaller wedge cross section and it is the recommended by the Optiblet software. According to Optibelt the face width of a SPZ three belt pulley is 42 mm. The

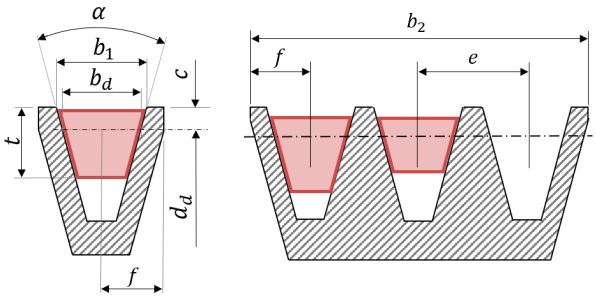

Figure 3.5: Dual pulley's cross section

Table 3.4: Dual duty pulley's mian dimentions

	DIN 7753 part 1/ISO	SPZ	SPA	SPB	SPC
	DIN 2215 and DIN 2216	Z/10	A/13	B/17	C/22
b_d [mm]		8.5	11	14	19
b_1 [mm]≈	$\alpha = 34°$	11	15	18.9	26.3
	$\alpha = 38°$	11.3	15.4	19.5	27.3
c [mm]		4	6.5	8	12
e [mm]		14±0.3	18±0.3	23±0.4	31±0.5
f [mm]		8±0.6	10±0.6	12.5±0.8	17±1.0
$t_m in$ [mm]		13	18	22.5	31.5

Table 3.5: Wedge angle function of pulley diameter acoording for wedge and classic belts

DIN 7753 part 1/ISO	SPZ	SPA	SPB	SPC
DIN 2215 and DIN 2216	Z/10	A/13	B/17	C/22
	34°±1°	34°±1°	34°±1°	34°±30'
Wedge belts	d_d 63 to 80	d_d 90 to 110	d_d 140 to 190	d_d 224 to 315
DIN 7753 part 1	38°±1°	38°±1°	38°±1°	38°±30'
	d_d >80	d_d >118	d_d >90	d_d >315
	34°±1°	34°±1°	34°±1°	34°±30'
Classic belts	d_d 50 to 80	d_d 71 to 110	d_d 112 to 190	d_d 180 to 315
DIN 2215	38°±1°	38°±1°	38°±1°	38°±30'
	d_d >80	d_d >118	d_d >190	d_d >315

pulleys diameters, due to be a test variable of the test rig, can not be fixed at particular values, being only possible to define a range of values. The minimum pulley diameter defined for the test rig is 67 mm, while the maximum is 224 mm. This allows for a range of transmission ratios from 1 up to 3.34, however, as explained before, transitions ratios above 2.4 can not be tested at the rated power of 5.5 kW.

According to DIN 1691, V-belt pulley are predominantly made from GG 20 cast iron and are available pilot bored, finished bored or with a taper bush. Optibelt software suggests the later option to all calculated drives. The taper bush design solution splits the traditional bored pulley in two main concentric components, the outside pulley and the inside taper bush. The inside wall of the pulley's bore and the outside wall of the

taper bush are conical and are hold together by two screws whose holes are drilled in the interface between these components. The hole assembly is then connected to the shaft trough friction and by a key. This solution was selected because it is relatively simple to mount and dismount and because it does not introduce any complicated features in the shafts design, being only necessary to machine the keyway. Table 3.6 shows the taper bush's dimensions for the smaller and largest pulleys. Figure 3.6 shows this type of solution.

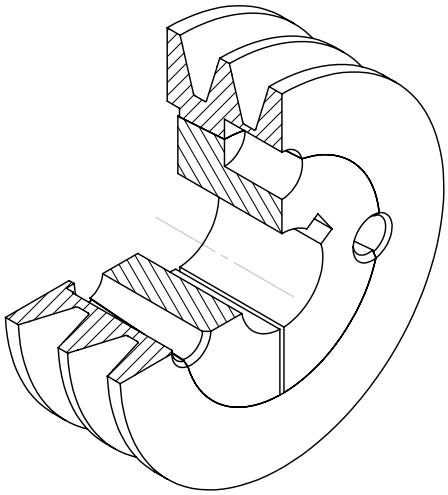

Figure 3.6: Generic pulley and taper bush system

Table 3.6: Taper bush's main dimensions for the smaler and largest pulleys

Pulleys diameter mm	Taper bush part number	Max shaft diameter mm	Min shaft diameter mm	Taper Bush face width mm
67	1108	25	10	22.3
224	2012	50	14	31.8

3.3 Working range

This section discusses the limiting range values of the degrees of freedom as well as the maximum belts pre-tension that the test rig will be designed for.

3.3.1 Axial offset

Regarding the axial offset, Optiblet's technical manual provide some limiting values for the allowed axial offset as function of the diameter of the pulleys [6]. For pulleys diameters up to 224 mm the allowed maximum axial offset is 1 mm. However, the test pretends to deliberately work away from this maximum value. For this reason a working range from 0 up to 50 mm was defined.

3.3.2 Toe

Regarding toe, Optiblet's technical manual provides a limiting value of 0.5º for what is considered proper working conditions for this angular misalignment [6]. This value is presented without any dependence of the center distance or the pulleys diameter. The same way as for the axial offset, it is pretended to work away from this recommendation. Therefore a working range from 0 to 15º was set. A higher maximum working value for this degree of freedom could be easily implemented, however this is not necessary due to the belts jump off from the pulleys.

3.3.3 Camber

Regarding camber, Optiblet's technical manual does not provides any limiting value for what can be considered proper working conditions. This degree of freedom is the one that can be used whit more flexibility to achieve less conventional power transmission design solution. Figure 3.7 shows the design versatility that this degree of freedom provide. So the working range for this degree of freedom was defined from 0 up to -90º. A negative working range was define for this degree of freedom in order to minimize the overall size of the test rig.

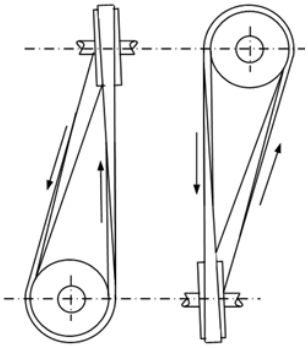

Figure 3.7: Versatility of camber misalignment

This degree of freedom can also prove to be very useful in some situations. When the transmission ratio is high and the center distance is low, the warp angle along the smaller pulley is very low. A small warp angle can lead to grater slippage between the pulley ad the belt. The small warp angle problem can be avoided using the close configuration (Figure 3.8a). However, this configuration, by default, has the problem that the belt intersects itself between the pulleys. The solution for such problem relies on design belt transmissions with a camber different from zero (Figure 3.8b).

3.3.4 Center distance

Regarding the center axis distance, this parameter will be responsible for:

- Mounting and dismounting the belts,
- Apply belt's tension,
- allowing to test different belt lengths.

To define a working domain of values for this parameter several belt's lengths provided by Optiblet, for the SPZ cross-section, in there technical manual were consulted [6]. The

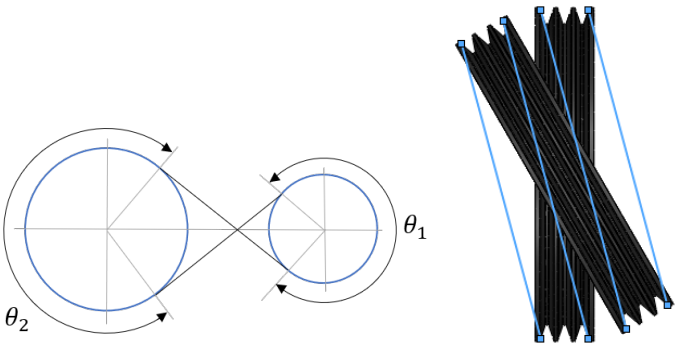

(a) Small warp angle solution

(b) Non self intersecting belt solution

Figure 3.8: Close configuration and non zero camber combination

lengths provided are divided in two groups. The first one goes from 487 mm up to 1137 mm and are not the *S=C PLUS* lengths. The second one goes from 1162 mm up to 3550 mm and are the *S=C PLUS* lengths. According to Optibelt *S=C PLUS* lengths have a tolerance considerably lower than the one permitted by DIN standard. For this reason the test rig was design for belt lengths *S=C PLUS*.

To define the maximum and minimum center distances for the test rig, besides belt lengths, the minimum and maximum pulley's diameters are needed. The minimum pulley diameter selected is 67 mm while the maximum is 224 mm. For a position with no deviations or misalignments, Figure 3.9, the center distance, belt length and pulleys diameters are related by

$$\beta = \sin^{-1}\frac{D_2 - D_1}{2a}; \qquad c = a\cos(\beta); \qquad P = \frac{D_1}{2}(\pi - 2\beta) + \frac{D_2}{2}(\pi + 2\beta) + 2c \tag{3.1}$$

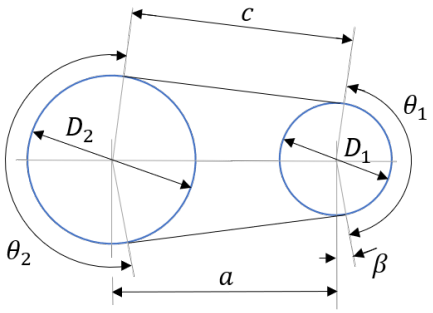

Figure 3.9: Parameters relating belts length to center axis distance

Finding the perimeter given the center distance is relatively simple, however the opposite can not be done explicitly unless the transmission ratio is equal to one and therefore $\beta = 0$. Nevertheless a numerical approximated solution can be obtain, for example, via MatLab.

The minimum belt length defined for the test rig is 1162 mm witch is the smallest *S=C PLUS* length. For this belt length, if the pulleys diameters are both equal to 67 mm, the corresponding center distance is 475.8 mm. This value provided a well defined minimum center axis distance for the test rig. The minimum center distance that the test

rig can present is 463 mm, however this value is not the minimum working center distance because some space is needed to mount/dismount and to exert pre-tension on the belts. On the other hand, for the maximum center distance it is not necessary to account for this. So the working center distance was defined to be 500 mm. The maximum center distance was defined to be 800 mm so that a 50% increase on the minimum center distance is possible.

The minimum and maximum belt lengths possible to be tested with the smaller and larger pulleys combinations can be found in Table 3.7 as well as the corresponding center distance.

Table 3.7: Minimum and maximum belt lengts with center distances for the extreme combinations of pulleys diameters

D1 [mm]	D2 [mm]	Belt length [mm]	Center distance [mm]
67	67	1212	500.8
67	67	1800	794.7
67	224	1487	508.9
67	224	2037	786.0
224	224	1737	516.6
224	224	2287	791.6

3.3.5 Belts pre-tension

To establish a value for the maximum belt tension the following working conditions were considered. The first motor's maximum torques at continuous duty is the static torque, $M_{01} = 30Nm$. The torque applied by the motor can be given by

$$M_{01} = (T_1 - T_2)\frac{D_1}{2} \tag{3.2}$$

Where T_1 and T_2 are the tight and slack sides respectively. This equation is only valid for transmissions ratios equal to one, however is as good as an approximation as β vanish. The worst case scenario corresponds to when $T_2 = 0$, leading after rearranging to

$$T_1 = M_{01}\frac{2}{D_1} \tag{3.3}$$

If $D1$ corresponded to the smallest diameter pulley, 67 mm, T_1 is equal to 895 N. This is the minimum belt pre-tension ($T1 + T2$) to guarantee that the slack side is tensioned. So, to allow the test rig to test the effects of excessive belt pre-tension, a limiting value of 1800 N was predefined, which is slightly more then the double of the previously calculated T_1.

The two calculation previously made with Optiblet software *CAD 6.0* present 692 and 724 N for the initial installation pre-tension ($T1 + T2$). These calculations both recommended the use of two SPZ belts, being the maximum static tension per belt ($T_1/2$ and $T_2/2$) 183 N.

The test rig must allow for the use of pulleys with three belts and being the maximum pre-tension for the test rig ($T1$+$T2$) defined at 1800 N, the maximum static tension per belt ($T_1/3$ and $T_2/3$) is 300 N. This value is considerable larger then the 183 N recommended by Optibelt's software.

3.3.6 Summary

Table 3.8 presents the limiting values of the variables of the test rig.

Table 3.8: Limiting values of the variables of the test rig

		min	max
Pulleys diameters	[mm]	67	224
Axial offset	[mm]	0	50
Toe	[°]	0	15
Camber	[°]	0	-90
Center distance	[mm]	500	800
Belts pre-tension	[N]	0	1800

Chapter 4

Instrumentation

In this chapter the details associated with the measurement of torque and speed are presented. It starts with the presentation of the selected torque cells. It continues with the presentation of the shafts bearings supports and couplings. It concludes with the presentation of the power losses calculation.

4.1 Load cells

As mentioned previously, due to belts slippage, is not possible to measure directly the losses from one shaft to the other. Therefore, two load cells, one for each shaft, are required.

The torque cells selected for this project are provided by ETH Messtechnik. They provide several types of torque cells as well as the associated components such as the torque cells' power supply and cables. The selected torque cell model for this projected is the DRVL [25] (Figure4.1).

Figure 4.1: DRVL ETH messtechnik's torque cell

This model is supplied with a rated torque that can vary from 0.02 Nm up to 20000 Nm. It can measure torque both in static and dynamic static conditions. The low mass moments of inertia and the high torsional stiffness that this elements have are particular beneficial in for the test rig [26].

The torque cells' shafts are constructed with aluminium or hardened carbon steel. On the shafts are attached strain gauges that can measure the shafts torsional deformation through its ohmic resistance, that is proportional to the torque applied to shaft within its elastic range. The strain gages are arranged in a Wheatstone bridge circuit. The torque is transmitted via cylinder shafts extensions with smooth shafts extension or a featherkey. For connecting the torque cell's shafts to other shafts ETH recommends the

use of clamping hub couplings. The torque cell's shafts is supported in the enclosure housing with two ball bearings.

The size of the torque cell's housing depends on the rated torque. For the test rig in hands the selected torque cells' full scales torques are 30 Nm for input shaft and 50 Nm for output shaft. Both of these rated torques correspond to the housings side identified by DRVL-II. The maximum typical measurement error of these model is 0.1% of full scale [27]. However for these the DRVL-II size there is an optional feature corresponding to a maximum measurement error of 0.05% of full scale. These later option was selected for the test rig. With this the max measurement error from input shaft is 0.015 Nm, while for the output shaft is 0.025 Nm.

This torque cell model can be base mounted or flange mounted. In the cover housing of the load cells there is a small cavity to indicate the measuring side (Figure 4.2). In Table 4.1 is presented the serial codes of the selected torque cells.

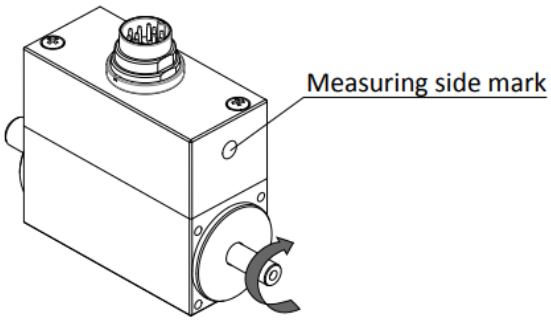

Figure 4.2: Measuring side and positive rotation of the DRVL torque cell

Table 4.1: Torque cells ordering codes

Shaft one load cell	DRVL-II-30-n-1
Shaft two load cell	DRVL-II-50-n-1

To take measurements a measurement chain is required for the torque cells. These is composed of the torque cells, connection cables, a power supply and an analyser.

The power supply is needed to supply the torque cells with the necessary voltage. The torque cells are fitted with a universal voltage input for the voltage range of 10 to 28,8 V.

The connection cables must be shielded and have low capacitance. The cables provided by ETH meet these requirements. Electrical and magnetics fields can disturb measurement circuits. These disturbances typically emanate from power lines placed parallel to the measurements cables, but can also be from nearby electric motors. The connection between the several components and the cables are done with 12 pin connectors. In Figures 4.3 and 4.4 is presented the 12 pin connector.

Analysers are needed to process the signals read in the load cells. The selected model is called ValueMasterBase also provided by ETH (Figure 4.5) [28]. The component can be used alongside with a computer to create a full-fledged measurement device. The measurement values can be displayed, evaluated according to pre-set limits and assessed graphically. The measured values are stored in a txt file and they can be compared to each other in several layers. Each of the components has two sensor connection to measuring torque, however only one of them can be used to measure speed and torque simultaneously. Therefore two of these components are needed.

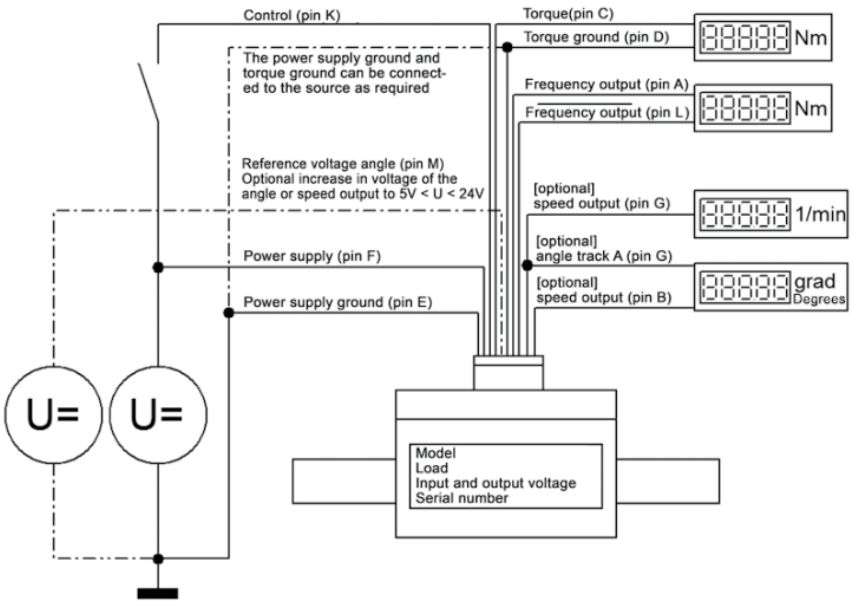

Figure 4.3: Electrical connections of the torque cells

Pin	Connection	AK12.3 F Color	AK12.3 DF Color
A	Frequency output	black	black
B	NC	red	red
C	Voltage output	brown	brown
D	Output ground	white	white
E	Power supply + speed ground	yellow	yellow
F	Power supply 9 - 28 V	purple	pink
G	Speed output	green	green/brown
H	Memory chip *only with ETH evaluation device	pink	purple
J	Ready output	grey	green/white
K	Control input	grey/pink	grey/pink
L	Frequency output inverted	red/blue	red/blue
M	NC	blue	blue

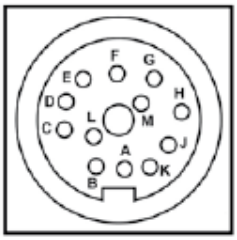

(Top view of transducer connector)

Figure 4.4: 12-pin connection of the load cells

Figure 4.5: ETH messtechnik's analyser

4.2 Couplings

The couplings selected for this project are provided by Siemens. As suggested by ETH the type of coupling selected is clamping hub coupling [27], as shown in Figure 4.6. This type of couplings are torsionally rigid couplings. The slotted clamping hub allows a frictionally engaged connection to the input and output shaft. A single tightening screw per hub ensures easy assembly. A keyway according to DIN 6885-1 can be selected additionally as an option. Table 4.2 presents the technical information of these components as well as the ordering codes.

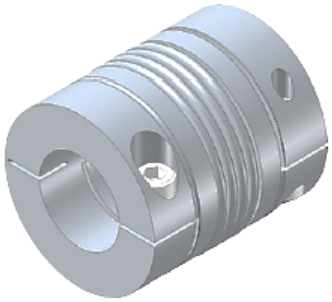

Figure 4.6: Siemens' clamping hub coupling

Table 4.2: Ordering number of Siemens' clamping hub couplings

Component	Quantity	D_1 mm	D_2 mm	Max torque Nm	Ordering code
Motors coupling	2	15	38	173	2LC0591-2AB99-0AA0-Z L9Y+M0V L0Y:$D_1 = 15$mm
Shafts coupling	2	15	35	173	2LC0591-2AB99-0AA0-Z L9Y+M0U L0Y:$D_1 = 15$mm

4.3 Shafts supports

For this project the chosen type of supports is the cast iron housing, radial insert ball bearing with adapter sleeve provided by Schaffler [29]. Figure 4.7 presents this component and Table 4.3 gives it's main characteristics.

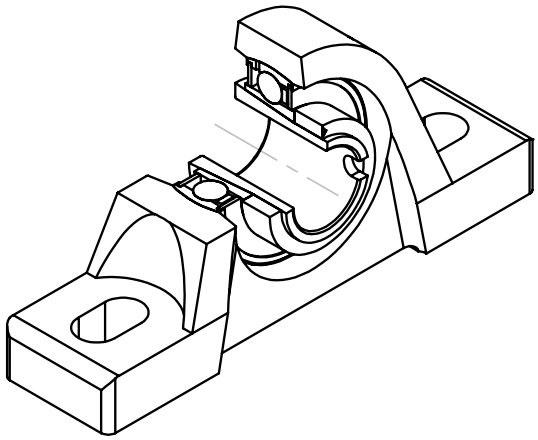

Figure 4.7: Schematic view of the type of supports selected

Table 4.3: RASEA35-XL-N main characteristics

RASEA35-XL-N		
Housing		ASE07
Bearing		GSH35-XL-2RSR-B
Bearing end cap		KASK07
d	[mm]	35
D	[mm]	72
C	[N]	26500
C_0	[N]	15700
f_0		13.8

This solution was selected for the following reasons:

1. There is no need to complex geometrical features such as steps in cross section or groves to retain rings. These geometric fetchers are synonymous with stress concentration factors that lead to bigger shafts cross section and a more complex overall solution.

2. In order to lock the shafts, the adapter sleeve compresses the shafts uniformly and with much more strength along its perimeter when compared with looking mechanisms based on a tightening screw perpendicular to the shaft's axis.

3. Its easy to mount and to incorporate in the test rig.

4. Its a ball bearing support. Of the various types of bearings, balls bearings are those that represent the smallest torque losses.

4.4 Power loss calculation

The main objective of the test rig is to evaluate the power loss in belt drives. For this the torque cells are used. The designed test rig does not measure directly the belt drive torque and speed losses, rather it measures the input and the output torques and speeds from the shafts. So to reach the belt drive torque loss, the input and output measures must be compared.

The comparation between the input and output torques must account for two factors:

1. Transmission ratio,
2. Torque loss in the shafts supports.

In total there are four bearings (identified from A to D in Figure 4.8) that constitute four torque losses between the measured quantities and the pulleys.

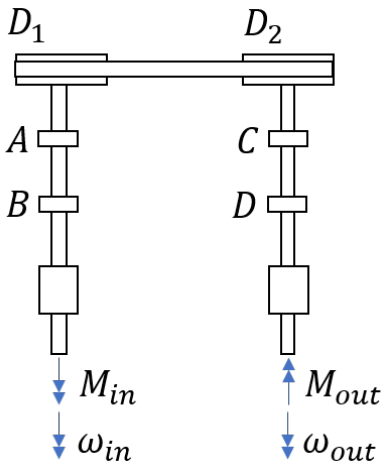

Figure 4.8: Sources of unwanted losses and measured quantities

The transmission ratio can be given as

$$i = \frac{D_2}{D_1} \tag{4.1}$$

while the input and output powers can be given as

$$P_{in} = \omega_{in} M_{in} \tag{4.2}$$

applying logarithms to the first expression leads to

$$\log P_{in} = \log \omega_{in} + \log M_{in} \tag{4.3}$$

after differentiation yields

$$\frac{dP_{in}}{P_{in}} = \frac{d\omega_{in}}{\omega_{in}} + \frac{dM_{in}}{M_{in}} \tag{4.4}$$

Although this is a differential equation it can be approximated for finite differences because the torque and speed losses are relativity small when compared with their corresponding nominal values [3]. This leads to

$$\frac{\Delta P_{in}}{P_{in}} = \frac{\Delta \omega_{in}}{\omega_{in}} + \frac{\Delta M_{in}}{M_{in}} \tag{4.5}$$

The only source of speed loss is due to the belt transmission. Therefore the measured speeds leads directly to the speed loss in the belt transmission and can be determined by

$$\frac{\Delta\omega_{in}}{\omega_{in}} = \frac{\omega_{in} - \omega_{out}/i}{\omega_{in}} \tag{4.6}$$

The difference in torque can be determined similarly and is given by

$$\Delta M_{in} = M_{in} - \frac{M_{out}}{i} \tag{4.7}$$

However the difference in torque is equal to the some of the several torque losses,

$$\Delta M_{in} = M_A + M_B + M_C + M_D + M_{bt} \tag{4.8}$$

where M_{bt} is the torque loss in the belt transmission and the rest corresponds to the torque losses in the four rolling (A,B,C and D, see Figure 4.8).

The several losses presented in the right hand side of the last equation are not known *a priori*. This leads to two possibilities of extracting knowledge from the test rig that are discussed bellow.

4.4.1 Comparative measure VS Absolute measure

The comparative measure consists in making tests where the reactions in the supports remain the same and therefore the torque losses are equal between tests. Whatever the losses in the roller bearings, as long as they remain the same between tests, conclusions can be made. For example, this can be done the comparing different types of belts or the efficiency of different number of belts. However this can not be done when the pre-tension, load, center distance and misalignments vary from test to test.

On the other hand the absolute measure permits to test the influence of each parameter regardless of the rolling bearings working conditions. In this case the absolute value of the torque losses in the rolling bearings must be at least estimated.

4.4.2 Calculation of rolling bearing torque losses

For this an empiric bearing loss model, made available by SKF in their catalogue, can be used [30]. This model considers that the total friction torque is the sum of four different physical sources of torque loss, represented by

$$M_t = M_{rr}^{'} + M_{sl} + M_{drag} + M_{seal} \tag{4.9}$$

Where $M_{rr}^{'}$ is the rolling frictional moment, M_{sl} is the sliding frictional moment, M_{seal} is the friction moment of the seals and M_{drag} is the friction moment of the drag losses which include churning, splashing, etc. The model present in there catalogue is in part replicated in their web site [31]. The SKF website does not replicate the empiric losses model for all bearings. For example it does not calculate losses for sealed bearings. The type of bearings present in the selected supports are insert bearings, characterized for having seals and an outer ring with an outside spherical contour. These are based on the sealed deep groove ball bearings in the 62 and 63 series. The closest deep grove ball bearings, without and with seals respectively, to the selected bearings are the 6207 and 6207-RS1, whose characteristics can be found in Table 4.4. Although the SKF web site is limited it was useful to concluded that the drag losses are negligible. To conclude this calculations were made with the values present in the Table 4.5. The values used are

Table 4.4: 6207 and 6207-2RS1 deep grove ball bearings characteristics

d	[mm]	35
D	[mm]	72
B	[mm]	17
C	[kN]	27
C0	[kN]	15.3

Table 4.5: SKF friction loss website calculation with 6207 bearing lubricated with grease

n	[rpm]	1000	3000
Fr	[N]	2500	2500
Fa	[N]	480	480
T	[°]	40	40
ν@40°	[cSt]	68	68
M_{sl}	[Nmm]	42.2	42.3
M_{drag}	[Nmm]	0	0

representative of supports reaction calculated during the design of the test rig. These will be discussed in the next chapter. In Table 4.5 are also presented the results. Strangely the SKF website does not provide values for the rolling frictional moment.

Disregarding the drag losses, the total internal friction torque of the rolling bearings have three contributions: the rolling, sliding and seal torques, respectively, $M_{rr}^{'}$, M_{sl} and M_{seal}, as represented by

$$M_t = M_{rr}^{'} + M_{sl} + M_{seal} \tag{4.10}$$

Equations (4.11)-(4.17) defines the rolling and sliding torques,

$$M_{rr}^{'} = \phi_{ish}.\phi_{rs}[G_{rr}(n.\upsilon)^{0,6}] \tag{4.11}$$

$$\phi_{ish} = \frac{1}{1 + 1.84 \times 10^{-9}(n.d_m)^{1.28}\nu^{0.64}} \tag{4.12}$$

$$\phi_{rs} = \frac{1}{e^{\left[K_{rs}\nu n(d+D)\sqrt{\frac{K_z}{2(D-d)}}\right]}} \tag{4.13}$$

$$M_{sl} = G_{sl}.\mu_{sl} \tag{4.14}$$

where n is the rotation speed, ν is the kinematic viscosity at the working temperature and d_m are is the mean diameter. The constants G_{sl}, G_{rr} are dependent on the geometry and given by

$$G_{rr} = R_1.{d_m}^{1.96}\left[F_r + \frac{R_2}{\sin(\alpha_f)}F_a\right]^{0.54} \tag{4.15}$$

$$G_{sl} = S_1.{d_m}^{-0.145}\left[{F_r}^5 + \frac{S_2.d_m^{1.5}}{sin(\alpha_f)}{F_a}^4\right]^{1/3} \tag{4.16}$$

$$\alpha_f = 24.6(F_a/C_0)^{0.24}[°] \tag{4.17}$$

where F_r and F_a are the radial and axial loads respectively. The sliding friction torque (Equation 4.18) is dependent on the weighting factor (Equation 4.19) and on the reference

values of the coefficient of friction (boundary film coefficient of friction – μ_{bl} and full film coefficient of friction – μ_{EHD}).

$$\mu_{sl} = \phi_{bl}.\mu_{bl} + (1 - \phi_{bl}).\mu_{EHD} \tag{4.18}$$

$$\phi_{bl} = \frac{1}{e^{2,6\times10^{-8}(n.\upsilon)^{1,4}d_m}} \tag{4.19}$$

SKF recommends $\mu_{bl} = 0.15$ as a general rule. On the other hand the μ_{EHL} depends on the bearing type and on the type of lubrication oil. For ball bearings μ_{EHL} is 0.05, 0.04 or 0.1 if the oil is mineral, synthetic or a transmission fluid respectively.

Table 4.6 presents the parameters, suited for the 6207-2RS1 bearing, needed for the calculation of the rolling and sliding torques.

Table 4.6: Parameters for seal torque loss of the 6207-2RS1

d	[mm]	35
D	[mm]	72
S_1		0.00323
S_2		36.5
R_1		3.9e-7
R_2		1.7
K_z		3.1
K_{rs}		6e-8

Equation (4.20) define the seals torque,

$$M_{seal} = K_{s1}.d_s^{\beta} + K_{s2} \tag{4.20}$$

Table 4.7 presents the parameters for this equation corresponding to the 6207-2RS1 bearing.

Table 4.7: Parameters for seal torque loss of the 6207-2RS1

K_{s1}	0.018
K_{s2}	20
β	2.25
d_s	46.9

With the model established , the values of M_A, M_B, M_C and M_D can be estimated function of the speed, loads and grease base oil viscosity at the working temperature of each bearing.

So M_{bt} can be given by

$$M_{bt} = M_{in} - \frac{M_{out}}{i} - M_A - M_B - M_C - M_D \tag{4.21}$$

With this the problem is closed and the power loss in the belt transmission can be given by

$$\frac{\Delta P_{bt}}{P_{in}} = \frac{\Delta\omega}{\omega_{in}} + \frac{M_{bt}}{M_{in}} \tag{4.22}$$

Chapter 5

Shafts design

In this section the design and calculation results of the shafts are presented. The bearings calculations are also presented. It starts with the presentation of the shafts geometry, followed by the calculation of the reactions and internal efforts and the analysis of their critical results. After this the shaft fatigue design is presented, where remarks about the shafts material are made and the fatigue calculation procedure and results are presented. It concludes with the presentation of the rolling bearings calculation procedure and results.

5.1 Shafts geometry

The shafts are responsible for transmitting/receiving power from pulleys and to support them. To exchange power between pulleys and shafts tapper bushes are used. These are mounted on the shaft's end with a keyway. To support each of the shafts, two radial ball bearing housing units are used. Figure 5.1 presents the overall solution to support the pulleys and the shafts. To insure that the pulleys are placed at the corrected distance

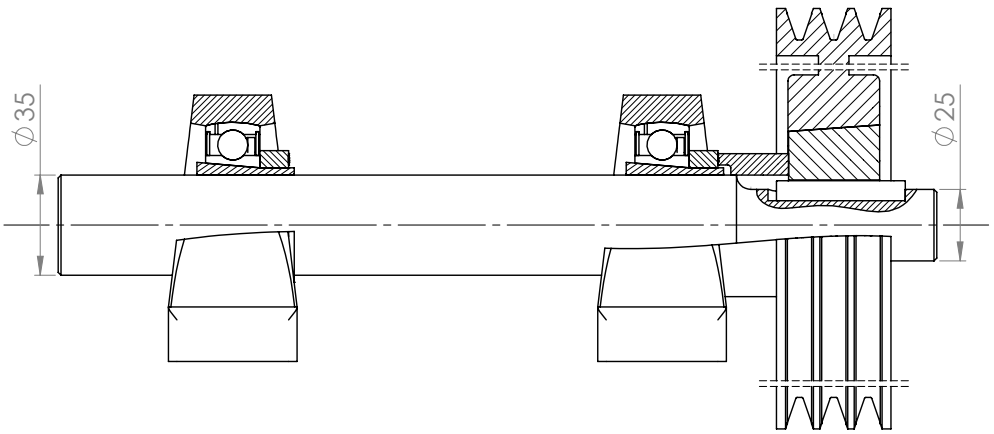

Figure 5.1: Shaft geometry and assembly in the test rig

form the near bearing house support a special design bushing is used. The shaft ends are designed according to NF E 22-051, which specifies a minimum length of 60 mm for shaft end with 25 mm of diameter, so a total length 65mm was selected. The shaft was designed to have a diameter of 35 mm. So that the supports are large enough in order to support

the reactions. Furthermore, the larger shaft's cross section ensures a larger stiffness.

5.2 Reaction loads and internal efforts

5.2.1 Calculation procedure of reaction loads and internal efforts

For the calculation of the support reaction loads the first step consists in the definition of the necessary frame of references. In total are needed three reference frames as shown in Figure 5.2. The first one is the inertial reference frame identified by the axis $Ox_0y_0z_0$ and its called s_0. The second and third ones correspond to the first and second shafts respectively, identified by $O_1x_1y_1z_1$ and $O_2x_2y_2z_2$ and are called s_1 and s_2 respectively. They accompany the respective shafts in everything except in their self axis rotations.

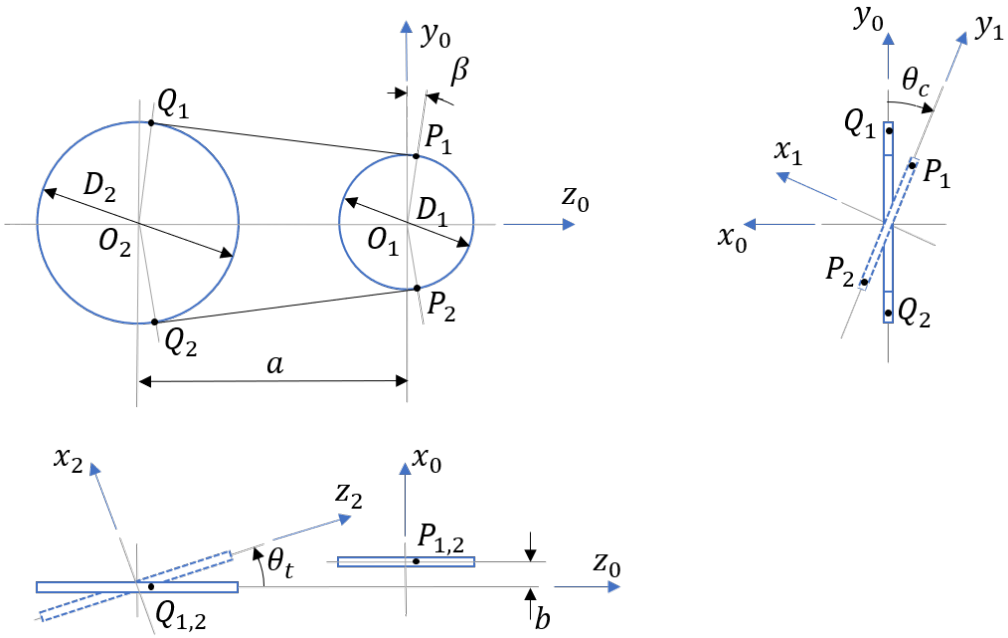

Figure 5.2: Reference frames needed for reactions and internal efforts calculation; Toe-θ_t; Camber-θ_c; Center distance-a; Axial offset-b

The first parameter important in this calculation corresponds to the angle β necessary to define the entering and leaving points of the belts in the pulleys, as shown in Figure 5.2. It is assumed that this parameter is independent of the misalignments, being given by

$$\beta = \sin^{-1} \frac{D_2 - D_1}{2a} \tag{5.1}$$

The positions of P_1 and P_2 can be defined in the frame of reference s_1 as

$$\overrightarrow{O_1P_{1,2}}|_{s1} = \frac{D_1}{2} \begin{Bmatrix} 0 \\ \pm\cos\beta \\ \sin\beta \end{Bmatrix} \tag{5.2}$$

The positions of Q_1 and Q_2 can be defined in the frame of reference s_2 as

$$\overrightarrow{O_2Q_{1,2}}|_{s2} = \frac{D_2}{2} \begin{Bmatrix} 0 \\ \pm\cos\beta \\ \sin\beta \end{Bmatrix} \tag{5.3}$$

The two forces that the belts exert on each pulley are defined in the directions of the belt entering and leaving the pulleys as shown in Figure 5.3. The direction associated to the top side of the belt is defined by the line connecting the point P_1 and Q_1, while the direction associated to the bottom side of the pulley is defined by the line connecting the points P_2 and P_3. The forces exerted on each pulley can be defined as

$$\overrightarrow{T_1}|_{s0} = T_1 \frac{\overrightarrow{P_1Q_1}|_{s0}}{||\overrightarrow{P_1Q_1}|_{s0}||} \qquad \overrightarrow{T_2}|_{s0} = T_2 \frac{\overrightarrow{P_2Q_2}|_{s0}}{||\overrightarrow{P_2Q_2}|_{s0}||} \tag{5.4}$$

where the scalers T_1 and T_2 are unknowns for now.

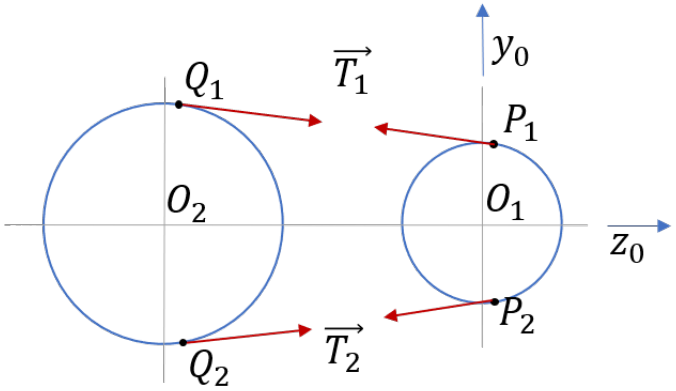

Figure 5.3: Forces exerted on each pulley

The points P_1 and P_2 are associated to a different reference frame than Q_1 and Q_2, however the definition of $\overrightarrow{T_1}$ and $\overrightarrow{T_2}$ must be in a common reference frame. The chosen reference frame for defining $\overrightarrow{T_1}$ and $\overrightarrow{T_2}$ was $Ox_0y_0z_0$. To fully define them the vectors $\overrightarrow{P_1Q_1}|_{s0}$ and $\overrightarrow{P_2Q_2}|_{s0}$ must be separated in

$$\overrightarrow{P_1Q_1}|_{s0} = \overrightarrow{P_1O_1}|_{s0} + \overrightarrow{O_1O_2}|_{s0} + \overrightarrow{O_2Q_1}|_{s0} \tag{5.5}$$

$$\overrightarrow{P_2Q_2}|_{s0} = \overrightarrow{P_2O_1}|_{s0} + \overrightarrow{O_1O_2}|_{s0} + \overrightarrow{O_2Q_2}|_{s0} \tag{5.6}$$

The vector $\overrightarrow{O_1O_2}|_{s0}$ is

$$\overrightarrow{O_1O_2}|_{s0} = \begin{Bmatrix} b \\ 0 \\ -a \end{Bmatrix} \tag{5.7}$$

Besides this vector, to define the vectors $\overrightarrow{P_1O_1}|_{s0}$ and $\overrightarrow{P_2O_1}|_{s0}$ it is necessary to define the transform matrix that converts entities defined in the reference frame s_1 into the reference frame s_0. For the vectors $\overrightarrow{O_2Q_1}|_{s0}$ and $\overrightarrow{O_2Q_2}|_{s0}$ the transform matrix from s_2 to s_0 is needed. This matrices are given by

$$[T_{10}] = \begin{bmatrix} \cos\theta_c & -\sin\theta_c & 0 \\ \sin\theta_c & \cos\theta_c & 0 \\ 0 & 0 & 1 \end{bmatrix} \qquad [T_{20}] = \begin{bmatrix} \cos\theta_t & 0 & \sin\theta_t \\ 0 & 1 & 0 \\ -\sin\theta_t & 0 & \cos\theta_t \end{bmatrix} \tag{5.8}$$

The needed vectors for the definition of $\overrightarrow{T_1}|_{s0}$ and $\overrightarrow{T_2}|_{s0}$ are constructed by

$$\overrightarrow{P_1O_1}|_{s0} = -[T_{10}] \cdot \overrightarrow{O_1P_1}|_{s1} \qquad \overrightarrow{O_2Q_1}|_{s0} = [T_{20}] \cdot \overrightarrow{O_2Q_1}|_{s2} \tag{5.9}$$

$$\overrightarrow{P_2O_1}|_{s0} = -[T_{10}] \cdot \overrightarrow{O_1P_2}|_{s1} \qquad \overrightarrow{O_2Q_2}|_{s0} = [T_{20}] \cdot \overrightarrow{O_2Q_2}|_{s2} \tag{5.10}$$

With the loading vectors fully established, the next step is to calculate the reaction loads of both shafts. For this, the free body diagram of shaft 1 and shaft 2, presented in Figure 5.3, are used. For shaft 1 the equations will be expressed in the reference frame s_1, while for the shaft 2 in the reference frame s_2.

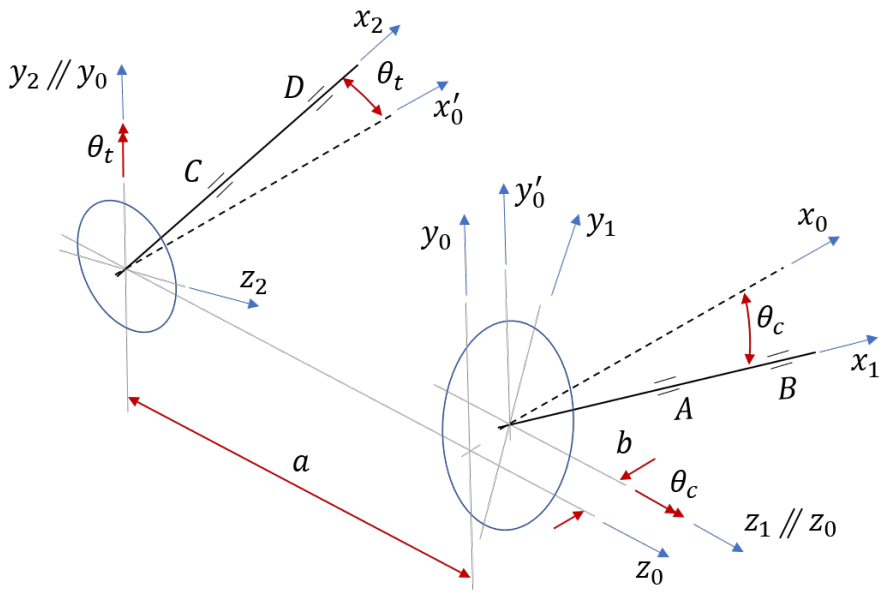

(a) Reference frames associated to each shaft; Toe-θ_t; Camber-θ_c; Center distance-a; Axial offset-b

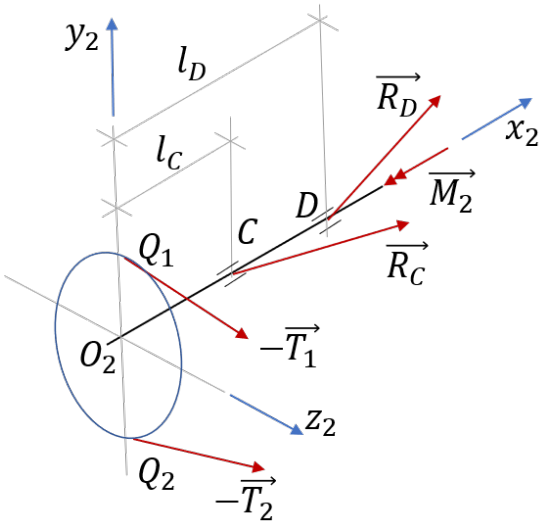

(b) Free body diagram of of shaft 2

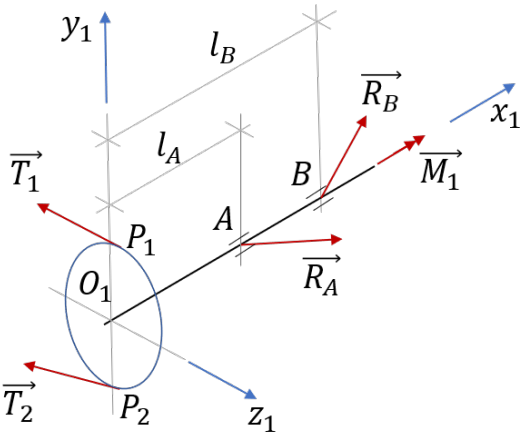

(c) Free body diagram of of shaft 1

Figure 5.4: Free body diagrams for reaction calculation

Before anything else, the loading vector $\overrightarrow{T_1}|_{s0}$ and $\overrightarrow{T_2}|_{s0}$ must be expressed in both

reference frames

$$\overrightarrow{T_1}|_{s1} = [T_{10}]^T \cdot \overrightarrow{T_1}|_{s0} \qquad \overrightarrow{T_2}|_{s1} = [T_{10}]^T \cdot \overrightarrow{T_2}|_{s0} \tag{5.11}$$

$$\overrightarrow{T_1}|_{s2} = [T_{20}]^T \cdot \overrightarrow{T_1}|_{s0} \qquad \overrightarrow{T_2}|_{s2} = [T_{20}]^T \cdot \overrightarrow{T_2}|_{s0} \tag{5.12}$$

The torques $\overrightarrow{M_1}|_{s1}$ and $\overrightarrow{M_2}|_{s2}$ applied in shafts correspond to the input and output efforts imposed by the motors. They are defined in the respective reference frame by

$$\overrightarrow{M_1}|_{s1} = \begin{Bmatrix} m\omega M_1 \\ 0 \\ 0 \end{Bmatrix} \qquad \overrightarrow{M_2}|_{s2} = \begin{Bmatrix} -m\omega M_2 \\ 0 \\ 0 \end{Bmatrix} \tag{5.13}$$

The value of ω is equal to 1 if the shafts are rotating in the positive direction and is equal to -1 if they are rotating in the negative direction. The value of m is equal to 1 if the machine M1 is working as motor and machine M2 is working as a generator. If the machine M1 is working as generator and machine M2 is working as motor the value of m is equal to -1. Since the loading motor operates in torque control mode, the value of the loading moment, $\overrightarrow{M_1}|_{s1}$ or $\overrightarrow{M_2}|_{s2}$ depending on which machine is working as load, is known *a priori*, while the input torque is for now an unknown.

The construction of the shafts and the way they work with their respective supports is such that forces in the axial direction are all absorbed in the supports closer to the pulleys. The unknown reactions can be identified by

$$\overrightarrow{R_A}|_{s1} = \begin{Bmatrix} R_A^x \\ R_A^y \\ R_A^z \end{Bmatrix} \quad \overrightarrow{R_B}|_{s1} = \begin{Bmatrix} R_B^x \\ R_B^y \\ 0 \end{Bmatrix} \quad \overrightarrow{R_C}|_{s2} = \begin{Bmatrix} R_C^x \\ R_C^y \\ R_C^z \end{Bmatrix} \quad \overrightarrow{R_D}|_{s2} = \begin{Bmatrix} R_D^x \\ R_D^y \\ 0 \end{Bmatrix} \tag{5.14}$$

For shaft 1, the force equilibrium and torque equilibrium in point A leads to

$$\Sigma \overrightarrow{M_A}|_{s1} = 0 : \overrightarrow{AP_1}|_{s1} \times \overrightarrow{T_1}|_{s1} + \overrightarrow{AP_2}|_{s1} \times \overrightarrow{T_2}|_{s1} + \overrightarrow{AB}|_{s1} \times \overrightarrow{R_B}|_{s1} + \overrightarrow{M_1}|_{s1} = 0 \tag{5.15}$$

$$\Sigma \overrightarrow{F}|_{s1} = 0 : \overrightarrow{T_1}|_{s1} + \overrightarrow{T_2}|_{s1} + \overrightarrow{R_A}|_{s1} + \overrightarrow{R_B}|_{s1} = 0 \tag{5.16}$$

Where $\overrightarrow{AP_1}|_{s1}$, $\overrightarrow{AP_2}|_{s1}$ and $\overrightarrow{AB}|_{s1}$ are defined by

$$\overrightarrow{AP_1}|_{s1} = \overrightarrow{AO_1}|_{s1} + \overrightarrow{O_1P_1}|_{s1} \qquad \overrightarrow{AP_2}|_{s1} = \overrightarrow{AO_1}|_{s1} + \overrightarrow{O_1P_2}|_{s1} \tag{5.17}$$

$$\overrightarrow{AO_1}|_{s2} = \begin{Bmatrix} -l_A \\ 0 \\ 0 \end{Bmatrix} \qquad \overrightarrow{AB}|_{s2} = \begin{Bmatrix} l_B - l_A \\ 0 \\ 0 \end{Bmatrix} \tag{5.18}$$

For shaft 2, the force equilibrium and torque equilibrium in point C leads to

$$\Sigma \overrightarrow{M_C}|_{s2} = 0 : \overrightarrow{CQ_1}|_{s2} \times \overrightarrow{-T_1}|_{s2} + \overrightarrow{CQ_2}|_{s2} \times \overrightarrow{-T_2}|_{s2} + \overrightarrow{CD}|_{s2} \times \overrightarrow{R_D}|_{s2} + \overrightarrow{M_2}|_{s2} = 0 \tag{5.19}$$

$$\Sigma \overrightarrow{F}|_{s2} = 0 : \overrightarrow{-T_1}|_{s2} + \overrightarrow{-T_2}|_{s2} + \overrightarrow{R_C}|_{s2} + \overrightarrow{R_D}|_{s2} = 0 \tag{5.20}$$

Where $\overrightarrow{CQ_1}|_{s2}$, $\overrightarrow{CQ_2}|_{s2}$ and $\overrightarrow{CD}|_{s2}$ are defined by

$$\overrightarrow{CQ_1}|_{s2} = \overrightarrow{CO_2}|_{s2} + \overrightarrow{O_2Q_1}|_{s2} \qquad \overrightarrow{CQ_2}|_{s2} = \overrightarrow{CO_2}|_{s2} + \overrightarrow{O_21_2}|_{s2} \tag{5.21}$$

$$\overrightarrow{CO_2}|_{s2} = \begin{Bmatrix} -l_C \\ 0 \\ 0 \end{Bmatrix} \qquad \overrightarrow{CD}|_{s2} = \begin{Bmatrix} l_D - l_C \\ 0 \\ 0 \end{Bmatrix} \tag{5.22}$$

The force equilibrium and torque equilibrium in shafts 1 and 2 leads to twelve independent equations, however the number of unknowns is 13, $3R_A$, $2R_B$, $3R_C$, $2R_D$, T_1, T_2 and M_1 or M_2. The last equation necessary to close the problem consists in the impose pre-tension on the belt, that can be given by

$$-T_i = \overrightarrow{T_1^z}|_{s0} + \overrightarrow{T_2^z}|_{s0} \tag{5.23}$$

Where T_i is imposed *a priori*. The fact that this last equation has to be written in the reference frame s_0 is the justification that led previously to defining $\overrightarrow{T_1}$ and $\overrightarrow{T_2}$ in this axis systems.

Having established the calculation procedure for the reactions, the internal efforts can now be defined. Considering Figure 5.5, the torque equilibrium in the section S of the shaft 1 leads to

$$\overrightarrow{0} = \begin{cases} \overrightarrow{M}|_{s1} + \overrightarrow{SP_1}|_{s1} \times \overrightarrow{T_1}|_{s1} + \overrightarrow{SP_2}|_{s1} \times \overrightarrow{T_2}|_{s1} & x \leq l_A \\ \overrightarrow{M}|_{s1} + \overrightarrow{SP_1}|_{s1} \times \overrightarrow{T_1}|_{s1} + \overrightarrow{SP_2}|_{s1} \times \overrightarrow{T_2}|_{s1} + \overrightarrow{SA}|_{s1} \times \overrightarrow{R_A}|_{s1} & l_A \leq x \leq l_B \\ \overrightarrow{M}|_{s1} + \overrightarrow{SP_1}|_{s1} \times \overrightarrow{T_1}|_{s1} + \overrightarrow{SP_2}|_{s1} \times \overrightarrow{T_2}|_{s1} + \overrightarrow{SA}|_{s1} \times \overrightarrow{R_A}|_{s1} + \overrightarrow{SB}|_{s1} \times \overrightarrow{R_B}|_{s1} & x \geq l_B \end{cases} \tag{5.24}$$

Where $\overrightarrow{SP_1}|_{s1}$, $\overrightarrow{SP_2}|_{s1}$, $\overrightarrow{M}|_{s1}$, $\overrightarrow{SA}|_{s1}$ and $\overrightarrow{SB}|_{s1}$ are obtained by

$$\overrightarrow{SP_1}|_{s1} = \overrightarrow{SO_1}|_{s1} + \overrightarrow{O_1P_1}|_{s1} \qquad \overrightarrow{SP_2}|_{s1} = \overrightarrow{SO_1}|_{s1} + \overrightarrow{O_1P_2}|_{s1} \tag{5.25}$$

$$\overrightarrow{SO_1}|_{s1} = \begin{Bmatrix} -x \\ 0 \\ 0 \end{Bmatrix} \quad \overrightarrow{M}|_{s1} = \begin{Bmatrix} M^x \\ M^y \\ M^z \end{Bmatrix} \quad \overrightarrow{SA}|_{s1} = \begin{Bmatrix} l_A - x \\ 0 \\ 0 \end{Bmatrix} \quad \overrightarrow{SB}|_{s1} = \begin{Bmatrix} l_B - x \\ 0 \\ 0 \end{Bmatrix} \tag{5.26}$$

The same procedure when applied to shaft 2 leading to

$$\overrightarrow{0} = \begin{cases} \overrightarrow{M}|_{s2} + \overrightarrow{SQ_1}|_{s2} \times \overrightarrow{-T_1}|_{s2} + \overrightarrow{SQ_2}|_{s2} \times \overrightarrow{-T_2}|_{s2} & x \leq l_C \\ \overrightarrow{M}|_{s2} + \overrightarrow{SQ_1}|_{s2} \times \overrightarrow{-T_1}|_{s2} + \overrightarrow{SQ_2}|_{s2} \times \overrightarrow{-T_2}|_{s2} + \overrightarrow{SC}|_{s2} \times \overrightarrow{R_C}|_{s2} & l_C \leq x \leq l_D \\ \overrightarrow{M}|_{s2} + \overrightarrow{SQ_1}|_{s2} \times \overrightarrow{-T_1}|_{s2} + \overrightarrow{SQ_2}|_{s2} \times \overrightarrow{-T_2}|_{s2} + \overrightarrow{SC}|_{s2} \times \overrightarrow{R_C}|_{s2} + \overrightarrow{SD}|_{s2} \times \overrightarrow{R_D}|_{s2} & x \geq l_D \end{cases} \tag{5.27}$$

Where $\overrightarrow{SQ_1}|_{s2}$, $\overrightarrow{SQ_2}|_{s2}$, $\overrightarrow{M_1}|_{s2}$, $\overrightarrow{SC}|_{s2}$ and $\overrightarrow{SD}|_{s2}$ are obtained by

$$\overrightarrow{SQ_1}|_{s2} = \overrightarrow{SO_2}|_{s2} + \overrightarrow{O_2Q_1}|_{s2} \qquad \overrightarrow{SQ_2}|_{s2} = \overrightarrow{SO_2}|_{s2} + \overrightarrow{O_2Q_2}|_{s2} \tag{5.28}$$

$$\overrightarrow{SO_2}|_{s2} = \begin{Bmatrix} -x \\ 0 \\ 0 \end{Bmatrix} \quad \overrightarrow{M}|_{s2} = \begin{Bmatrix} M^x \\ M^y \\ M^z \end{Bmatrix} \quad \overrightarrow{SC}|_{s2} = \begin{Bmatrix} l_C - x \\ 0 \\ 0 \end{Bmatrix} \quad \overrightarrow{SD}|_{s2} = \begin{Bmatrix} l_D - x \\ 0 \\ 0 \end{Bmatrix} \tag{5.29}$$

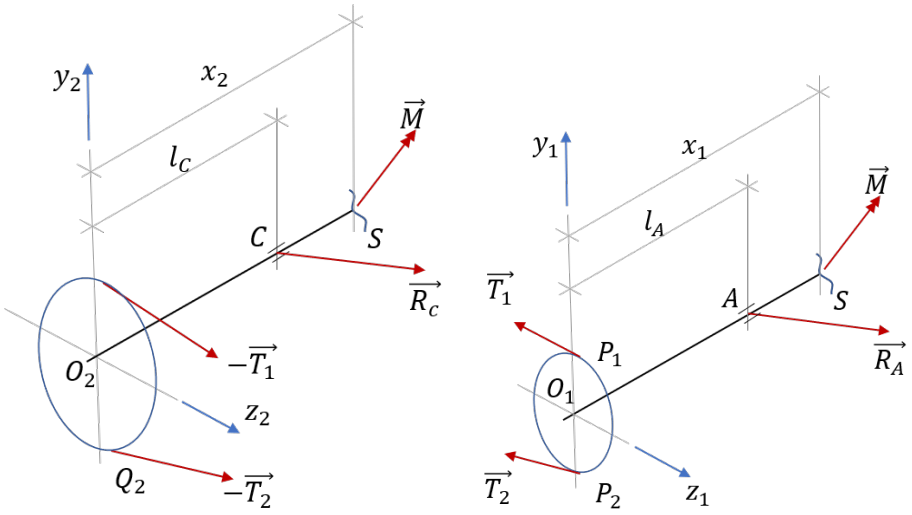

(a) Shaft 2 (b) Shaft 1

Figure 5.5: Free body diagrams with generic boundary exposed cross section

In total there's three unknowns for each shaft M^x, M^y and M^z, functions of x, which can be determined directly from the equilibrium of moments in the three spatial directions.

With the M^y and M^z, the maximum bending effort can be easily derived from

$$M_b = \sqrt{M^{y2} + M^{z2}} \tag{5.30}$$

The same goes for the supports reaction in the radial direction R^r, that can be given, for point A for example, as following

$$R_A^r = \sqrt{R_A^{y\,2} + R_A^{z\,2}} \tag{5.31}$$

5.2.2 Reactions results and efforts diagrams

In this section the numerical results of the supports reactions and shafts efforts diagrams, needed for bearings calculation and shafts design respectively, are presented.

The test rig will be able to vary the following parameters from test to test:

- Pulleys Diameters $(D_1; D_2)$
- Linear degrees of freedom $(a; b)$
- Angular degrees of freedom $(\theta_t; \theta_c)$
- Loading conditions $(M_r; T_i)$
- Motor operating conditions $(\omega; m, n_{in})$

Due to the large number of possible combinations, varying one factor at a time would be inefficient, so the following was considered.

- a was set to its minimum possible value.
- T_i was set to it's maximum value.

- ω was set to 1. For the purpose of reactions calculation this parameter has no interference in it's magnitude.
- m was set to 1. Expected normal operating condition.

The distance between the shafts supports are defined in Table 5.1.

Table 5.1: Distances between shafts supports and pulleys

Parameter		Value
L_A	[mm]	60
L_B	[mm]	205
L_C	[mm]	60
L_D	[mm]	205

In total the results are divided in three parts:

- Part one for the shafts design under dynamic conditions,
- Part two for the static bearing calculation and,
- Part three for the life bearing calculation.

For part one the following was considered:

- D_1 and D_2 were set to 67 and 224 mm respectively, this corresponds to the maximum transmission ratio possible;
- M_r was set to the maximum value possible, function of the transition ratio, without overloading any of the motors.

For part two the following was considered:

- D_1 and D_2 were set to 67 and 224 mm respectively, this corresponds to the maximum transmission ratio possible;
- M_r was set to 0. This situation corresponds to when the pre-tension is already applied but the motors are not running.

For part three the following was considered:

- D_1 and D_2 were set both to 224 mm;
- n_{in} was set to the rated speed of 3000 rpm. Although the speed is not needed for the reaction calculation, it is needed for the bearing life calculations;
- M_r was set to the maximum value possible, function of the transition ratio, without overloading any of the motors.

For the three parts the misalignments were set, one at a time, either to zero or to the end of scale value and the calculations were made.

The complete results of all of the reaction values for all the parts are presented in Appendix C. In all of the three parts the supports A and C present higher reaction loads then supports B and D. Tables 5.2, 5.3 and 5.4 present the critical reactions of part one, two and three respectively. The critical results correspond to the maximum axial and

radial reactions on each support. The calculations corresponding to no misalignments are also presented as comparative examples.

The free body diagrams of the shafts are present in figures 5.6 to 5.11. These correspond to the critical results of part one. For shaft one the critical diagrams correspond to the calculations number 1.5 and 1.6. On the other hand for shaft two correspond the calculations 1.3 and 1.6.

Table 5.2: Part one of reactions results: for shafts design

Cal.		1.1	1.3	1.5	1.6
D_1	[m]	0.067	0.067	0.067	0.067
D_2	[m]	0.224	0.224	0.224	0.224
a	[m]	0.5	0.5	0.5	0.5
b	[m]	0	0	0.05	0.05
θ_t	[°]	0	15	0	0
θ_c	[°]	0	0	0	-90
T_i	[N]	1800	1800	1800	1800
M_r	[Nm]	47	47	47	47
T_1	[N]	1121	1129	1127	1149
T_2	[N]	701.5	693.7	705.1	713
R_A^x	[N]	0	-16.78	184.5	93.02
R_A^y	[N]	-93.15	-97.38	-83.45	393.4
R_A^z	[N]	2545	2544	2552	2548
R_A^r	[N]	2547	2546	2553	2578
R_C^x	[N]	0	482.1	-184.5	-212.4
R_C^y	[N]	93.15	184.3	60.73	6.284
R_C^z	[N]	-2545	-2394	-2567	-2571
R_C^r	[N]	2547	2401	2568	2571

Table 5.3: Part two of reactions results: for static bearings calculation

Cal.		2.1	2.4	2.5	2.6
D_1	[m]	0.067	0.067	0.067	0.067
D_2	[m]	0.224	0.224	0.224	0.224
a	[m]	0.5	0.5	0.5	0.5
b	[m]	0	0	0.05	0.05
θ_t	[°]	0	15	0	0
θ_c	[°]	0	-90	0	-90
T_i	[N]	1800	1800	1800	1800
M_r	[Nm]	0	0	0	0
T_1	[N]	911.3	908.1	916	935.5
T_2	[N]	911.3	941.6	916	923.4
R_A^x	[N]	0	-7.154	184.5	1.13e-14
R_A^y	[N]	0	66.29	0	354.1
R_A^z	[N]	2545	2545	2552	2545
R_A^r	[N]	2545	2545	2552	2569
R_C^x	[N]	0	484.1	-184.5	-184.5
R_C^y	[N]	0	-106.4	0	-93.15
R_C^z	[N]	-2545	-2392	-2567	-2567
R_C^r	[N]	2545	2395	2567	2569

Table 5.4: Part three of reactions results: for life bearings calculation

Cal.		3.1	3.3	3.6	3.7
D_1	[m]	0.224	0.224	0.224	0.224
D_2	[m]	0.224	0.224	0.224	0.224
a	[m]	0.5	0.5	0.5	0.5
b	[m]	0	0	0.05	0.05
θ_t	[°]	0	15	0	15
θ_c	[°]	0	0	-90	0
T_i	[N]	1800	1800	1800	1800
M_r	[Nm]	18.33	18.33	18.33	18.33
T_1	[N]	981.8	984.7	1055	987.4
T_2	[N]	818.2	815.3	844.6	821.6
R_A^x	[N]	0	0	36.66	180
R_A^y	[N]	0	0	617.7	12.75
R_A^z	[N]	2545	2545	2545	2545
R_A^r	[N]	2545	2545	2619	2545
R_C^x	[N]	0	465.9	-216.7	292
R_C^y	[N]	0	33.87	-272.2	20.68
R_C^z	[N]	-2545	-2458	-2545	-2524
R_C^r	[N]	2545	2458	2559	2524

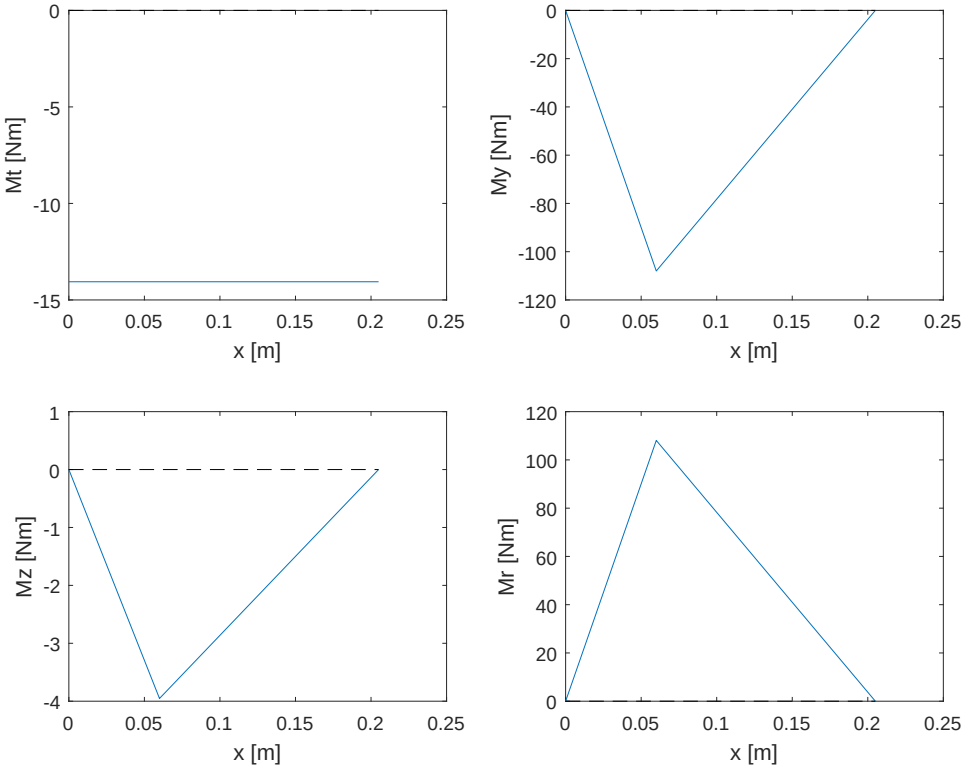

Figure 5.6: First shaft's efforts diagrams of calculation number 1.1

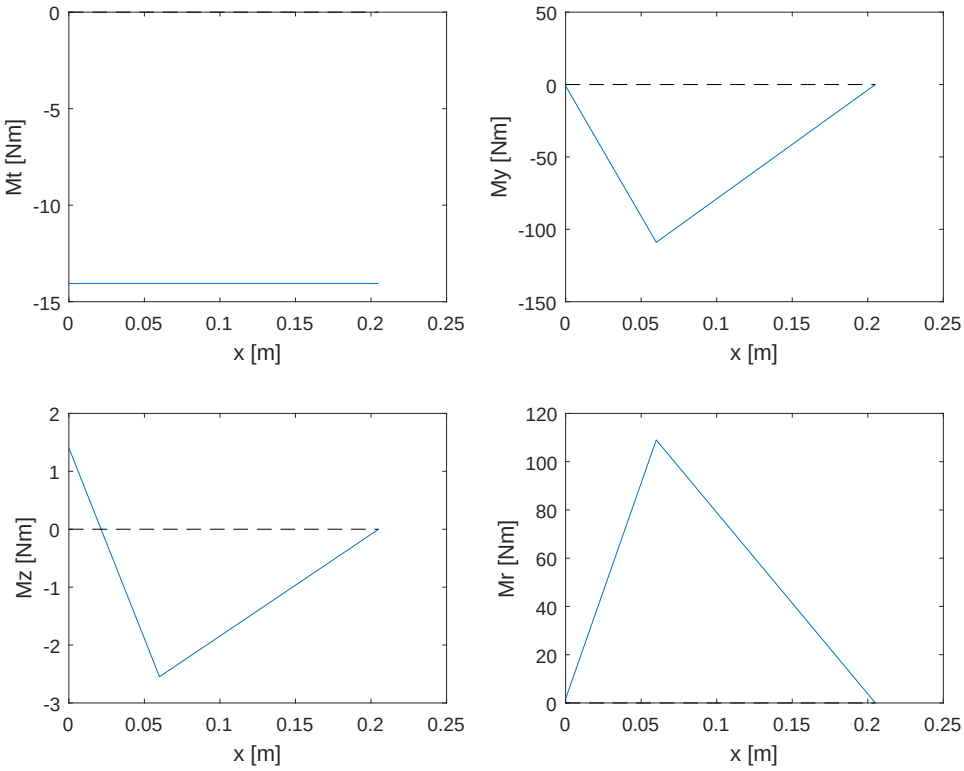

Figure 5.7: First shaft's efforts diagrams of calculation number 1.5

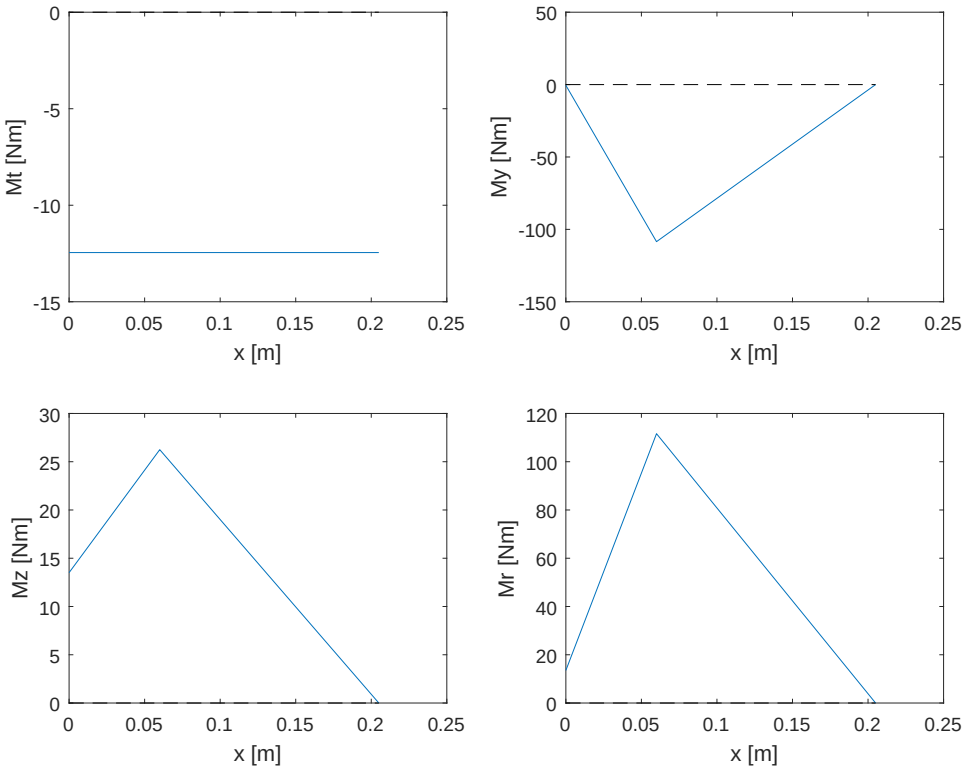

Figure 5.8: First shaft's efforts diagrams of calculation number 1.6

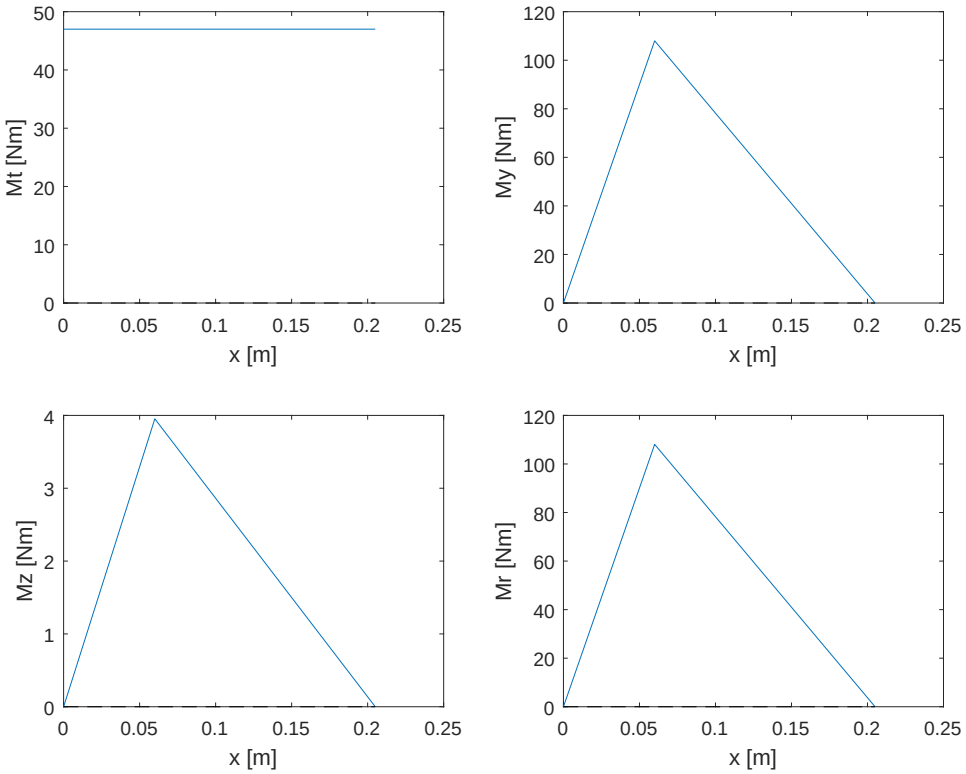

Figure 5.9: Second shaft's efforts diagrams of calculation number 1.1

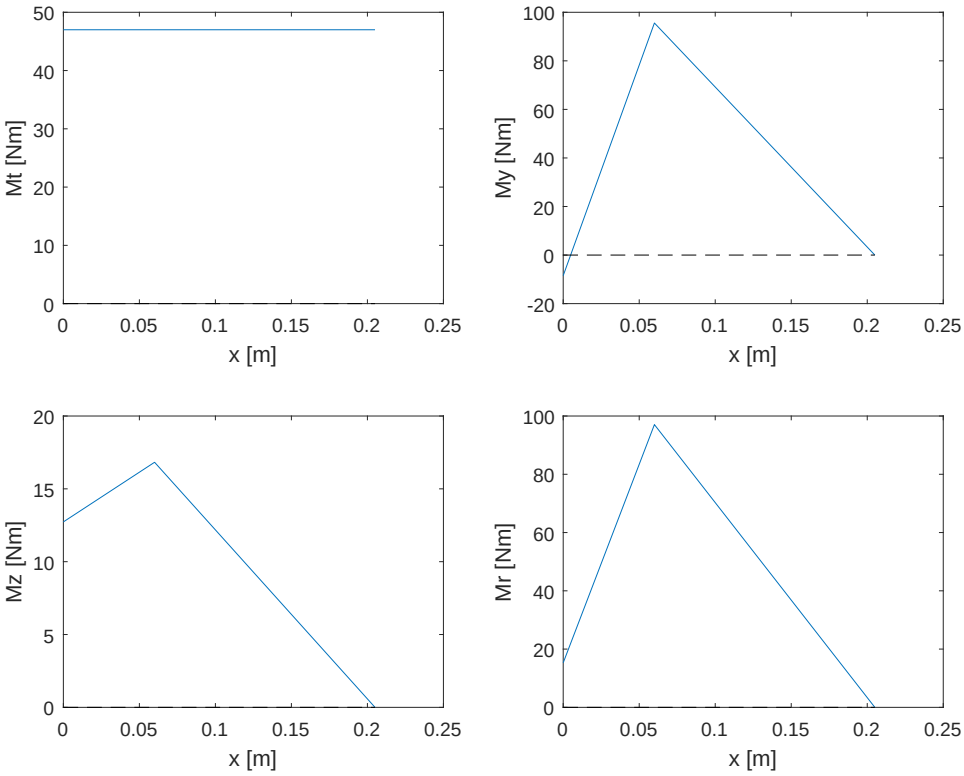

Figure 5.10: Second shaft's efforts diagrams of calculation number 1.3

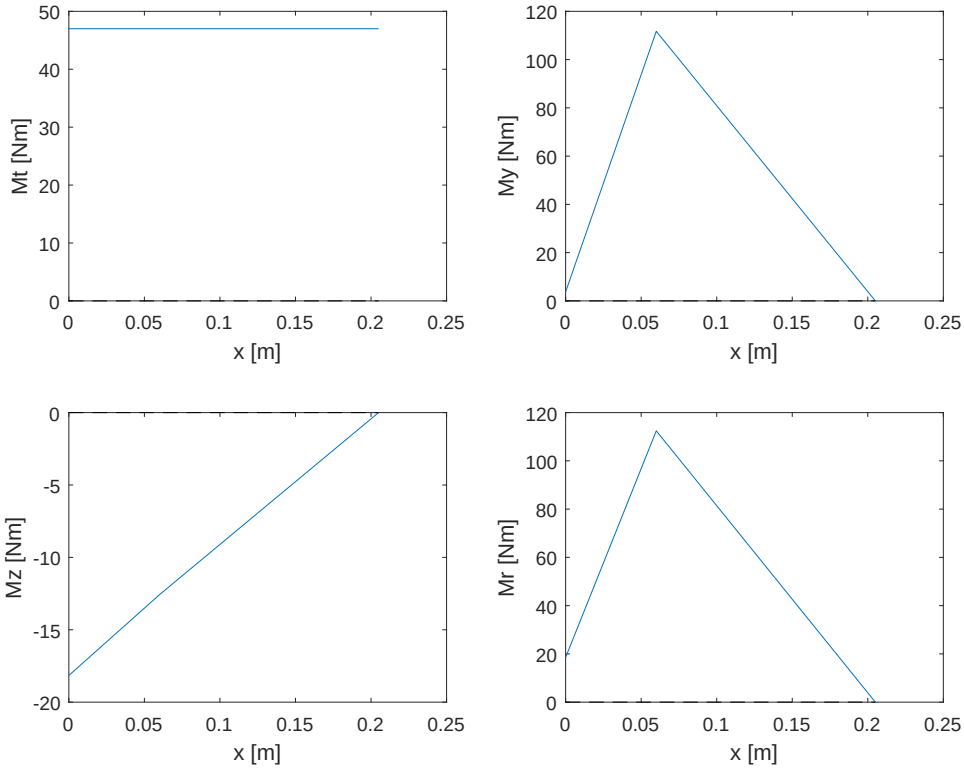

Figure 5.11: Second shaft's efforts diagrams of calculation number 1.6

5.3 Shafts fatigue design

In this section the aspects related to the mechanical strength of the shafts will be discussed. The material of the shafts, the calculations performed and, finally, the results. The shafts fatigue calculation was done following the book Fundamentals of Machine Component Design form Robert C. Juvinall [1].

Figure 5.12 shows the final drawing of the shafts, after an iterative design process, as well as the distance from the center of the pulley to the stress concentration factors.

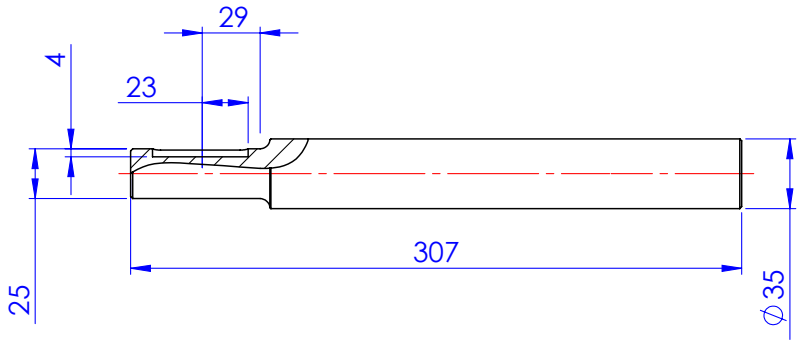

Figure 5.12: Final drawing of the shafts

5.3.1 Shafts material

The choice of the material of the shafts is an important aspect for the dimensioning, since the ultimate fatigue stress and the yield stress depend directly on the material selected.

In this application the shafts will be load primarily with bending and torsion, which is normal in power transmission applications. However, the shafts will be subject to some wear when mounting and dismounting the pulley's taper bushings. In order to prevent, or at least minimize, this wear the surface of the shafts must present a high hardness. To achieve this, either the stock material have a high hardness *a priori* before machining or a surface treatment must be applied to the shafts after machining. The second alternative with a diffusion nitriding heat treatment was selected because it permits the machining of the shafts in a softer metallurgic state and the final product will be rust resistant.

For selecting the material the Ramada Aços catalogue was used [32]. Among the steels recommended for surface treatment, the corresponding mechanical properties and recommended applications ware considering. The selected steel is called G 15 Special and it was selected because it presented the best mechanical proprieties (Table 5.5) and is supplied in a fully annealed state.

Table 5.5: G15 special main mechanical properties

Ramada Aços	DIN	σ_y [MPa]	σ_u [MPa]	A %
G 15 Special	18 CrNiMo 7-6	735	784	9

According to Ramada Aços catalogue the final hardness resulting from a nitriding heat treatment process in pre-treated steels is between 650-900 HV and the thickness of the hardened layer is between 0.1 and 0.2 mm [33].

For steels the ultimate fatigue stress σ_{f_0} can be estimated as half of the ultimate stress σ_u [1], that is $\sigma_{f_0} = 392$ [Mpa]. This value is obtained using a 0.3 inch diameter specimen with a polished surface in a rotating bending test (without average stress component). For an accurate design of the shafts it is necessary to correct this value according to the type of load, diameter and surface finish. The following equation is used:

$$\sigma_{f_0}^c = \sigma_{f_0} C_L C_G C_S C_T \tag{5.32}$$

were C_L, C_G, C_S and C_T are factor contemplating respectively the effects of load, size, surface finishing and temperature. For alternative bending efforts C_L is equal to 1. For shafts diameters between 10 and 50 mm C_G is equal to 0.9. The surface finishing factor is obtain from Figure 5.13. For the chosen steel C_S is approximately 0.75. For a working

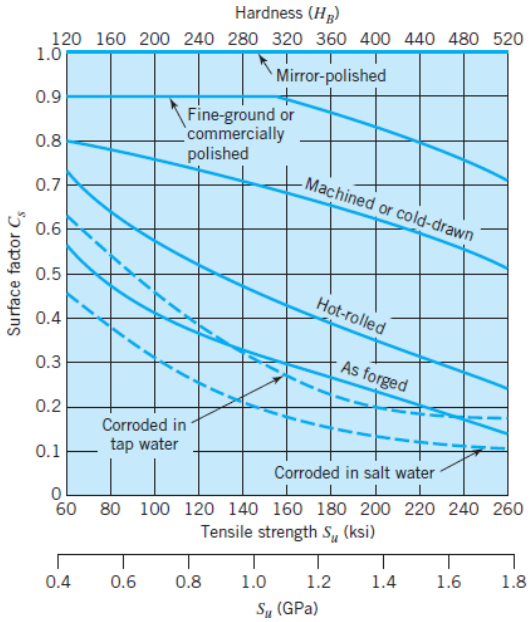

Figure 5.13: Ultimate fatigue stress reduction due to surface finish for steel parts [1]

condition at room temperature the factor C_T is equal to 1. The value of $\sigma_{f_0}^c$ is therefore given by $\sigma_{f_0}^c = 264.6$[MPa].

5.3.2 Fatigue calculation procedure

Due to the presence of simultaneous torsion and bending efforts, that are static and alternating respectively. The criteria of the equivalent static loading is used that has as its starting point the Soderberg criteria that can be established as:

$$\frac{\sigma_a}{\sigma_{f_0}} + \frac{\sigma_m}{\sigma_y} \leq \frac{1}{sc} \tag{5.33}$$

where σ_a and σ_m are respectively the alternating and mean stress and sc is the safety coefficient. Multiplying this expression by σ_y lead to

$$\frac{\sigma_a}{\sigma_{f_0}} \sigma_y + \sigma_m \leq \frac{\sigma_y}{sc} \tag{5.34}$$

For this expression to be used, it needs to be corrected in two features. The first is to replace σ_{f_0} with $\sigma^c_{f_0}$ and was covered in the previous section. The second is due to the existence of geometric discontinuities that cause stress concentrations, which aggravates the resistance of the shaft locally. This issue is taken into account with the introduction of the fatigue stress concentrator factor K_f, that multiplied by the alternating stress, gives:

$$K_f \frac{\sigma_a}{\sigma^c_{f_0}} \sigma_y + \sigma_m \leq \frac{\sigma_y}{sc} \tag{5.35}$$

In this expression the left-hand side is the equivalent static load.

$$\sigma^{eq}_{st} = K_f \times \frac{\sigma_a}{\sigma^c_{f_0}} \times \sigma_y + \sigma_m \tag{5.36}$$

However, the torsion efforts were not considered yet. For this the Tresca criteria was use and can be stated for this case as

$$\sqrt{\frac{(\sigma^{eq}_{st})^2}{4} + (\tau^{eq}_{st})^2} = \tau_{max} \leq \frac{\sigma_y}{2sc} \tag{5.37}$$

where τ_{max} is the maximum shear stress. τ^{eq}_{st} can be obtained the same way as σ^{eq}_{st}, however it is not necessary since in this work the torsion efforts are constant, being characterized by only a mean component τ_m.

The expressions of σ_a, σ_m and τ_m are defined as following

$$\sigma_a = \frac{d}{2}\frac{M_f}{I}; I = \frac{\pi d^4}{64}; \sigma_m = \frac{N}{A}; A = \frac{\pi d^2}{4} \tag{5.38}$$

$$\tau_m = \tau^{eq}_{st} = \frac{d}{2}\frac{M_t}{I_p}, I_p = \frac{\pi d^4}{32} \tag{5.39}$$

where M_f, N, M_t are respectively the alternating bending torque, the axial effort and the torsion torque shown in Figures 5.6 to 5.11. Replacing these last expression in the Tresca criteria leads to

$$\sqrt{\frac{(K_f \frac{d}{2}\frac{M_f}{I}\frac{\sigma_y}{\sigma_{f_0}} + \frac{N}{A})^2}{4} + (\frac{d}{2}\frac{M_t}{I_p})^2} \leq \frac{\sigma_y}{2sc} \tag{5.40}$$

The fatigue stress concentration factor K_f is a parameter that depends on the notch sensitivity factor q and the theoretical or geometrical stress concentrator factor K_t. The expression that relates these factors is

$$K_f = 1 + q(K_t - 1) \tag{5.41}$$

The theoretical stress concentrator factor is a parameter that depends on the type of load and the type of geometry discontinuity. The two shafts have geometry discontinuities are the shafts diameter variation and key slots. The values of K_t for these two types of geometric discontinuity can be found in Peterson's Stress Concentration Factors [34]. For shafts diameter variations and key slots the expression present in Figures 5.14 and 5.15 can be used. On the other hand, the notch sensitivity factor can be estimated using Figure 5.16

Given the expected high hardness of the steel after surface treatment, the notch sensitivity factor was set to 1.

With al the involved parameters clarified it is possible to transform the Tresca expression in to an equation and calculate the safety coefficient for a given a load and geometry.

$$sc = \frac{\sigma_y}{\sqrt{\frac{(kf \frac{d}{2}\frac{M_f}{I}\frac{\sigma_y}{\sigma_{f_0}} + \frac{N}{A})^2}{4} + (\frac{d}{2}\frac{M_t}{I_p})^2}} \tag{5.42}$$

2.
Shoulder fillet in stepped circular shaft

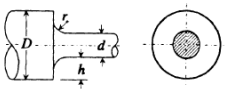

b. Bending

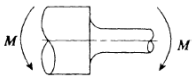

$$\sigma_{\max} = K_t \sigma_{\text{nom}}, \qquad \sigma_{\text{nom}} = 32M/\pi d^3$$

$$K_t = C_1 + C_2 \frac{2h}{D} + C_3 \left(\frac{2h}{D}\right)^2 + C_4 \left(\frac{2h}{D}\right)^3$$

	$0.1 \le h/r \le 2.0$	$2.0 \le h/r \le 20.0$
C_1	$0.947 + 1.206\sqrt{h/r} - 0.131h/r$	$1.232 + 0.832\sqrt{h/r} - 0.008h/r$
C_2	$0.022 - 3.405\sqrt{h/r} + 0.915h/r$	$-3.813 + 0.968\sqrt{h/r} - 0.260h/r$
C_3	$0.869 + 1.777\sqrt{h/r} - 0.555h/r$	$7.423 - 4.868\sqrt{h/r} + 0.869h/r$
C_4	$-0.810 + 0.422\sqrt{h/r} - 0.260h/r$	$-3.839 + 3.070\sqrt{h/r} - 0.600h/r$

Figure 5.14: Geometrical stress concentration factor for shafts diameter variations

1.
Round shaft with semicircular end key seat

a. Bending

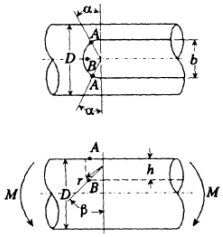

$$\sigma_{\max} = K_t \sigma, \qquad \sigma = 32M/\pi D^3$$

$b = \frac{1}{4}D, \qquad h = \frac{1}{8}D, \qquad \alpha = 10°, \qquad \beta = 15°$

(1) At location A on surface:

$K_{tA} = 1.6$

(2) At location B at end of keyway:

$$K_{tB} = 1.426 + 0.1643\left(\frac{0.1}{r/D}\right) - 0.0019\left(\frac{0.1}{r/D}\right)^2$$

where $0.005 \le r/D \le 0.04$

$D \le 6.5$ in.

$h/D = 0.125$

For $D > 6.5$ in., it is suggested that the K_{tB} values for $r/D = 0.0208$ be used.

Figure 5.15: Geometrical stress concentration factor for key slots

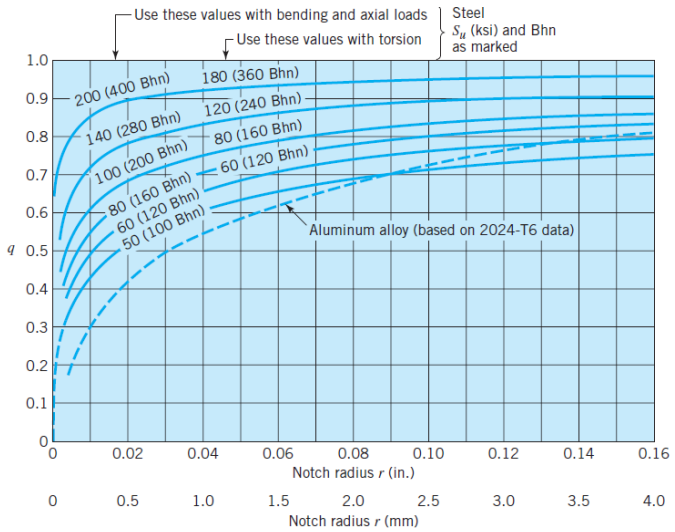

Figure 5.16: Notch sensitivity factor function of the notch radius and material hardness

5.3.3 Fatigue calculation results

Tables-5.6 to 5.8 present the necessary parameters of the fatigue calculation procedure previously presented and Tables 5.9 to 5.14 the results.

In all situations the safety coefficient is quite high ($sc > 2.6$).

Table 5.6: Geometrical parameters necessary to calculate the safety coefficient do to section variation

x	[mm]	29
D	[mm]	35
d	[mm]	25
r	[mm]	5
h	[mm]	5
c_1		2.022
c_2		-2.468
c_3		2.091
c_4		-0.648
k_t		1.472
q		1
k_f		1.472
A	[mm^2]	490.9
I	[mm^4]	1.917e+04
I_p	[mm^4]	3.835e+04

Table 5.7: Geometrical parameters necessary to calculate the safety coefficient do to key slot

x	[mm]	23
D	[mm]	25
r	[mm]	0.2
k_t		3.183
q		1
k_f		3.183
A	[mm^2]	490.9
I	[mm^4]	1.917e+04
I_p	[mm^4]	3.835e+04

Table 5.8: Geometrical parameters necessary to calculate the safety coefficient at supports A and C

x	[mm]	60
D	[mm]	35
A	[mm^2]	962.1
I	[mm^4]	7.366e+04
I_p	[mm^4]	1.473e+05

Table 5.9: First shaft fatigue results to section variation

Cal.		1.1	1.3	1.5	1.6
N	[N]	0	16.78	-184.5	-93.02
M_b	[Nm]	52.23	52.15	53.17	56.24
M_y	[Nm]	-52.2	-52.11	-53.17	-52.69
M_z	[Nm]	-1.911	-2.111	-0.5048	19.67
M_t	[Nm]	-14.06	-14.58	-14.06	-12.45
σ_{est}^{eq}	[MPa]	139.3	139.1	141.4	149.8
τ_{est}^{eq}	[MPa]	-4.582	-4.751	-4.582	-4.059
SC		5.266	5.272	5.187	4.901

Table 5.10: Second shaft fatigue results to section variation

Cal.		1.1	1.3	1.5	1.6
N	[N]	0	-482.1	184.5	212.4
M_b	[Nm]	52.23	44.33	55.52	58.03
M_y	[Nm]	52.2	41.82	55.45	55.93
M_z	[Nm]	1.911	14.71	-2.789	-15.46
M_t	[Nm]	47	47	47	47
σ_{est}^{eq}	[MPa]	139.3	117.2	148.4	155.2
τ_{est}^{eq}	[MPa]	15.32	15.32	15.32	15.32
SC		5.154	6.067	4.851	4.647

Table 5.11: First shaft fatigue results to key slot

Cal.		1.1	1.3	1.5	1.6
N	[N]	0	16.78	-184.5	-93.02
M_b	[Nm]	41.43	41.35	42.37	45.75
M_y	[Nm]	-41.4	-41.31	-42.37	-41.89
M_z	[Nm]	-1.515	-1.702	-0.1095	18.39
M_t	[Nm]	-14.06	-14.58	-14.06	-12.45
σ_{est}^{eq}	[MPa]	238.8	238.3	243.8	263.5
τ_{est}^{eq}	[MPa]	-4.582	-4.751	-4.582	-4.059
SC		3.076	3.081	3.012	2.788

Table 5.12: Second shaft fatigue results to key slot

Cal.		1.1	1.3	1.5	1.6
N	[N]	0	-482.1	184.5	212.4
M_b	[Nm]	41.43	34.51	44.76	47.89
M_y	[Nm]	41.4	31.41	44.65	45.13
M_z	[Nm]	1.515	14.3	-3.185	-16.02
M_t	[Nm]	47	47	47	47
σ_{est}^{eq}	[MPa]	238.8	197.9	258.3	276.5
τ_{est}^{eq}	[MPa]	15.32	15.32	15.32	15.32
SC		3.053	3.669	2.825	2.642

Table 5.13: First shaft fatigue results in support A

Cal.		1.1	1.3	1.5	1.6
N	[N]	0	0	-2.842e-14	4.263e-14
M_b	[Nm]	108.1	108	109	111.6
M_y	[Nm]	-108	-107.9	-109	-108.5
M_z	[Nm]	-3.953	-4.227	-2.547	26.25
M_t	[Nm]	-14.06	-14.58	-14.06	-12.45
σ_{est}^{eq}	[MPa]	71.32	71.27	71.93	73.66
τ_{est}^{eq}	[MPa]	-1.67	-1.732	-1.67	-1.479
SC		10.29	10.3	10.21	9.97

Table 5.14: Second shaft fatigue results in support C

Cal.		1.1	1.3	1.5	1.6
N	[N]	0	-5.684e-14	2.842e-14	0
M_b	[Nm]	108.1	97.05	111.2	112.4
M_y	[Nm]	108	95.58	111.2	111.7
M_z	[Nm]	3.953	16.82	-0.747	-12.58
M_t	[Nm]	47	47	47	47
σ_{est}^{eq}	[MPa]	71.32	64.05	73.41	74.2
τ_{est}^{eq}	[MPa]	5.583	5.583	5.583	5.583
SC		10.18	11.31	9.898	9.795

5.4 Rolling bearings calculation

5.4.1 Rolling bearings calculation procedure

The type of support selected is a housing support with a ball bearing inside, provided by Schaffler. For the calculation of this components, the calculation procedure presented in Schaffler's catalogue was followed [29]. This procedure is divided in two parts the load carrying capacity under static conditions and the rated life under dynamic conditions.

For the load carrying capacity under static conditions the equivalent static rolling bearing load P_0 is directly compared with the basic static load rating C_{0r}, for a given P_0 the selected bearing must have a grater value of C_{0r}. The value of C_{0r} of the selected bearing size, as well as other characteristics can be found in Table 5.15.

Table 5.15: RASEA35-XL-N Proprieties for life calculation

		RASEA35-XL-N
C	[N]	26500
C_{0r}	[N]	15700
f_0		13.8

The value of P_0 is given by

$$P_0 = X_0 F_{0r} + Y_0 F_{0a} \tag{5.43}$$

where X_0 is the radial factor, Y_0 is the axial factor, F_{0r} is the radial static bearing load and F_{0a} is the axial static bearing load. The values X_0 and Y_0 are equal to 1 and 0 respectively if $F_{0a}/F_{0r} \leq 0,8$ and equal to 0.6 and 0.5 respectively if $F_{0a}/F_{0r} > 0,8$.

For the calculation of the rated life under dynamic conditions the basic dynamic load C is compared with the equivalent dynamic bearing load P using

$$L_{10h} = \frac{16666}{n} \left(\frac{C}{P}\right)^p \tag{5.44}$$

where L_{10h} is the rated life in hours and n is the operating speed in revolutions per minute. The value of P is given by

$$P = XF_r + YF_a \tag{5.45}$$

where X is the radial load factor, Y is the axial factor, F_r is the radial dynamic bearing load and F_a is the axial dynamic bearing load. The values X and Y are equal to 1 and 0 respectively if $F_a/F_r \leq e$ and for $F_a/F_r > e$ the values of X and Y are given in Table 5.16, where is also shown the values for e.

Table 5.16: X and Y factors has function of rolling bearing and axial load

$\frac{f_0 F_a}{C_{0r}}$	e	X	Y
0.3	0.22	0.56	2
0.5	0.24	0.56	1.5
0.9	0.28	0.56	1.85
1.6	0.35	0.56	1.4
3	0.36	0.56	1.2
6	0.43	0.56	1

5.4.2 Rolling bearings calculation results

Regarding the static bearing calculations, Tables 5.17 and 5.18 show the values of P_0. These values are considerable smaller (over six times smaller) them C_{0r}.

Table 5.17: Static results for bearing A

Cal.		2.1	2.4	2.5	2.6
F_a	[N]	0	-7.154	184.5	1.13e-14
F_r	[N]	2545	2545	2552	2569
X_0		1	1	1	1
Y_0		0	0	0	0
P_0	[N]	2545	2545	2552	2569

Table 5.18: Static results for bearing C

Cal.		2.1	2.4	2.5	2.6
F_a	[N]	0	484.1	-184.5	-184.5
F_r	[N]	2545	2395	2567	2569
X_0		1	1	1	1
Y_0		0	0	0	0
P_0	[N]	2545	2395	2567	2569

Regarding the dynamic rolling bearing calculation, Tables 5.19 and 5.20 present the rated life of the rolling bearings when submitted to the reaction loads corresponding to part three.

Table 5.19: Dynamic results for bearing A

Cal.		3.1	3.3	3.6	3.7
n	[rpm]	3000	3000	3000	3000
F_a	[N]	0	0	36.66	180
F_r	[N]	2545	2545	2619	2545
e		0.1777	0.1777	0.1826	0.2006
X		1	1	1	1
Y		0	0	0	0
P	[N]	2545	2545	2619	2545
L_{10_h}	[h]	6273	6273	5757	6273

Table 5.20: Dynamic results for bearing C

Cal.		3.1	3.3	3.6	3.7
n	[rpm]	3000	3000	3000	3000
F_a	[N]	0	465.9	-216.7	292
F_r	[N]	2545	2458	2559	2524
e		0.1777	0.2318	0.1466	0.2135
X		1	1	1	1
Y		0	0	0	0
P	[N]	2545	2458	2559	2524
L_{10_h}	[h]	6273	6959	6167	6429

Chapter 6

Base structure

This chapter presents the constructive solution for the base structure. It starts with the establishment of some requirements that the base structure should fulfil. The main structural parts are described as well as the connection elements.

6.1 Guide lines

In order to support all the components of the test rig, a supporting structure is needed. The structure of the test rig was designed according the following guide lines and requirements:

- Easy manufacturing/acquisition,
- minimizing the number of parts needing machining processes,
- Modular structure,
- Versatile connection elements.

An entity capable of offering a solution that meets these requirements is the Rexroth Bosch Group with structural profiles [35]. The wide variety of Bosch Rexroth profiles covers virtually any application (see Figure 6.1). They are constructed with a continuous cross section with groove on the sides in order to increase robustness and to facilitate assembly. The several profiles possess grove width of 6 mm, 8 mm and 10 mm. The 10 mm grove allows maximum strength connections, due to this the corresponding profiles are suitable for applications with high loads and therefore should be the selected for the test rig.

Figure 6.1: Different Bosch profiles with different groove dimensions

6.2 Selected profiles

The profile dimensions available for 10 mm width groves are the 40 mm, 45 mm, 50 mm and 60 mm. The selected profile dimension for the test rig is the 45 mm since this provide a variety of different cross sections that allow for design versatility.

The material of these Bosch structural profiles is AlMgSi 0.5 F25, which correspondent to a 6000 series aluminium alloy, the 6063 T6. This material is very easy to machine and to weld. The main properties of this material can be found in Table 6.1. The profiles used are shown in Figure 6.2 and their technical information is present in Table 6.2

Table 6.1: Mechanical proprieties of Bosch structural profile material

Young's Modulus	E	Pa	70×10^9
Poisson's ratio	ν		0.34
Ultimate strength	σ_u	Pa	250×10^6
Yield strength	σ_y	Pa	200×10^6

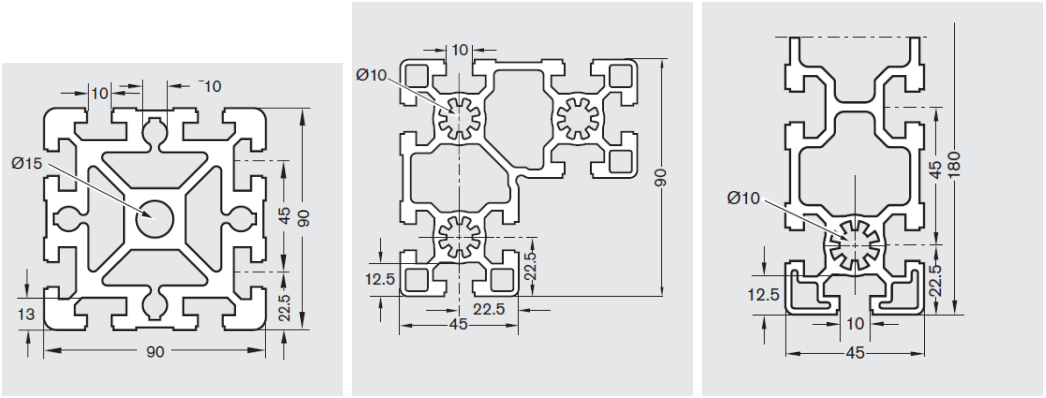

(a) 90x90H (b) 45x90x90 (c) 45x180H

Figure 6.2: Bosch profiles used in the test rig

Table 6.2: Geometrical proprieties of the Bosch profiles

	A cm^2	I_y cm^4	I_z cm^4	Weight kg/m
90x90H	39.43	299.80	299.80	11.60
45x90x90	21.00	151.13	151.13	5.67
45x180H	25.50	766.67	57.28	6.90

Figure 6.3 shows the assembly of the base structure. On top of the 45x90x90 profiles (in green) will be mounted the plate associated to the center distance, while on the side of the 45x180H profiles (in red) will be mounted the linear plate associated to the axial offset. The two central bottom 90x90 profiles (in grey), although they are not loaded, are used to provide stiffness to the structure by closing a rectangle with the vertical profiles and the 45x90x90 profiles. The 90x90 profiles that extend further outside in the bottom part of the structure are used to counteract the weight of overhanging components such as the motors. Table 6.3 lists the different profile parts and their lengths.

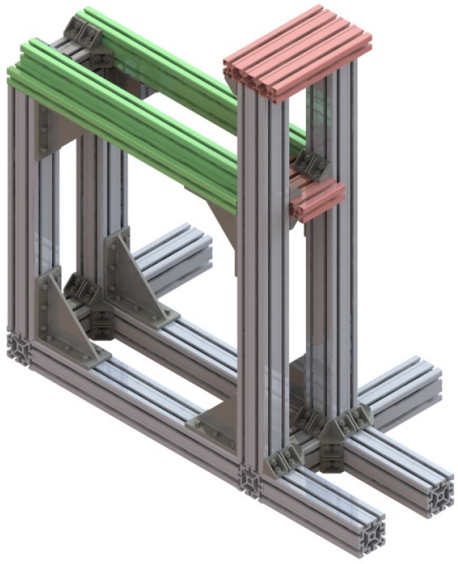

Figure 6.3: Assembly of the base structure, 90x90H gray, 45x90x90 green and 45x180H red

Table 6.3: Lengths and weights of the different profiles used in the base structure

Profile	Quantity	Length [mm]	Weight [kg]
45x90x90	2	770	2 x 4.37
45x180 H	1	320	2.21
45x180 H	1	140	0.97
90x90 H	2	1080	2 x 12.53
90x90 H	2	700	2 x 8.12
90x90 H	2	680	2 x 7.89
90x90 H	2	600	2 x 6.96
90x90 H	2	320	2 x 3.71
90x90 H	1	140	1.62
Total			91.95

6.3 Connections

To connect the several profiles used in the test rig structure two different connectors are used, simple brackets and heavy duty connectors. Figure 6.4 shows the brackets while Figure 6.5 shows the heavy duty connectors. The brackets are versatile and only occupy one slot of each profile. On the other hand, the heavy duty profiles occupy two parallel slots on the profiles.

The brackets are mounted with T-shaped bolts whose heads are designed to fit in the groves of the profiles. On the other hand, the heavy duty connectors mount with sliding blocks and screws. The sliding blocks are design to fit in the profile groves and have the threaded holes to connect with the screws. This provides a much strong connection, with a greater overall stiffness.

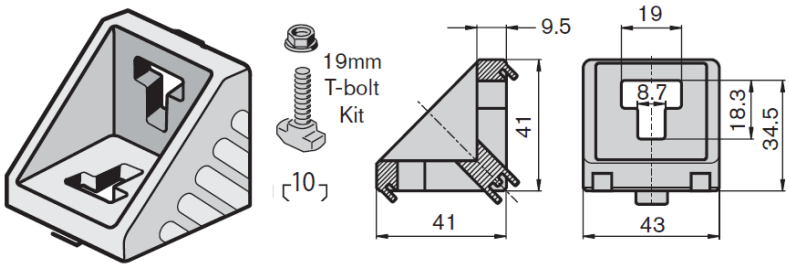

Figure 6.4: Bracket for 45 mm profiles

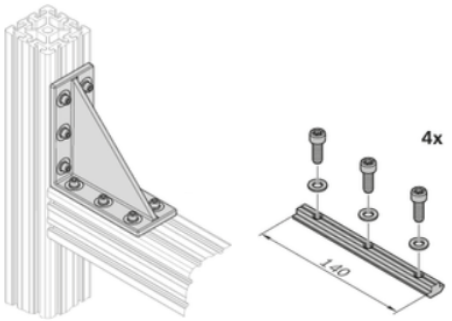

(a) Heavy duty connector (b) Sliding blocks

Figure 6.5: Heavy duty connectors for 90x90 profiles

Chapter 7

Misalignments implementation

This chapter discusses the details associated with the misalignments implementation. It starts with a brief overview of previous information followed by the presentation of the linear degrees of freedom and angular degrees of freedom. It concludes with the presentation of the positioning solution for the several degrees of freedom. The technical drawings of the parts that were designed, and not selected from components suppliers, can be found in Appendix D. The drawings were made according to the book Simões Morais Desenho Técnico 3 [36]. The technical information in the drawings assumes that the parts are manufactured by machining with medium quality. Most of the operations are done with conventional milling machine or a lathe.

7.1 Overview of the degrees of freedom

As mentioned previously, in this work there are four degrees of freedom, two linear displacements and two angular displacements. The linear displacements are the center distance and the axial offset, while the angular displacements are the toe and camber. During the design, to allow for the greatest simplicity, the displacements were separated, being the center distance and toe implemented in the input shaft and pulley while the axial offset and camber were implemented in the output shaft and pulley. Each linear displacement is associated to one movable base plate. These plates are used to support other components and to implement the displacements. Figure 7.1 shows the configuration of these plates relative to each other and the corresponding displacements. The plates associated with the linear displacements will be called linear plates, while the plates associated with the angular displacements will be called angular plates. The plates, was well as the rest of the design parts, must be obtained from versatile manufacturing processes, such as machining. The extreme values of the range of each displacement are presented in Table 7.1.

Table 7.1: Working window of each misalignment

			min	max
Center distance	a	[mm]	500	800
Axial offset	b	[mm]	0	50
Toe	θ_t	[º]	0	15
Camber	θ_c	[º]	-90	0

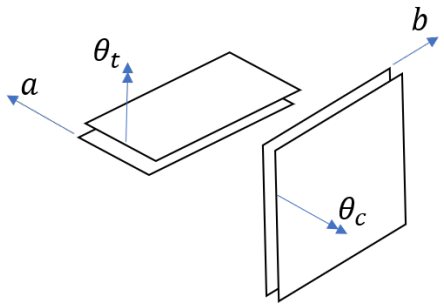

Figure 7.1: Relative position of each of the plates associated to the several degrees of freedom

7.2 Linear degrees of freedom

The linear displacements were implemented directly on the base structure using a Bosh Rexorth's solution called EcoSlide, presented in Figure 7.2 and Table 7.2 [35]. This solution is particularly interesting for the following reasons:

- Easy acquisition,
- Almost no parts obtained by machining processes,
- Modular structure,
- Versatile connection elements,
- Can be implemented directly on to the base structure.

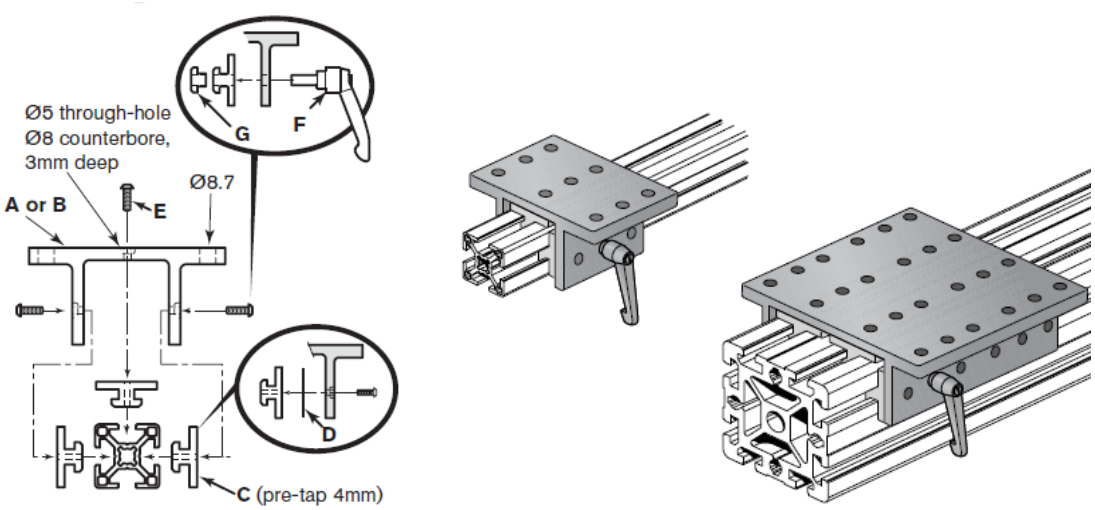

(a) EcoSlide assembly (b) Overview

Figure 7.2: Bosh Rexorth's EcoSlide solution for linear displacements

Figures 7.3a and 7.3b show the sketch of the linear plates and Figure 7.4 shows how they connect with the base structure. The EcoSlide carriages are connected to the linear plates with bolts. To ensure positioning precision a rectangular cavity per carriage must be machined on the bottom of the plates with an end mill. The machining of these cavities

Table 7.2: Parts discription of Bosh Rexorth's EcoSlide solution for linear displacements

Part	Discription
A and B	EcoSlide carriage
C	EcoSlide bearing, flat
D	Bearing shim, 0.1mm thick
E	M4x12 ISO 7380 BHC screw
F	Locking lever
G	M8 T-block

leaves a fillet in the corners. The EcoSlide carriages are provided with 90 degree corners on the top surface, so to ensure proper assembly the corners must be chamfered off.

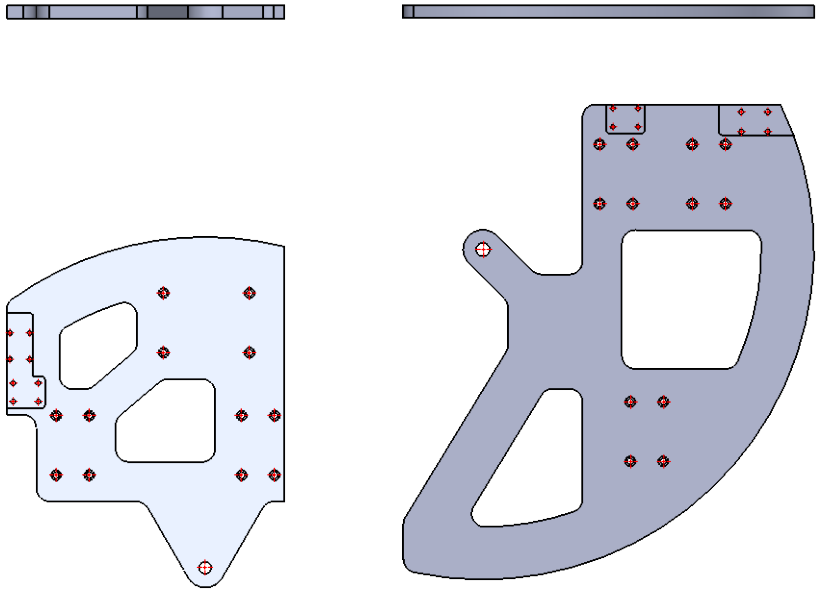

(a) Center distance movable plate (b) Axial offset movable plate

Figure 7.3: Linear plates

The EcoSlide bearings are design to travel inside the grooves of the Bosch profiles. To ensure a close enough fit and a proper guiding they are mounted with 0.1 mm thick shims between the EcoSlide bearing and the EcoSlide carriage. The number of shims per bearing may vary and its only defined when assembling. The bearings are conected to the carriage through the M4x12 ISO 7380 BHC screws.

In this work it was not possible to use the locking leaver due to space limitations. Instead a minimum of a screw per carriage, each alongside a T-block nut, were used to lock the carriages to the structure profiles when in the pretended positions.

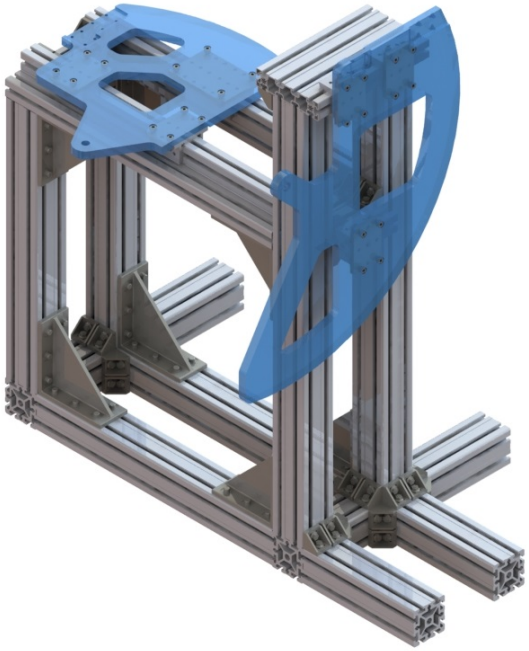

Figure 7.4: Assembly of the linear plates on the base structure

7.3 Angular degrees of freedom

The angular displacements were implemented directly on the linear plates. Contrarily to the linear displacements the angular displacements were not implemented following a pre-existing solution, and they were specially designed for this application, in order to ensure design precision and to simplify the overall solution.

The toe degree of freedom is coupled to the center distance and the camber degree of freedom coupled to the axial offset. The implementation of toe over the center distance does not differ from the camber over the axial offset. In fact, regarding the mechanical design, almost all parts used in one angular degree of freedom are equal to the other, inclusive the angular plates. Figure 7.5 shows the angular plate.

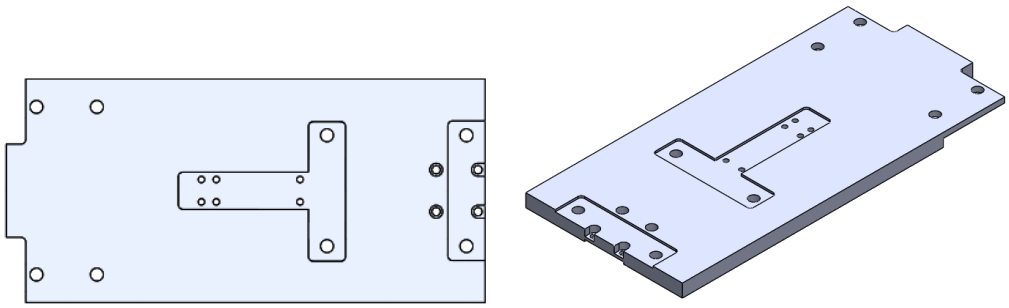

(a) Top view (b) 3D

Figure 7.5: Angular plate

The angular displacements are implemented using pivot points. The pivot point corresponds of the center of rotation between the relative movement of the linear plate and the angular plate.

To ensure that the degrees of freedom correspond to the independent misalignments,

the pivot points must be located below the pulley, such that from the top view the center of the pulleys and pivot point are coincident (Figure 7.6).

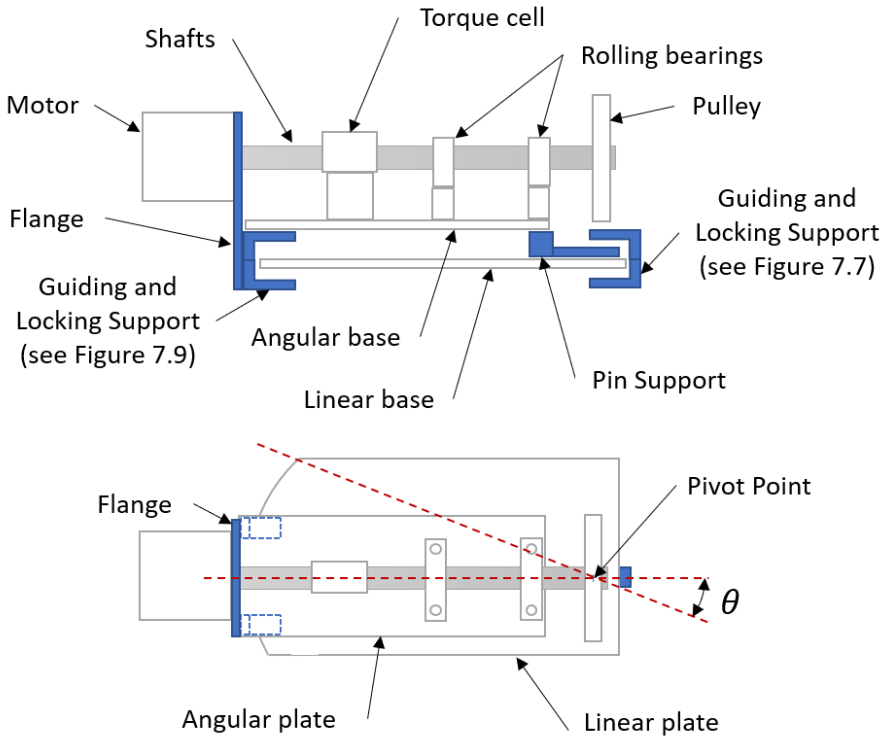

Figure 7.6: Schematic of the angular displacement design (front and top views)

To restrict other movements besides the rotation, C shaped parts were design to perform two tasks: 1) to guide the movement when positioning 2) to lock the plates one to the other when in the desired position. The overall design contemplates three of these parts for each angular degree of freedom, one in the front and two in the back. These three locking parts define a three point support between the angular plate and the linear one, thus ensuring a stable support configuration. As shown in Figure 7.6 the two C shaped locking supports from the back are also responsible for supporting the flange that supports the motor.

Each pivot point is physically associated with a pin that sets the point of rotation of the angular plate relative to the corresponding angular plate. Each pin is half housed in the hole in the linear plate and half housed in the pin support. Figure 7.7 shows the detail housing of the pin and Table 7.3 lists the several components.

Between the pin and each of its hounding parts a radial plain baring was used (Figure-7.8a). This plain bearings are provided by Schaeffler and contain in its inner diameter a composite material such as PTFE to lower the coefficient of friction between the pin and the support. [37]. Axial plain bearings are also used (see Figure7.8c). Similarly to the radial plain bearings, these contain PTFE in on one of the sides to minimize friction between the angular plates and the C shape supports.

Similarly to the pivot point, plain bearings are used to guide the movement in the two C shaped supports in the back of the angular plate. Figure 7.9 shows the detail assembly of the back supports and Table 7.3 lists all the components.

To lock the angular plate to the linear one, a static contact solution was designed. This solution consists of three parts, the C shaped support, a headless screw tip and a

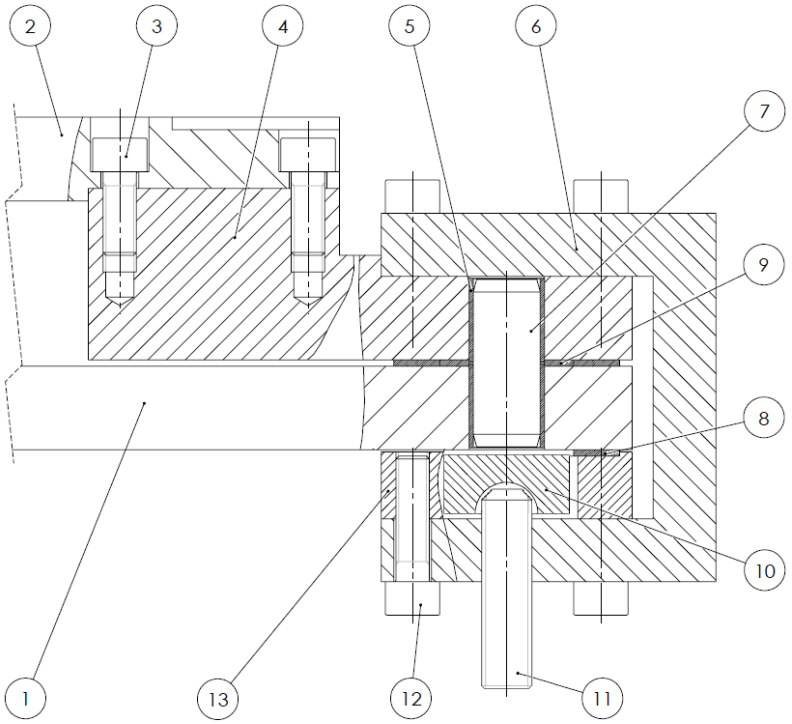

Figure 7.7: Design of pivot point mechanism for the angular displacements

(a) Radial (b) Radial with axial support (c) Axial

Figure 7.8: Schaeffler plain bearings [37]

contacting part (parts 6, 10 and 11 from Figure 7.7). The contacting part is no more than a cylinder with a with a spherical concave feature in one of the faces. The C shaped support has a through all threaded bore at the bottom side of the C. By rotating the screw tip, the contact element moves closer to the linear plate until it touches it. After this the contact part starts to compress the linear plate against the angular, therefore locking them. This solution can be seen in Figures 7.7 and 7.9.

The assembly drawings of the components presented in this work are displayed in Appendix D

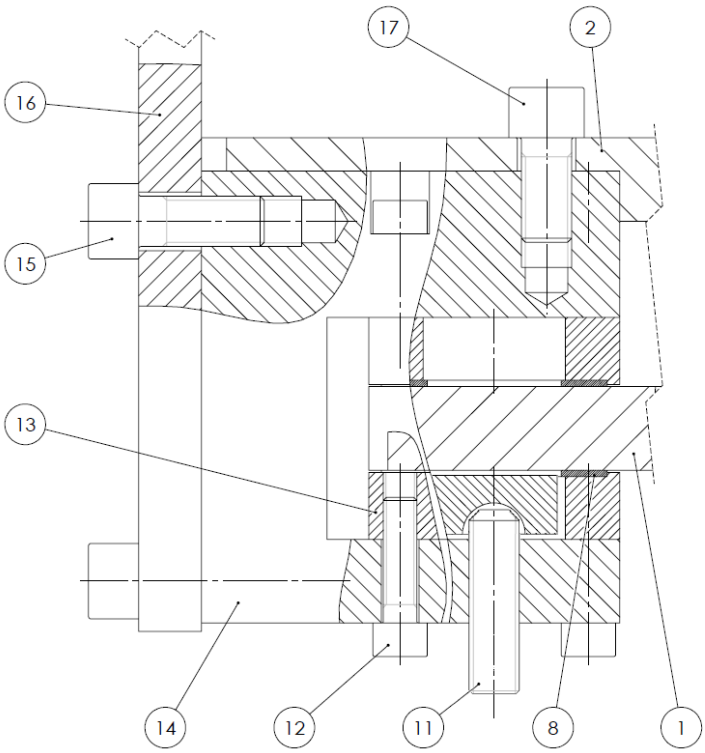

Figure 7.9: Design of the C shaped support

Table 7.3: List of components present in Figures 7.7 and 7.9

Number	Componet	Tec. Info
1	Linear plate	
2	Angular plate	
3	CHC	ISO 4762 M8x20
4	Pin support	
5	Radial plain bearing	PCM 161820
6	Front C shaped support	
7	Pin	ISO 8734 - 16x40
8	Axial plain bearing	PCMW 183201.5
9	Axial plain bearing	PCMW 325401.5
10	Locker	
11	Headless screw tip	ISO 4026 M12x40
12	CHC	ISO 4762 M8x30
13	Plain bearing support	
14	Back C shaped support	
15	CHC	ISO 4762 M12x30
16	Motor support flange	
17	CHC	ISO 4762 M12x25

7.4 Positioning

The positioning of the linear plates in relation to the structure profiles, and the angular plates in relation to the linear ones, lead screws were used. In total four lead screws are used, one for each plate. Lead screws were preferred to ball screws because they can provide irreversibility of movement. With this the rotation of the lead screw displaces the nut, but trying to displace the nut does not rotate the lead screw. To achieve this irreversibility the helix angle of the tread must be the lowest possible, therefore the number of independent threads must be one.

In this work the lead screws and the lead screws' nuts are supplied by Automotion Components [38]. The selected ouside diameter for the lead screws is 20 mm with a picth of 4 mm and an helix angle of 4°05'. Automotion Components provides the lead screws in two different materials, C45 carbon steel and AISI 316L stainless steel. The C45 tensile strength is considerably higher then of the 316L, therefore C45 was seleced [39][40]. The only advantage of the stainless is the protection against corrosion. To ensure that the selected C45 lead screws are not prom to corrosion, a surface treatment must be applied. It was chosen a surface nitriding heat treatment, the same way as for the shafts present in this work. On the other hand the lead screw nuts' material is bronze, more precisely the CuSn12 alloy.

The two lead screws associated to the linear plates are attached to the base structure with mouing blocks, while the corresponding nuts are attached to the plates. Figure 7.10 shows the assembly of these in the base structure. The center distance lead screw is

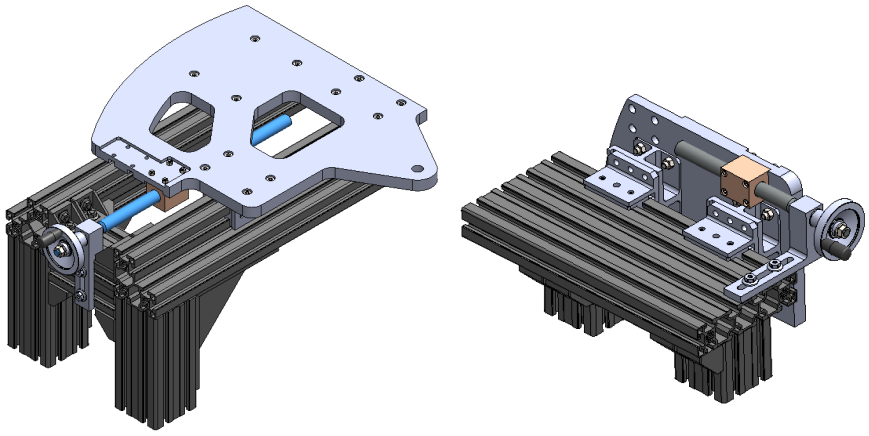

(a) Assembly of the center distance lead screw

(b) Assembly of the axial offset lead screw

Figure 7.10: Linear lead screws representation with addendum diameter

responsible for defining the working center distance and to impose the belt pre-tension. The positioning of the center distance lead screw in relation to the pulleys is such that, when imposing the pre-tension, it works under tension rather then under compression and therefore avoiding buckling problems.

Figure 7.11 shows the detail assembly of the linear lead screws and Table 7.4 lists all the components. The assembly of both linear lead screws is almost equal, being different only in the length of the lead screws and in its supporting part.

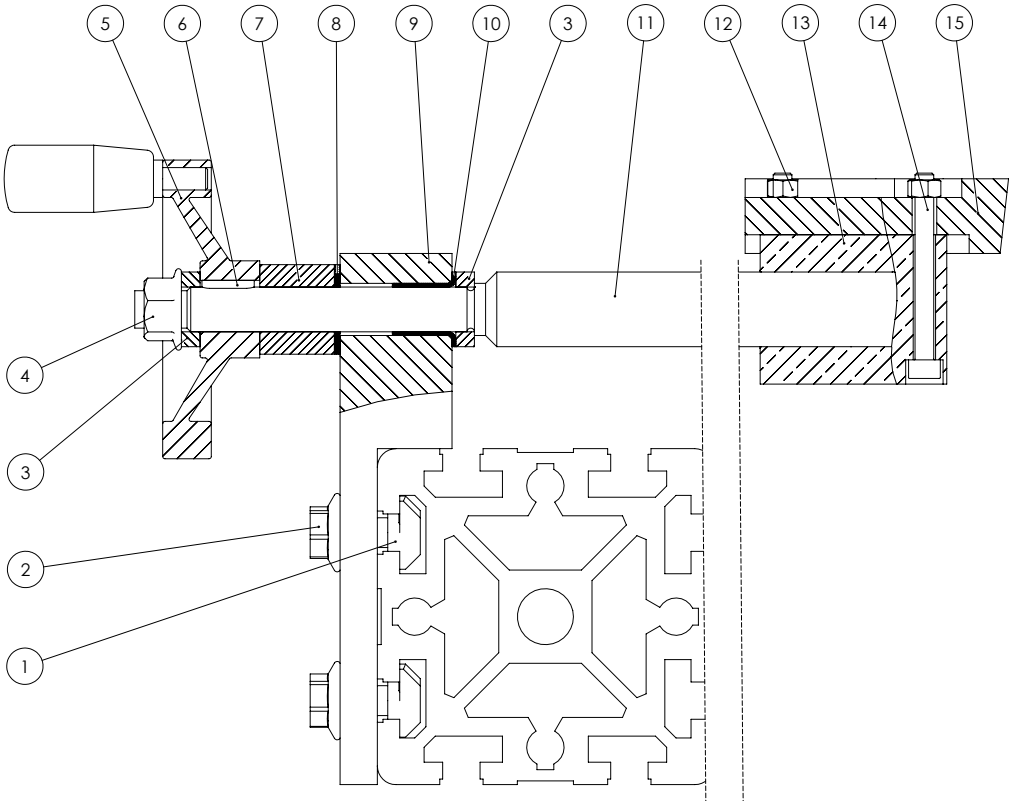

Figure 7.11: Angular lead screws representation with addendum diameter

Table 7.4: List of components present in Figure 7.11

Number	Component	Tec. Info
1	Bosch T nut N10	
2	Bosch flange scrwe	
3	Bushing	d12x5x4
4	Nut	ISO 4161 M10
5	Hand well	
6	Parallel key A	DIN6885 4x4x14
7	Bushing	d12x20x5
8	Axial plain bearing	PCMW122401.5
9	Linear lead screw support	
10	Radial plain bearing with axial support	PCMF 121417
11	Linear lead screw	
12	Nut	ISO 4032 M5
13	Lead screw nut	
14	CHC	ISO 4762 M15x50
15	Linear base	

The maximum axial force that can occur in the lead screws is 1800 N in the center distance lead screw. The minimal cross section diameter in the designs lead screws is 10 mm. This corresponded to a maximum uniformly distributed stress of 23 MPa. This is not a critical value when compared with the C45 tensile strength.

Each of the lead screws is supported by plain bearings, one radially with axial support and one axially, that together with a supporting part discharge the efforts on the base structure. To rotate the leads screws hand-wheels are used. These are also provided by Automotion Components and assemble with the lead screws with keys. The whole assembly is mouthed with bushing between the main components and with a nut with flange that threads at the top of the lead screw in a custom made M10 tread.

Regarding the angular lead screw the design is similar to the linear one, the main difference being that the support of the lead screw and the nut must rotate in relation to the linear angular base. Figure 7.12 shows schematically the main part involving the angular positioning mechanism.

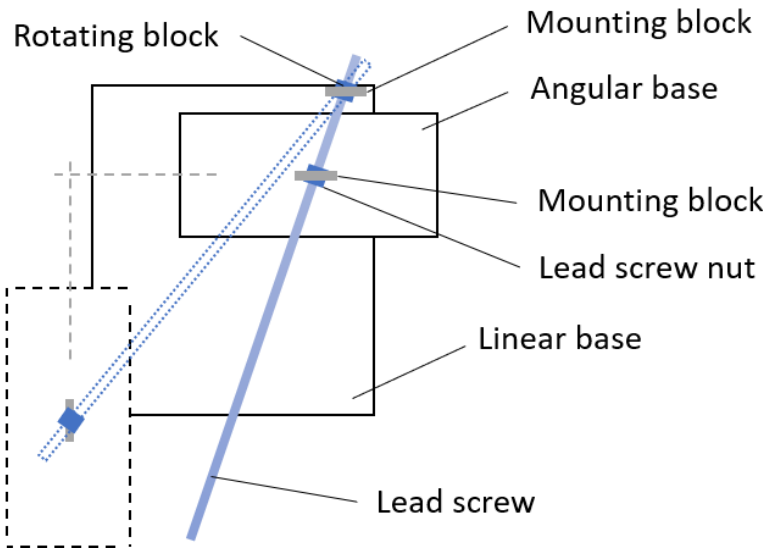

Figure 7.12: Design of the linear lead screws' supports

The angular lead screw is mounted in a rotating block that is then supported in a mounting block fixed to the linear plates. Similarly, the angular lead screws' nuts are also mounted in a mounting block that is static in relation to the angular plates. To allow the rotation of the nuts and rotating blocks in relation to the mounting blocks, two headless screws with recessed cylindrical tip, are used in each mounting block. The cylindrical tip of these mount on holes drilled on the nuts and the rotating block. One mounted on the top and the other mounted on the bottom. To allow an easy relative movement of the parts, Schaeffler plain bearing are used to separate them. Figure 7.13 shows the detailed assembly of these parts and Table 7.5 lists all the components.

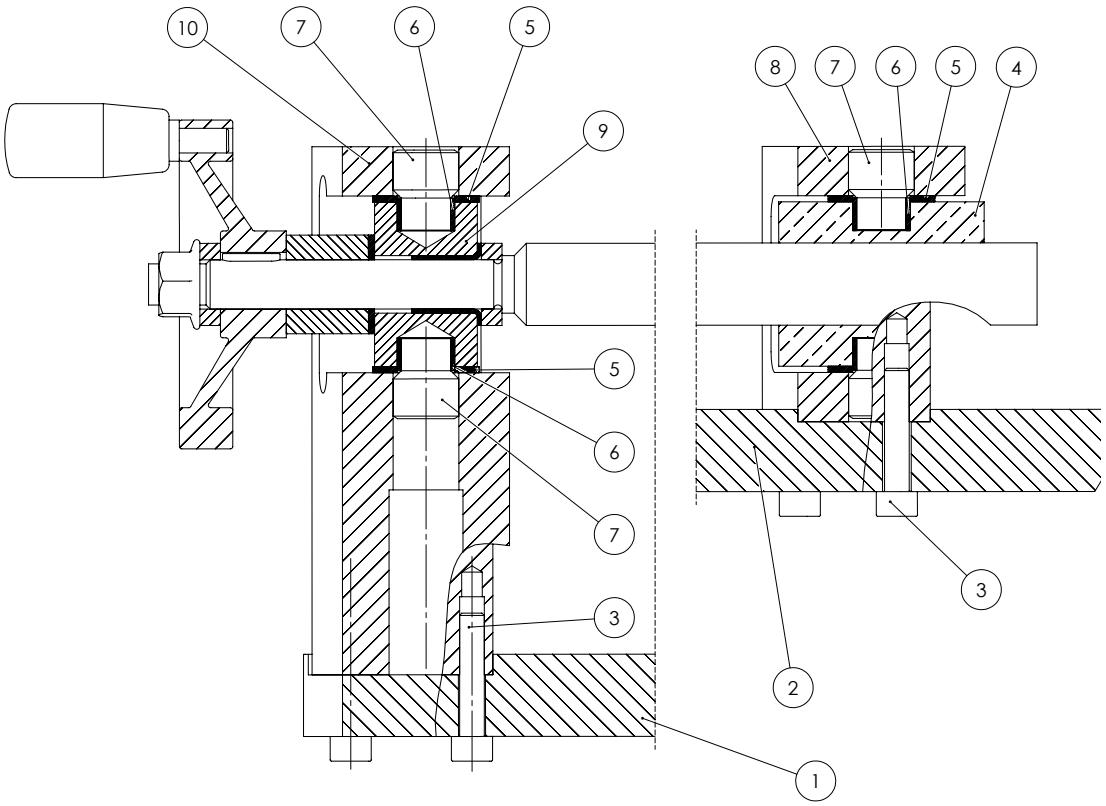

Figure 7.13: Design of the angular lead screws supports

Table 7.5: List of components present in Figure 7.13

Number	Componet	Tec. Info
1	Linear plate	
2	Angular plate	
3	CHC	ISO 4762 M6x50
4	Lead screw nut	
5	Axial plain bearing	PCMW 142601.5
6	Radial plain bearing	PCM 121408
7	Headles screw tip	ISO 4028 M6X20 LD
8	Nut mounting block	
9	Rotating block	
10	Lead screw mounting block	

Table 7.6 presents the threaded and total lengths of the lead screws.

Table 7.6: Threaded and total lengths of the lead screws

	Threaded [mm]	Total [mm]
Toe	293	390
Camber	653	750
Center distance	393	490
Axial offset	143	240

Using lead screws to position the angular plates creates a non linear relationship between the angular displacements and the position of the nuts in the angular lead screws. Figure 7.14 shows the variables needed to establish this relationship.

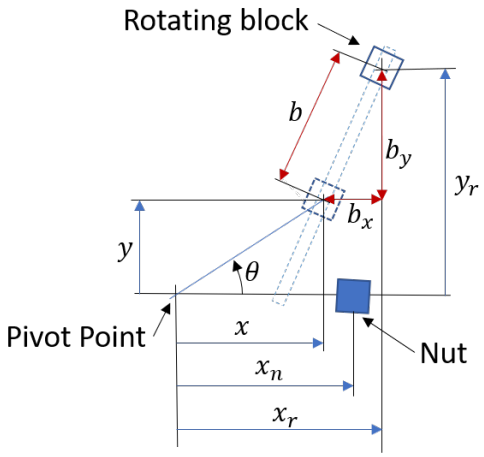

Figure 7.14: Schematic of the parameter needed to establish $b(\theta)$

For a given θ (angular displacement) the positioning of the nut in relation to the pivot point can be given by

$$x(\theta) = x_n \cos(\theta) \tag{7.1}$$

$$y(\theta) = x_n \sin(\theta) \tag{7.2}$$

with this the cartesian projections of the distance between the nut and the rotating block can be given by

$$b_x = x_r - x_n \cos\theta \tag{7.3}$$

$$b_y = y_r - x_n \sin\theta \tag{7.4}$$

the distance between the nut and the rotating block can be given by

$$b = \sqrt{(x_r - x_n \cos\theta)^2 + (y_r - x_n \sin\theta)^2} \tag{7.5}$$

this distance can also be given by

$$b = b_0 - np \tag{7.6}$$

where b_0 is b evaluated at θ equal to zero, n is the number of turns performed in the lead screw and p is the pitch of the lead screw, equal to 4 mm. Combining these last two equation and solving for n results in the following

$$n = \frac{b_0 - \sqrt{(x_r - x_n \cos\theta)^2 + (y_r - x_n \sin\theta)^2}}{p} \tag{7.7}$$

The values of x_n, x_r, y_r and b_0 can be found in the Table 7.7

Table 7.7: Values of the parameter needed to establish $b(\theta)$

		toe	camber
x_n	mm	284	284
x_r	mm	335	410
y_r	mm	280	193
b_0	mm	284.6	230.5

Chapter 8

Conclusion and future work

8.1 Summary

The aim of this work was to make the mechanical project for a belt transmission test rig.

One of the requirements stated that the test rig must be able to impose misalignments between the pulleys. In total there are three misalignments: axial offset, toe and camber. Optibelt's technical manual provide limiting values for the first two. Regarding toe it recommends to not exceed 0.5°. On the other hand regarding axial offset it recommends to not exceed 1 mm for pulleys up to 224 mm. The designed test rig allows to impose a toe up to 15° and an axial offset up to 50mm.

Another requirements stated that the test rig must de able to impose belt's pre-tension and to use pulleys with up three belts. Optiblet's software recommends about 360 N of pre-tension per belt. The designed test rig allows for a pre-tension per belt of 600 N and a total pre-tension of 1800 N.

The designed test rig can variate the following parameters:

- Pulleys diameters, from 67 mm to 224 mm.
- Transmission ratio, from 1 to 2.4 at 5,5 kW and up to 3.3 at the maximum torque allowed by the motors.
- Number of belts, up to three belts.
- Center distance, from 500 mm up to 800 mm.
- Belt length
- Toe misalignment, up to 15 degrees.
- Camber misalignment, up to 90 degrees.
- Axial offset misalignment, up to 50 mm.
- Belts pretension, up to 1800 N.
- Input torque, up to 30 Nm.
- Input speed, up to 3000 rpm.

Figures 8.1 to 8.3 show the test rig in three different configurations.

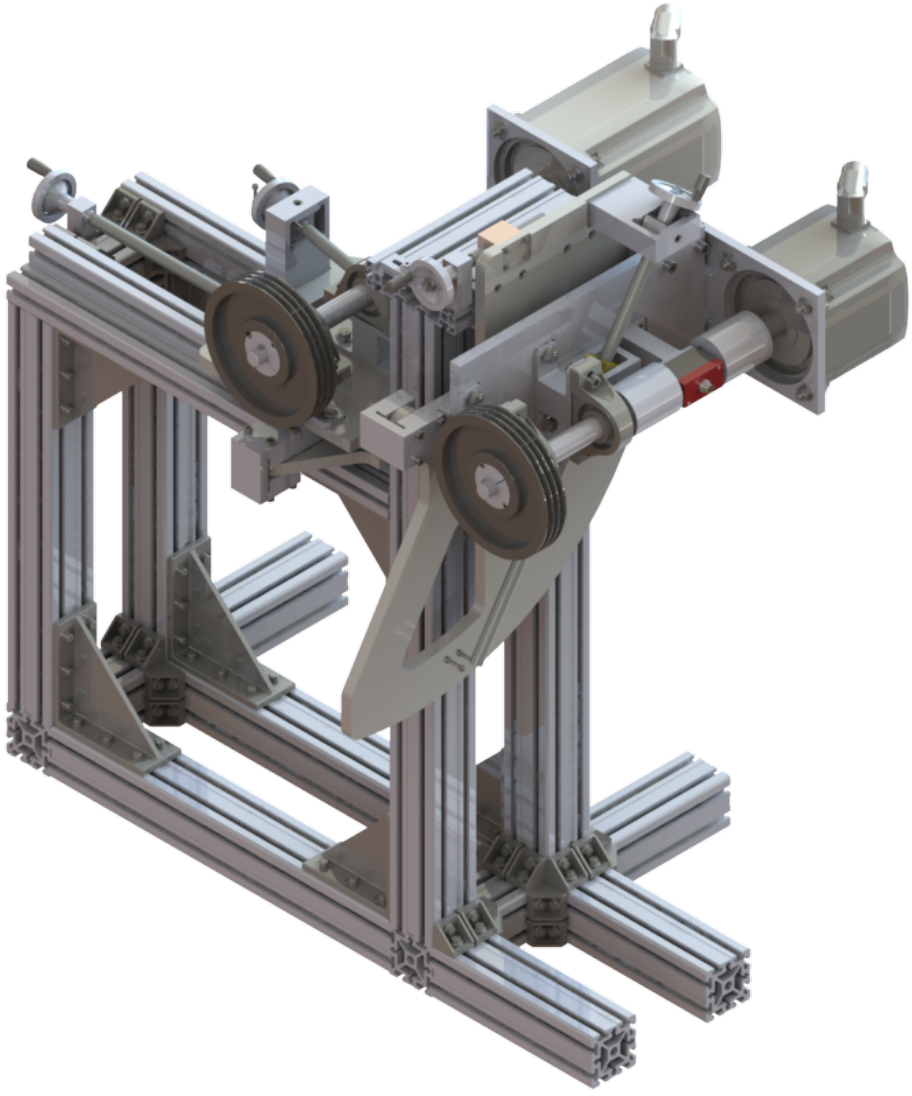

Figure 8.1: Reference position: minimum center distance and no misalignments

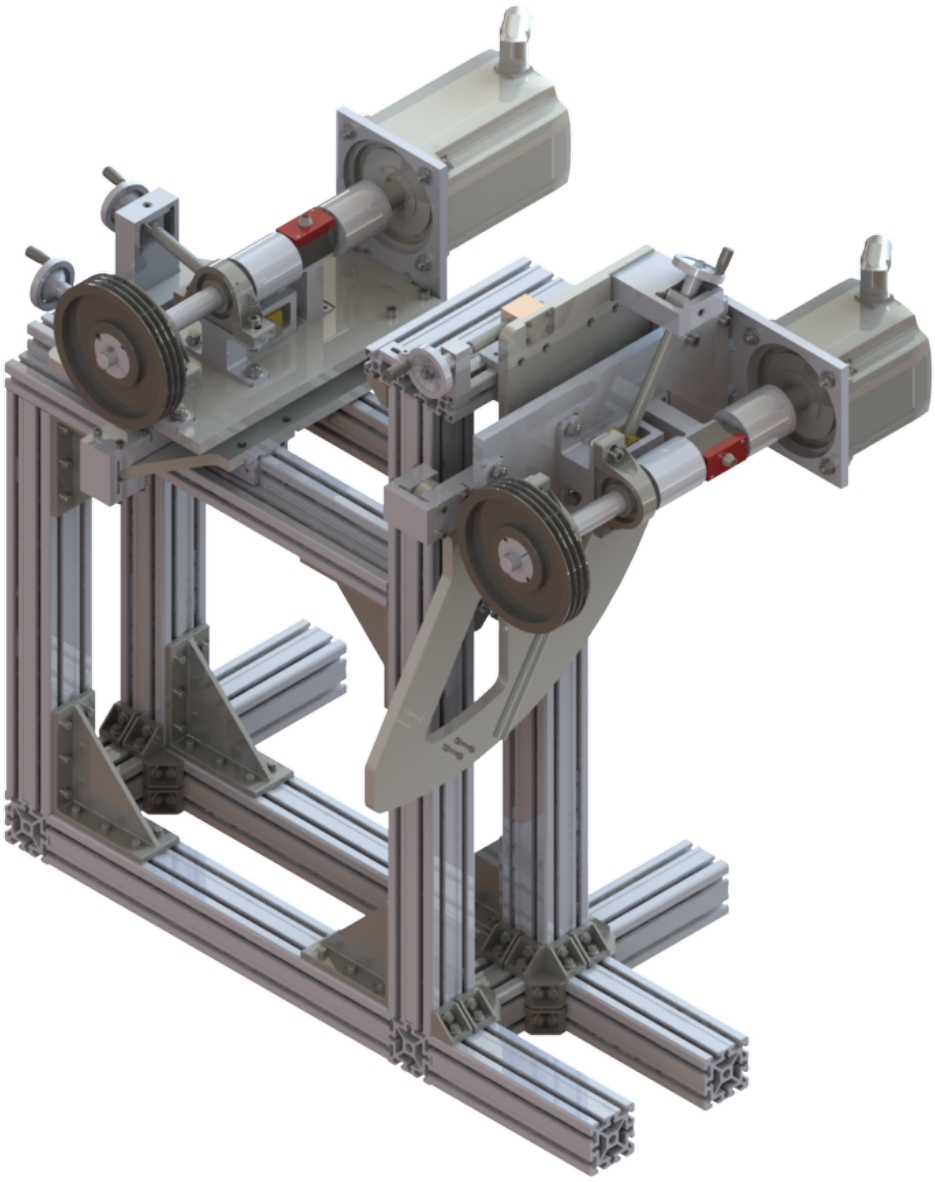

Figure 8.2: Max position of linear degrees of freedom

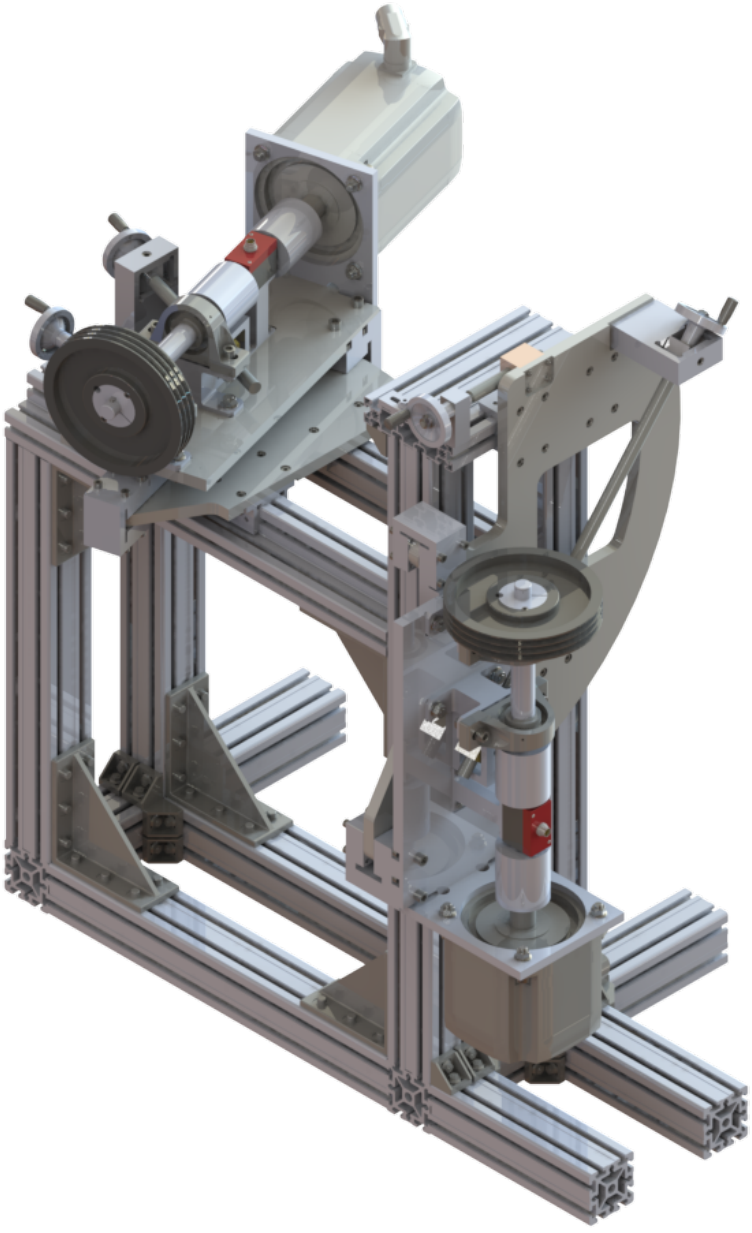

Figure 8.3: Max position of all degrees of freedom

8.2 Conclusions

After the review of the state of the art, it was noticed that a traditional design of a back to back transmission test bench, as the FZG test, could not be used due to slippage between the belts and the pulleys. This implies that instead of a closed mechanical power circuit, a open mechanical power circuit must be used.

For powering the test bench, it was noted that instead of using a break test bench solution, where all the transmitted power would be consumed by a brake dynamometer, an existing electric regenerative test bench solution, where energy could be recirculated is more interesting and therefore selected. This closes the power circuit, being half of it mechanical and the other half electrical, with the connection between the tow halves connected with two motors that can also work as generators.

To provide measurements of torque and speed in each of the shafts, two torque load cells are used. To compute the power loss in the belt transmission the torque losses present in the bearings supports had to be estimated. To this an empiric numerical model, made available by SKF, was used.

The test bench was designed to simulate the effects of improper working conditions, namely the misalignments and belts pre-tension. In total there are three misalignments which were implemented through three degrees of freedom. Also a fourth one, that corresponds to the center distance of the pulleys, is needed to impose belt pre-tension. In total there are two linear degrees of freedom and two angular ones. The linear ones were implemented directly on the base structure and the angular ones were each implemented on top of a linear one. The linear degrees of freedom were implemented using an existing solution suitable for the selected design solution of the base structure, while the angular ones were designed from scratch using a pin pivot point for each. To define the center distance and each of the misalignments four lead screws were used.

8.3 Future work

After completing the pretended work it was noticed that the constructive solution that supports the motors appears not have much rigidity. So as a future work a better solution must be implemented. Figure presents a possible solution where the motors' flanges are supported by two additional parts that are bolted to the angular plate.

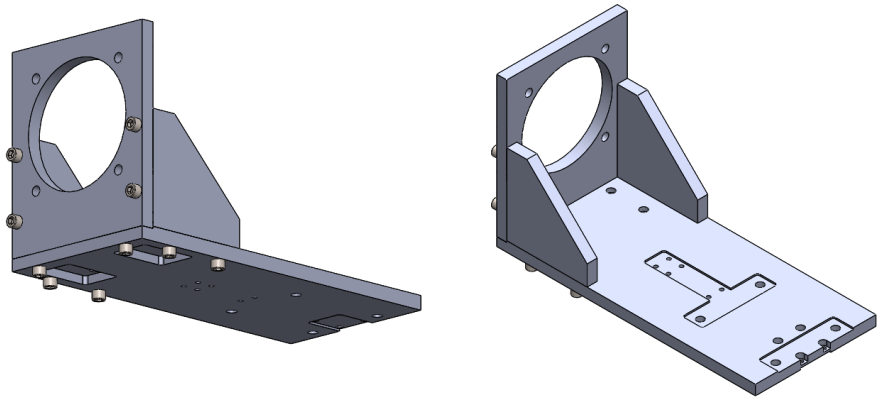

(a) Back view (b) Top view

Figure 8.4: Alternative solution for supporting the motors flange

As future work it is necessary to design an protection cage to enclosure hazards from people.

To provide the electric power, protection and cutting functions an electric box should also be design. The incorporation of these elements may imply alterations on the base structure, if so the base structure may be redesign.

To conclude, in order to assess the measured information and making command function, a PLC type solution as well as a Lab View interface for example must be implemented.

References

[1] Robert C Juvinall and Kurt M Marshek. *Fundamentals of machine component design*. Vol. 1. Wiley New York, 2000.

[2] Encyclopedia Britannica. *Belt drive mechanics*. URL: https://www.britannica.com/technology/belt-drive (visited on 08/02/2018).

[3] Joseph Edward Shigley. *Shigley's mechanical engineering design*. Tata McGraw-Hill Education, 2011.

[4] Antonino Risitano. *Mechanical design*. Crc Press, 2011.

[5] Peter RN Childs. *Mechanical design engineering handbook*. Butterworth-Heinemann, 2013.

[6] Optibelt. *Tecnical manual V-belt drives*. URL: https://www.optibelt.com/fileadmin/content/pdf/Produkte/EN/Optibelt-TH-v-belt-drives.pdf (visited on 08/02/2018).

[7] Anibal De Almeida and Steve Greenberg. "Technology assessment: energy-efficient belt transmissions". In: *Energy and buildings* 22.3 (1995), pp. 245–253.

[8] Plant Engineering. *Basics of belt drives*. URL: https://www.plantengineering.com/single-article/basics-of-belt-drives (visited on 09/02/2018).

[9] Robert B McMillan. *Rotating machinery: practical solutions to unbalance and misalignment*. The Fairmont Press, Inc., 2004.

[10] Flow control. *The importance of shaft alignment*. URL: https://www.flowcontrolnetwork.com/the-importance-of-shaft-alignment/ (visited on 09/02/2018).

[11] M Leonard Euler. "Remarques sur l'effect du frottement dans l'equilibre". In: *Mem. Acad. Sci* 18 (1762), pp. 265–278.

[12] Vlado A Lubarda. "The mechanics of belt friction revisited". In: *International Journal of Mechanical Engineering Education* 42.2 (2014), pp. 97–112.

[13] Osborne Reynolds. "On rolling-friction". In: *Philosophical Transactions of the Royal Society of London* 166 (1876), pp. 155–174.

[14] Kenneth Langstreth Johnson and Kenneth Langstreth Johnson. *Contact mechanics*. Cambridge university press, 1987.

[15] TC Firbank. "Mechanics of the belt drive". In: *International Journal of Mechanical Sciences* 12.12 (1970), pp. 1053–1063.

[16] GG Gerbert. "Paper XII (i) On Flat Belt Slip". In: *Tribology Series*. Vol. 18. Elsevier, 1991, pp. 333–340.

[17] Goran Gerbert. "Belt slip—a unified approach". In: *Journal of Mechanical Design* 118.3 (1996), pp. 432–438.

[18] J Hu et al. “Finite element analysis of V-ribbed belt/pulley system with pulley misalignment using a neural-network-based material model”. In: *Neural Computing and Applications* 18.8 (2009), p. 927.

[19] Lionel Manin et al. “From transmission error measurement to pulley–belt slip determination in serpentine belt drives: Influence of tensioner and belt characteristics”. In: *Mechanism and Machine Theory* 44.4 (2009), pp. 813–821.

[20] Maria Di Napoli et al. “Intelligent Belt Drive Systems in Hybrid Powertrains: a Multipurpose Test Rig”. In: *IFAC-PapersOnLine* 49.21 (2016), pp. 47–53.

[21] Berna Balta, Fazil O Sonmez, and Abdulkadir Cengiz. “Speed losses in V-ribbed belt drives”. In: *Mechanism and Machine Theory* 86 (2015), pp. 1–14.

[22] Bernd Robert Hoehn et al. “Test methods for gear lubricants”. In: *Goriva i maziva: časopis za tribologiju, tehniku podmazivanja i primjenu tekućih i plinovitih goriva i inžinjerstvo izgaranja* 47.2 (2008), pp. 141–152.

[23] Siemens. *SIMOTION, SINAMICS S120 SIMOTICS*. URL: https://www.industry.siemens.com/datapool/industry/drives/Docs/MC/PM21-2013-complete-en.pdf (visited on 02/22/2018).

[24] Siemens. *SINAMICS S120 and SIMOTICS*. URL: https://cache.industry.siemens.com/dl/files/019/109747019/att_918077/v1/motion-control-drives-D21-4-complete--English-2017.pdf (visited on 02/22/2018).

[25] ETH messtechnik. *DRVL*. URL: https://www.eth-messtechnik.de/en/index.html.

[26] ETH messtechnik. *DRVL operator manual*. URL: https://www.eth-messtechnik.de/downloads/DRVL-operator_manual.pdf.

[27] ETH messtechnik. *DRVL Datasheet*. URL: https://www.eth-messtechnik.de/_datenblaetter/en/drvl.pdf.

[28] ETH messtechnik. *Torque Measuring Module*. URL: https://www.eth-messtechnik.de/en/measuring_technology/analyzers/analyzers/measuring-module_valueMasterBase.html.

[29] INA FAG Schaefflar. *Radial Insert Ball Bearings and Housing Units*. URL: https://www.schaeffler.com/remotemedien/media/_shared_media/08_media_library/01_publications/schaeffler_2/catalogue_1/downloads_6/sg_1_de_en.pdf (visited on 04/12/2018).

[30] SKF. *Roling Bearings*. URL: https://www.motion-products.ru/upload/iblock/672/672e909694906ba8831e53d3d9d8545b.pdf (visited on 06/20/2018).

[31] SKF. *The SKF model for calculating the frictional moment*. URL: http://www.skf.com/binary/21-299767/The%20SKF%20model%20for%20calculating%20the%20frictional%20movement_tcm_12-299767.pdf (visited on 06/20/2018).

[32] Ramada aços. *Inproving together*. URL: http://www.ramada.pt/ficheiros_upload/ramada-aa-os_catalogo170316130332.pdf (visited on 05/28/2018).

[33] F. Ramada. *Nitroration*. URL: http://www.ramada.pt/pt/servicos/acos-ligas/tratamentos-termicos/nitruracao.html (visited on 05/28/2018).

[34] Walter D Pilkey and Deborah F Pilkey. *Peterson's stress concentration factors*. John Wiley & Sons, 2008.

[35] Rexroth Bosch Group. *Aluminum Structural Framing System*. URL: http://www.boschrexroth.ch/country_units/america/united_states/en/Documentation_and_Resources/a_downloads/AluminumStructuralFraming_Catalog.pdf (visited on 04/13/2018).

[36] Simões Morais. *Desenho técnico básico 3*. 2007.

[37] Schaeffler. *Plain Bearings*. URL: http://www.bearingsandindustrialsupply.com/pdf/Schaeffler%20Bearings.pdf (visited on 06/20/2018).

[38] Automotion Components. *Linear Motion Handbook*. URL: https://www.automotioncomponents.co.uk/files/catalogues/lin.pdf (visited on 05/17/2018).

[39] steelnumber. *C45 (1.0503)*. URL: http://www.steelnumber.com/en/steel_composition_eu.php?name_id=152 (visited on 06/05/2018).

[40] steelnumber. *X2CrNiMo17-12-2 (1.4404)*. URL: http://www.steelnumber.com/en/steel_composition_eu.php?name_id=104 (visited on 06/05/2018).

Appendixes

Appendix A: Motors technical drawings

back view

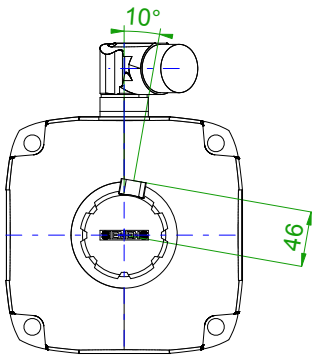

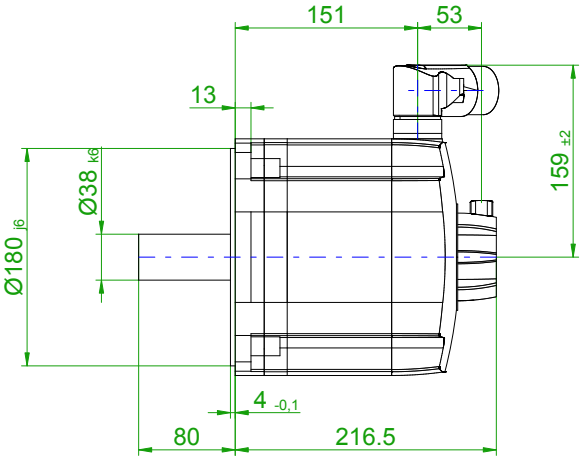

front view

center hole
DIN 332-DR M12

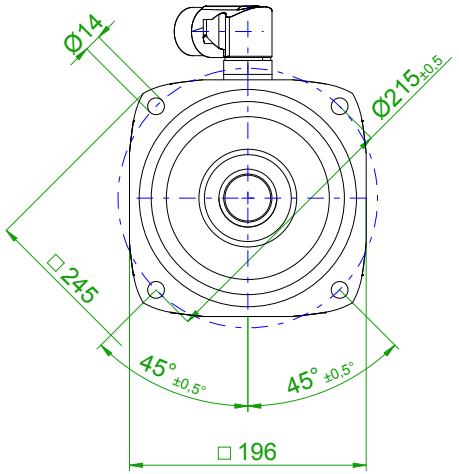

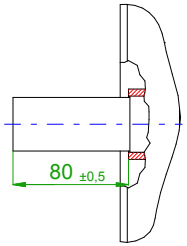

6-pole plug size 1.5
for power

10-pole
signal plug

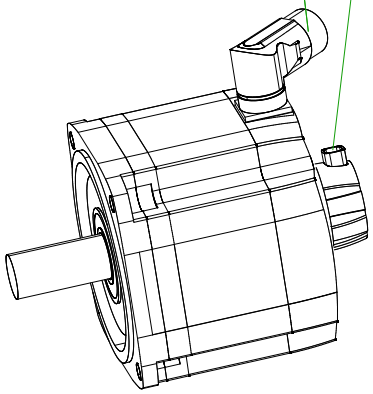

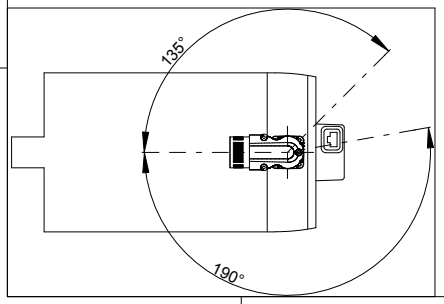

		SIEMENS
Einheit / unit: mm	Synchron-Servomotor Synchronous Servo Motor:	1FT7102-5AF71-1BG1
nicht tolerierte Maße / not toleranced dimensions: ±1	Optionen / options:	
	Gewicht / mass:	26.1 kg
Maßstab / scale: ohne / without	Bemerkung / notice:	
CAD CREATOR 2.2 (WWW-Version V02.20.00.00)		Druckdatum / print date: 22.06.2018

back view

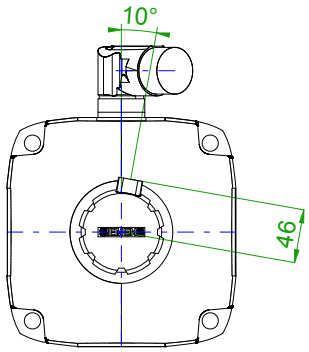

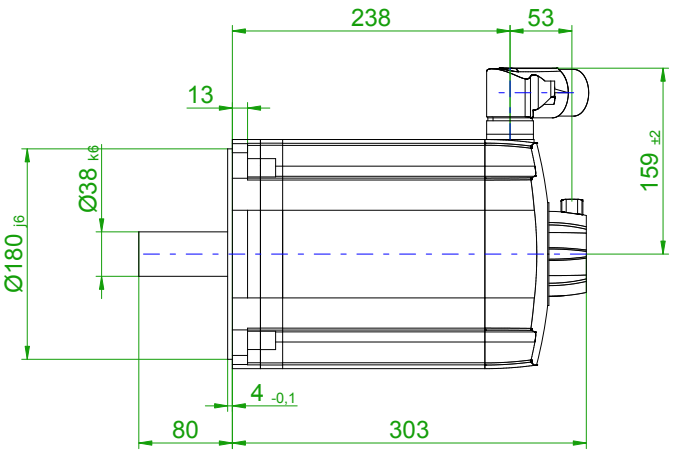

front view

center hole
DIN 332-DR M12

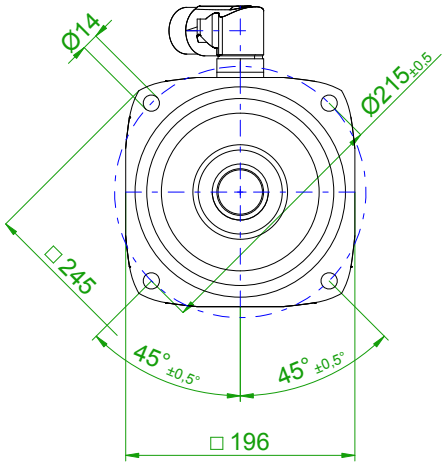

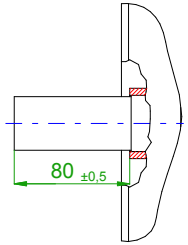

6-pole plug size 1.5
for power

10-pole
signal plug

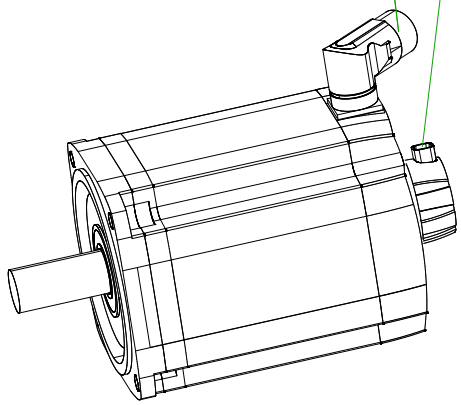

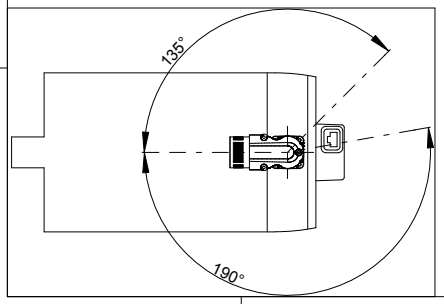

	SIEMENS	
Einheit / unit: mm	Synchron-Servomotor Synchronous Servo Motor:	1FT7105-5AF71-1BG1
nicht tolerierte Maße / not toleranced dimensions: ±1	Optionen / options:	
	Gewicht / mass:	44.2 kg
Maßstab / scale: ohne / without	Bemerkung / notice:	
CAD CREATOR 2.2 (WWW-Version V02.20.00.00)		Druckdatum / print date: 22.06.2018

Appendix B: Optibelt software reports

Optibelt-CAP Drive Calculation

Power Transmission

Sender

Tel. No.	:	Tel. No.	:
Fax No.	:	Fax No.	:
E-Mail	:	E-Mail	:
Internet	:	Internet	:

Drive Calculation

V Belts 2 Pulley Drive

No.	: C000000007	Date	: 20.04.2018	SN	: 88040108
Project	: 0001	Drawing No.	: 0001	Drive	: 0001

Dear Sir or Madam

As discussed on the telephone we have used your drive information in a series of calculations.

The drive requires:

- 2 x Optibelt-SK wedge belt SPZ 772 Ld

Driver pulley:

- Optibelt-KS pulley for taper bush TB SPZ 90-2
- Optibelt-TB taper bush 1610 (Bore-diameter 14-42 mm)

Driven pulley:

- Optibelt-KS pulley for taper bush TB SPZ 90-2
- Optibelt-TB taper bush 1610 (Bore-diameter 14-42 mm)

We suggest the use of Optibelt tension measuring gauges when setting belt tensions. When belts are being installed the drive should be rotated by hand for at least two revolutions to ensure that the belts are settled properly into the pulley grooves. A check of belt tensions is recommended after 0.5 to 4 hours running. After the first check the belt tension should be re-checked every 6 to 12 months. Further information on 'Installation and Maintenance' is available in a variety of Optibelt publications.

Should you have questions about our recommendations please contact us at the postal or E-Mail address, telephone or fax number shown.

With best regards

Our 'General Conditions of Sale' are applicable.

Customer: **Sender:**

optibelt
Power Transmission

Drive Calculation

based on a theoretical belt life of 25000 h

V Belts 2 Pulley Drive

No.	: C000000007	Data	: 20.04.2018	SN	: 88040108
Project	: 0001	Drawing No.	: 0001	Drive	: 0001

The drive requires:

- 2 x Optibelt-SK wedge belt SPZ 772 Ld

- Optibelt-KS pulley for taper bush TB SPZ 90-2
- Optibelt-TB taper bush 1610 (Bore-diameter 14-42 mm)
- Optibelt-KS pulley for taper bush TB SPZ 90-2
- Optibelt-TB taper bush 1610 (Bore-diameter 14-42 mm)

					Deviation / Hints	
Type of driver unit		**:**	**Electric motor**			
Type of driven unit		**:**	**Generator and exciter**			
Calculation Power	PB	:	6.60	kW		
Driver Power	**P**	**:**	**5.50**	**kW**		
Torque at driver pulley	M	:	18	Nm		
Driver speed	**n1**	**:**	**3000**	**1/min**		
Required driven speed	**n2**	**:**	**3000**	**1/min**	**0**	**1/min**
Datum diameter pulley 1	**dd1**	**:**	**90.00**	**mm**		
Datum diameter pulley 2	**dd2**	**:**	**90.00**	**mm**		
Datum length	Ld	:	772	mm		
Actual centres	**C**	**:**	**244.63**	**mm**	**---**	**mm**
Actual drive ratio	i	:	1.00		---	%
Adjustment required for belt fitting	y	:	15.00	mm		
Adjustment required for belt tensioning	x	:	15.00	mm		
Actual service factor	**c2**	**:**	**1.15**			
Belt speed	v	:	14.14	m/s		
Flex rate	fB	:	36.62	1/s		
Power per belt	PN	:	3.65	kW		
Arc of contact factor	c1	:	1.00			
Belt length factor	c3	:	0.87			
Arc of contact on small pulley	ß	:	180.00	°		
Pulley face width	b	:	28.00	mm		
Span length	l	:	244.63	mm		
Calculated number of belts	**z1**	**:**	**2.09**		**given c2 =**	**1.20**
Weight of drive		:	2.33	kg		
Static shaft load (Initial installation)	Samin	:	692	---		
Static shaft load (Re-tension)	Samin	:	532	N		
Dynamic shaft load	Sadyn	:	486	N		

Tensioning recommendations			**Initial installation**	**Re-tension**
given c2 = 1.20			new belts	existing belts
1. OPTIKRIK 0 + I	Static tension per belt	:	173 N	133 N
2. Load/deflection tension gauge	Load at centre of span	:	25 N	25 N
	Deflection	:	5.82 mm	6.56 mm
3. Length additinal value per 1000 mm belt length		:	2.97 mm	2.26 mm
4. Optibelt-TT 3 / TT mini Tension Tester	Frequency	:	98.81 1/s	86.67 1/s

Our 'General conditions of Sale' are applicable.

Release 6.031 29.09.2017 Pricelist 06/2012

Optibelt-CAP Drive Calculation

Power Transmission

Sender

Tel. No.	:	Tel. No.	:
Fax No.	:	Fax No.	:
E-Mail	:	E-Mail	:
Internet	:	Internet	:

Drive Calculation

V Belts 2 Pulley Drive

No.	: C000000008	Date	: 20.04.2018	SN	: 88040108
Project	: 0001	Drawing No.	: 0001	Drive	: 0001

Dear Sir or Madam

As discussed on the telephone we have used your drive information in a series of calculations.

The drive requires:

- 2 x Optibelt-SK wedge belt SPZ 1237 Ld S=C plus

Driver pulley:

- Optibelt-KS pulley for taper bush TB SPZ 85-2
- Optibelt-TB taper bush 1610 (Bore-diameter 14-42 mm)

Driven pulley:

- Optibelt-KS pulley for taper bush TB SPZ 200-2
- Optibelt-TB taper bush 2012 (Bore-diameter 14-50 mm)

We suggest the use of Optibelt tension measuring gauges when setting belt tensions. When belts are being installed the drive should be rotated by hand for at least two revolutions to ensure that the belts are settled properly into the pulley grooves. A check of belt tensions is recommended after 0.5 to 4 hours running. After the first check the belt tension should be re-checked every 6 to 12 months. Further information on 'Installation and Maintenance' is available in a variety of Optibelt publications.

Should you have questions about our recommendations please contact us at the postal or E-Mail address, telephone or fax number shown.

With best regards

Our 'General Conditions of Sale' are applicable.

Customer: **Sender:**

optibelt
Power Transmission

Drive Calculation

based on a theoretical belt life of 25000 h

V Belts 2 Pulley Drive

No.	: C000000008	Data	: 20.04.2018	SN	: 88040108
Project	: 0001	Drawing No.	: 0001	Drive	: 0001

The drive requires:

- 2 x Optibelt-SK wedge belt SPZ 1237 Ld S=C plus

- Optibelt-KS pulley for taper bush TB SPZ 85-2
- Optibelt-TB taper bush 1610 (Bore-diameter 14-42 mm)
- Optibelt-KS pulley for taper bush TB SPZ 200-2
- Optibelt-TB taper bush 2012 (Bore-diameter 14-50 mm)

					Deviation / Hints	
Type of driver unit		**:**	**Electric motor**			
Type of driven unit		**:**	**Generator and exciter**			
Calculation Power	PB	:	6.60	kW		
Driver Power	**P**	**:**	**5.50**	**kW**		
Torque at driver pulley	M	:	18	Nm		
Driver speed	**n1**	**:**	**3000**	**1/min**		
Required driven speed	**n2**	**:**	**1275**	**1/min**	**25**	**1/min**
Datum diameter pulley 1	**dd1**	**:**	**85.00**	**mm**		
Datum diameter pulley 2	**dd2**	**:**	**200.00**	**mm**		
Datum length	Ld	:	1237	mm		
Actual centres	**C**	**:**	**390.43**	**mm**	**---**	**mm**
Actual drive ratio	i	:	2.35		-2.0	%
Adjustment required for belt fitting	y	:	15.00	mm		
Adjustment required for belt tensioning	x	:	20.00	mm		
Actual service factor	**c2**	**:**	**1.28**			
Belt speed	v	:	13.35	m/s		
Flex rate	fB	:	21.59	1/s		
Power per belt	PN	:	3.73	kW		
Arc of contact factor	c1	:	0.99			
Belt length factor	c3	:	0.95			
Arc of contact on small pulley	ß	:	163.06	°		
Pulley face width	b	:	28.00	mm		
Span length	l	:	386.17	mm		
Calculated number of belts	**z1**	**:**	**1.87**		**given c2 =**	**1.20**
Weight of drive		:	4.64	kg		
Static shaft load (Initial installation)	Samin	:	724	---		
Static shaft load (Re-tension)	Samin	:	557	N		
Dynamic shaft load	Sadyn	:	523	N		

Tensioning recommendations			**Initial installation**	**Re-tension**
given c2 = 1.20			new belts	existing belts
1. OPTIKRIK 0 + I	Static tension per belt	:	183 N	141 N
2. Load/deflection tension gauge	Load at centre of span	:	25 N	25 N
	Deflection	:	9.19 mm	10.35 mm
3. Length additinal value per 1000 mm belt length		:	3.16 mm	2.42 mm
4. Optibelt-TT 3 / TT mini Tension Tester	Frequency	:	64.39 1/s	56.48 1/s

Our 'General conditions of Sale' are applicable.

Release 6.031 29.09.2017 Pricelist 06/2012

Appendix C: Complete results of reaction loads calculation

Table A1: Complete reactions results: Part 1 for shafts fatigue desing

Cal.		1.1	1.2	1.3	1.4	1.5	1.6	1.7	1.8
D_1	[m]	0.067	0.067	0.067	0.067	0.067	0.067	0.067	0.067
D_2	[m]	0.224	0.224	0.224	0.224	0.224	0.224	0.224	0.224
a	[m]	0.5	0.5	0.5	0.5	0.5	0.5	0.5	0.5
b	[m]	0	0	0	0	0.05	0.05	0.05	0.05
θ_t	[°]	0	0	15	15	0	0	15	15
θ_c	[°]	0	-90	0	-90	0	-90	0	-90
T_i	[N]	1800	1800	1800	1800	1800	1800	1800	1800
M_r	[Nm]	47	47	47	47	47	47	47	47
T_1	[N]	1121	1136	1129	1126	1127	1149	1128	1133
T_2	[N]	701.5	714.1	693.7	723.1	705.1	713	702.3	726.5
R_A^x	[N]	0	93.02	-16.78	89.15	184.5	93.02	167.5	86.85
R_A^y	[N]	-93.15	132.5	-97.38	107	-83.45	393.4	-85.06	366.6
R_A^z	[N]	2545	2548	2544	2548	2552	2548	2551	2548
R_A^r	[N]	2547	2552	2546	2550	2553	2578	2552	2574
R_B^x	[N]	0	0	0	0	0	0	0	0
R_B^y	[N]	27.26	-104.7	29.15	-97.13	17.57	-181	18.61	-173.1
R_B^z	[N]	-744.8	-748.2	-744.2	-748.1	-751.5	-748.2	-750.9	-748
R_B^r	[N]	745.3	755.5	744.8	754.3	751.7	769.8	751.1	767.7
R_C^x	[N]	0	-27.82	482.1	456.3	-184.5	-212.4	304	278.9
R_C^y	[N]	93.15	38.36	184.3	116.6	60.73	6.284	147.9	82.31
R_C^z	[N]	-2545	-2548	-2394	-2406	-2567	-2571	-2483	-2495
R_C^r	[N]	2547	2548	2401	2409	2568	2571	2487	2496
R_D^x	[N]	0	0	0	0	0	0	0	0
R_D^y	[N]	-27.26	54.66	-116	-27.42	5.151	86.74	-81.42	4.535
R_D^z	[N]	744.8	748.2	659.2	665.2	767.2	770.6	700.5	706.3
R_D^r	[N]	745.3	750.2	669.3	665.7	767.2	775.4	705.2	706.4

Table A2: Complete reactions results: Part 2 for bearings static calculation

Cal.		2.1	2.2	2.3	2.4	2.5	2.6	2.7	2.8
D_1	[m]	0.067	0.067	0.067	0.067	0.067	0.067	0.067	0.067
D_2	[m]	0.224	0.224	0.224	0.224	0.224	0.224	0.224	0.224
a	[m]	0.5	0.5	0.5	0.5	0.5	0.5	0.5	0.5
b	[m]	0	0	0	0	0.05	0.05	0.05	0.05
θ_t	[°]	0	0	15	15	0	0	15	15
θ_c	[°]	0	-90	0	-90	0	-90	0	-90
T_i	[N]	1800	1800	1800	1800	1800	1800	1800	1800
M_r	[Nm]	0	0	0	0	0	0	0	0
T_1	[N]	911.3	924.9	911.3	908.1	916	935.5	915.1	918.1
T_2	[N]	911.3	924.9	911.3	941.6	916	923.4	915.1	938.9
R_A^x	[N]	0	0	-16.78	-7.154	184.5	1.13e-14	167.5	-6.97
R_A^y	[N]	0	93.15	0	66.29	0	354.1	0	327
R_A^z	[N]	2545	2545	2544	2545	2552	2545	2551	2545
R_A^r	[N]	2545	2547	2544	2545	2552	2569	2551	2565
R_B^x	[N]	0	0	0	0	0	0	0	0
R_B^y	[N]	0	-93.15	0	-85.21	0	-169.5	0	-161.5
R_B^z	[N]	-744.8	-744.8	-744.2	-744.6	-751.5	-744.8	-750.9	-744.6
R_B^r	[N]	744.8	750.6	744.2	749.4	751.5	763.9	750.9	761.9
R_C^x	[N]	0	0	482.1	484.1	-184.5	-184.5	304	306.1
R_C^y	[N]	0	-93.15	0	-106.4	0	-93.15	0	-103.7
R_C^z	[N]	-2545	-2545	-2394	-2392	-2567	-2567	-2483	-2482
R_C^r	[N]	2545	2547	2394	2395	2567	2569	2483	2484
R_D^x	[N]	0	0	0	0	0	0	0	0
R_D^y	[N]	0	93.15	0	99.28	0	93.15	0	96.72
R_D^z	[N]	744.8	744.8	659.2	658.7	767.2	767.2	700.5	700.1
R_D^r	[N]	744.8	750.6	659.2	666.2	767.2	772.8	700.5	706.7

Table A3: Complete reactions results: Part 3 for bearings life calculation

Cal.		3.1	3.2	3.3	3.4	3.5	3.6	3.7	3.8
D_1	[m]	0.224	0.224	0.224	0.224	0.224	0.224	0.224	0.224
D_2	[m]	0.224	0.224	0.224	0.224	0.224	0.224	0.224	0.224
a	[m]	0.5	0.5	0.5	0.5	0.5	0.5	0.5	0.5
b	[m]	0	0	0	0	0.05	0.05	0.05	0.05
θ_t	[°]	0	0	15	15	0	0	15	15
θ_c	[°]	0	-90	0	-90	0	-90	0	-90
T_i	[N]	1800	1800	1800	1800	1800	1800	1800	1800
M_r	[Nm]	18.33	18.33	18.33	18.33	18.33	18.33	18.33	18.33
T_1	[N]	981.8	1030	984.7	976.3	986.7	1055	987.4	999.4
T_2	[N]	818.2	858.2	815.3	911.9	822.3	844.6	821.6	898.2
R_A^x	[N]	0	36.66	0	13.75	180	36.66	180	13.39
R_A^y	[N]	0	363.3	0	330.9	12.64	617.7	12.75	584.9
R_A^z	[N]	2545	2545	2545	2545	2545	2545	2545	2545
R_A^r	[N]	2545	2571	2545	2566	2545	2619	2545	2611
R_B^x	[N]	0	0	0	0	0	0	0	0
R_B^y	[N]	0	-326.6	0	-317.1	-12.64	-401.1	-12.75	-391.5
R_B^z	[N]	-744.8	-744.8	-744.8	-744.8	-744.8	-744.8	-744.8	-744.8
R_B^r	[N]	744.8	813.3	744.8	809.5	744.9	846	744.9	841.4
R_C^x	[N]	0	-36.66	465.9	452.6	-180	-216.7	292	279.1
R_C^y	[N]	0	-259.6	33.87	-269.1	-12.64	-272.2	20.68	-274.4
R_C^z	[N]	-2545	-2545	-2458	-2463	-2545	-2545	-2524	-2529
R_C^r	[N]	2545	2558	2458	2478	2545	2559	2524	2544
R_D^x	[N]	0	0	0	0	0	0	0	0
R_D^y	[N]	0	296.3	-33.87	282.9	12.64	308.9	-20.68	287.8
R_D^z	[N]	744.8	744.8	719.4	720.9	744.8	744.8	738.7	740.2
R_D^r	[N]	744.8	801.6	720.2	774.4	744.9	806.3	739	794.1

Appendix D: Technical drawings

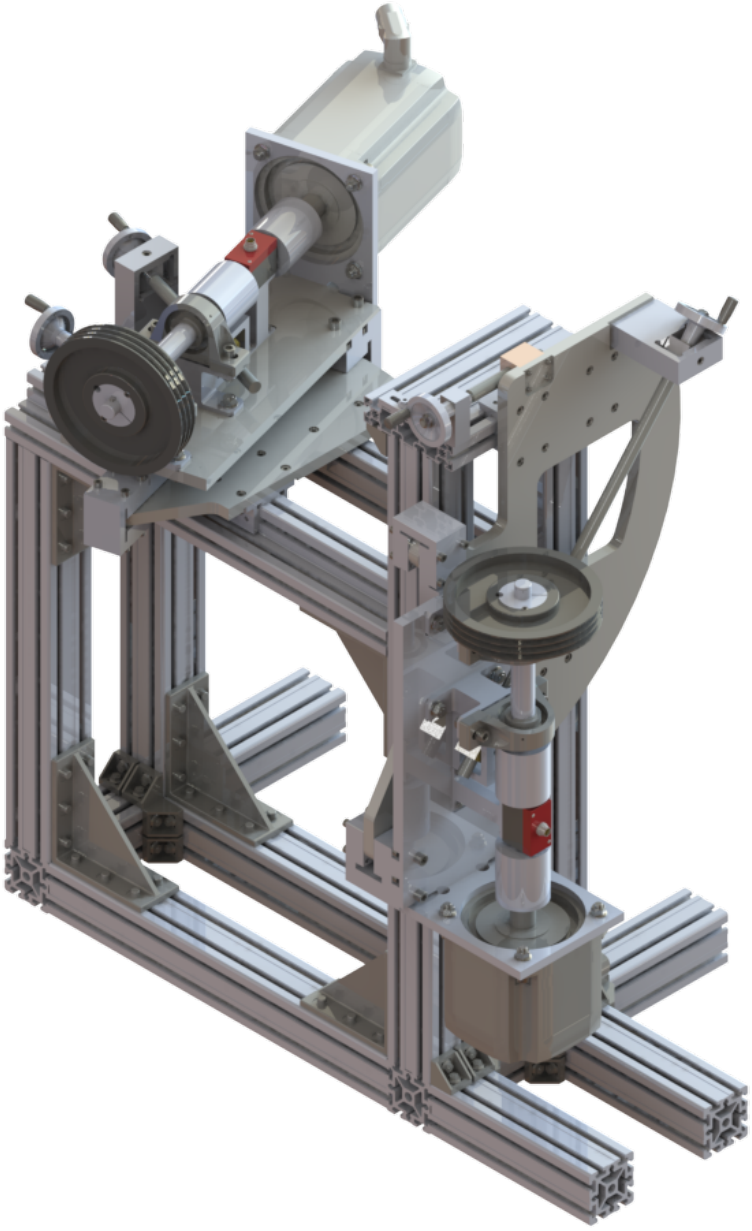

ITEM	QTY.	DESIGNAÇÃO	DADOS TÉCNICOS
1	2	Perfil Bosch 90x90	L=1080mm
2	1	Perfil Bosch 45x180	L=500mm
3	1	Perfil Bosch 45x180	L=140mm
4	2	Perfil Bosch 90x90	L=700mm
5	2	Perfil Bosch 45x90x90L	L=770mm
6	2	Perfil Bosch 90x90	L=320mm
7	2	Perfil Bosch 90x90	L=700mm
8	1	Perfil Bosch 90x90	L=140
9	2	Perfil Bosch 90x90	L=600mm
10	8	Connector	Bosch - Heavy-duty connector
11	32	Kit de aperto Connector	Bosch - Mounting kit
12	64	Bracket	Bosch - Bracket 45X45
13	1	EcoSlide 45x45x160	Bosch
14	24	Parafuso CHC	ISO 4762 M8 x 25
15	1	Base entreixo	
16	24	Porca H	ISO - 4032 - M8
17	7	Carro de fixação GdL linear	Slider_flat_lockable_N10
18	15	Parafuso CHC	ISO 4762 M8 x 20
19	5	EcoSlide 45x45x80	Bosch
20	50	Parafuso BHC	ISO 7380 - M4 x 12
21	14	Chapa compensação	10mm bearing shim 0.1mm thick
22	14	Carro guia linear livre	Slider_flat_N10
23	7	Porca de fixação EcoSlide	Sliding_block_N10_steel_galvanized_M8
24	4	Manivela	Automotion Components - L1458.D080
25	4	Porca H com flange	ISO - 4161 - M10
26	8	Casquilho	d12x5x4

BELT DRIVE TEST RIG

DEmec FEUP

Documento nº BDTR Lista de peças 01

Lista de peças

	NOME	DATA
DESENHOU	Pedro José de Freitas	25/06/2018
VERIFICOU		
APROVOU		

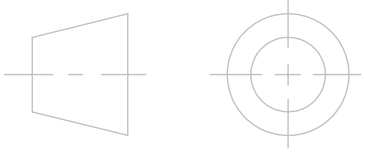

SCALE:1:5 | PÁGINA 1 DE 4 | A4

ITEM	QTY.	DESIGNAÇÃO	DADOS TÉCNICOS
27	4	Chaveta paralela	Parallel key A4 x 4 x 14 DIN 6885
28	4	Casquilho	d12x20x6
29	4	Chumaceira axial	SKF - PCMW 122401.5 E
30	1	Suporte do fuso entreixo	
31	4	Chumaceira radial com emcosto	SKF - PCMF 121417 E
32	1	Fuso entreixo	Automotion Components - L1320.R20-4-1.0
33	4	Porca T	Bosch - T nut 10(M8)
34	4	Parafuso H com flange	Collar screw - Bosch L=20mm
35	2	Porca de fuso GdL linear	Automotion Components L1334.R20-04
36	8	Porca H	ISO - 4032 - M5
37	8	Parafuso CHC	ISO 4762 M5 x 50
38	1	Base axial offset	
39	1	Suporte do fuso Axxial Offset	
40	1	Fuso Axial Offset	Automotion Components - L1320.R20-4-1.0
41	6	Enconto de aperto	
42	12	Chumaceira axial	SKF - PCMW 325401.5 E
43	4	Chumaceira radial	SKF - PCM 161820 E
44	2	Chumaceira axial	SKF - PCMW 183201.5 E
45	2	Suporte pino	
46	2	C de frente	
47	2	Pino	ISO 2338 - 16 h8 x 40 - St
48	48	Parafuso CHC	ISO 4762 M8 x 30
49	10	Suporte chumaceira plana	
50	6	Ponta de parafuso s/cabeça	ISO 4026 M12 x 40 - 14H
51	4	Suporte de chumaceira	
52	2	Base angular	

BELT DRIVE TEST RIG

DEmec FEUP

Documento nº BDTR Lista de peças 02

Lista de peças

	NOME	DATA
DESENHOU	Pedro José de Freitas	25/06/2018
VERIFICOU		
APROVOU		

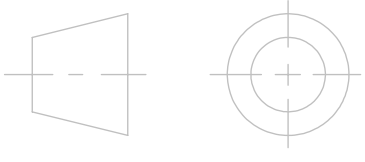

SCALE:1:5 | PÁGINA 2 DE 4 | A4

ITEM	QTY.	DESIGNAÇÃO	DADOS TÉCNICOS
53	4	Ponta de parafuso s/ cabeça	ISO 4026 - M10 x 30
54	2	Bucha cónica	optibelt - 2012_25
55	2	Polia	Optibelt - tb_spz_224_3_2012
56	2	Chaveta paralela	A8 x 7 x 45 DIN 6885
57	2	Casquilho da polia	
58	4	Chumacereira de rolamento	INA FAG - RASEA 35
59	2	Veio	
60	2	Suporte de porca de fuso	
61	8	Porca H	ISO - 4032 - M6
62	2	Base célula de carga	
63	24	Parafuso CHC	ISO 4762 M6 x 30
64	8	Parafuso CHC	ISO 4762 M12 x 25
65	16	Parafuso CHC	ISO 4762 M12 x 45
66	2	Flange	
67	8	Parafuso CHC	ISO 4762 M12 x 30
68	4	C de trás	
69	2	Suporte fuzo GdL angular	
70	8	Chumaceira radial	SKF - PCM 121408 E
71	8	Ponta de parafuso com rebaixo	ISO 4028 - M16 x 16
72	8	Chumaceira axial	SKF - PCMW 142601.5 E
73	2	Cubo fuzo GdL angular	
74	1	Fuso Toe	Automotion Components - L1320.R20-4-1.0
75	2	Porca de fuso GdL angular	Automotion Components - L1335.L20-04
76	24	Porca H com flange	ISO - 4161 - M12
77	8	Parafuso CHC	ISO 4762 M12 x 40
78	1	Fuso Camber	L1320.R20-4-1.0

BELT DRIVE TEST RIG

DEmec FEUP

Documento nº BDTR Lista de peças 03

Lista de peças

	NOME	DATA
DESENHOU	Pedro José de Freitas	25/06/2018
VERIFICOU		
APROVOU		

SCALE:1:5 PÁGINA 3 DE 4 A4

ITEM	QTY.	DESIGNAÇÃO	DADOS TÉCNICOS
79	2	Acoplamento	Siemens - 2LC0591-24B99-0AA0
80	2	Acoplamento	Siemens - 2LC0591-24B99-0AA0
81	8	Parafuso H	ISO 4017 - M3 x 10
82	1	Célula de carga	HSK - DRVL-II 30Nm
83	1	Célula de carga	HSK - DRVL-II 50Nm
84	1	Motor 1	Siemens - 1FT7102-5AF71-1BG1
85	1	Motor 2	Siemens - 1FT7105-5AF71-1BG1

BELT DRIVE TEST RIG

DEmec FEUP

Documento nº BDTR Lista de peças 04

Lista de peças

	NOME	DATA
DESENHOU	Pedro José de Freitas	25/06/2018
VERIFICOU		
APROVOU		

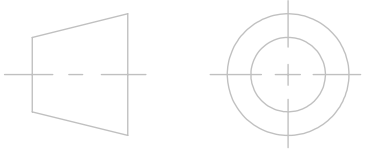

SCALE:1:5 | PÁGINA 4 DE 4 | A4

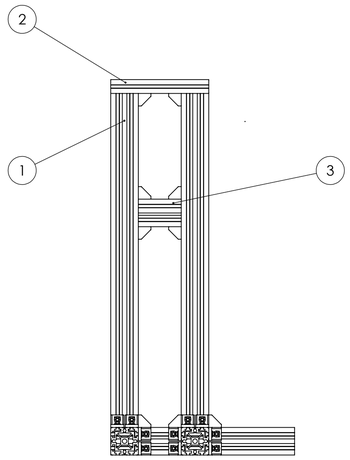

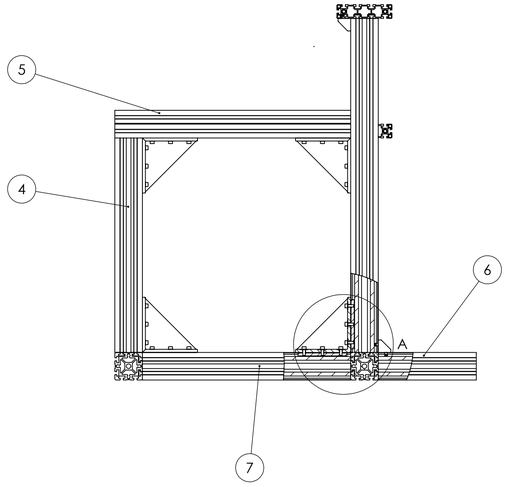

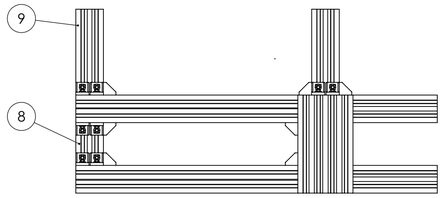

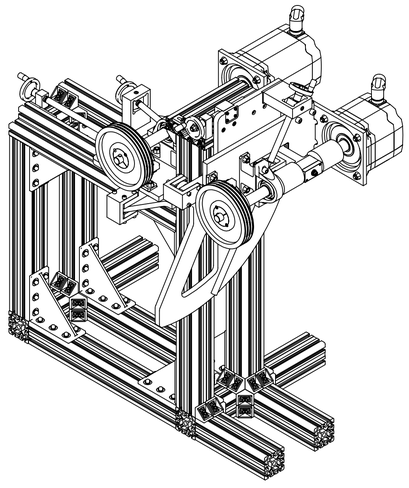

DETAIL A
SCALE 1 : 2

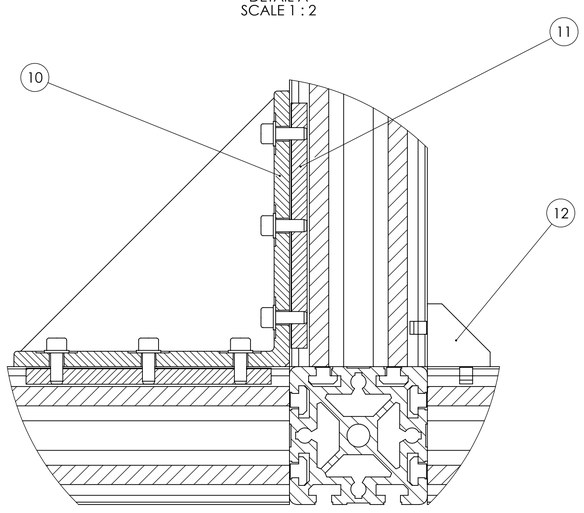

BELT DRIVE TEST RIG			NOME / DATA
DEmec FEUP		DESENHOU	Pedro José de Freitas / 25/06/2018
Desenho nº	BDTR Conjunto 01	VERIFICOU	
Desenho de Conjunto		APROVOU	
		ESCALA:1:5	PÁGINA 1 DE 4 / A1

DETAIL A
SCALE 1 : 1

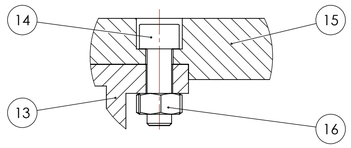

DETAIL B
SCALE 1 : 1

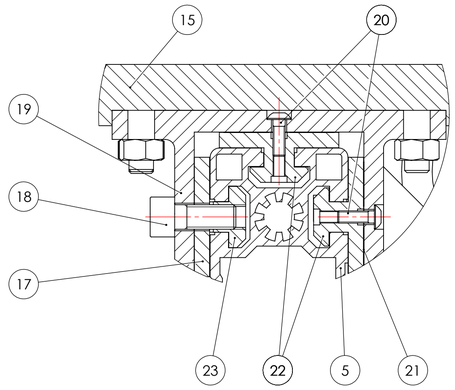

DETAIL C
SCALE 1 : 1

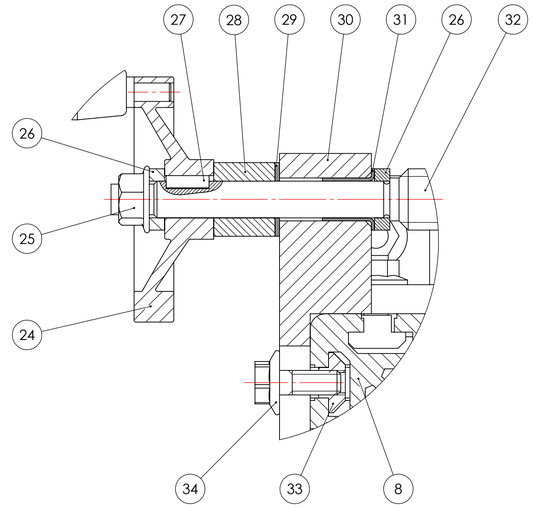

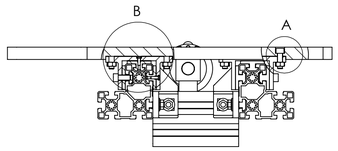

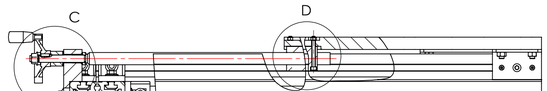

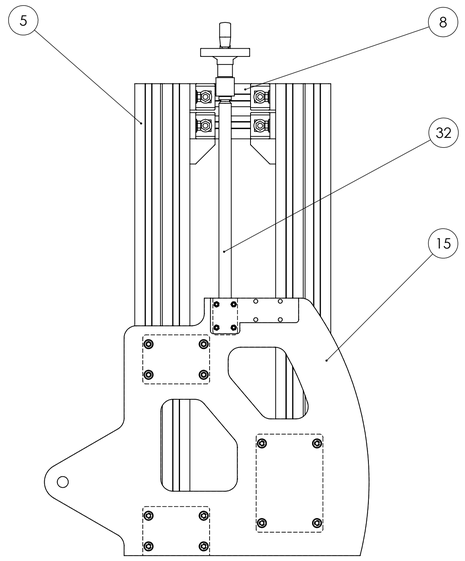

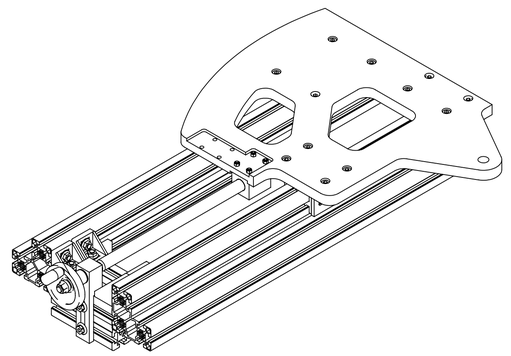

DETAIL D
SCALE 1 : 1

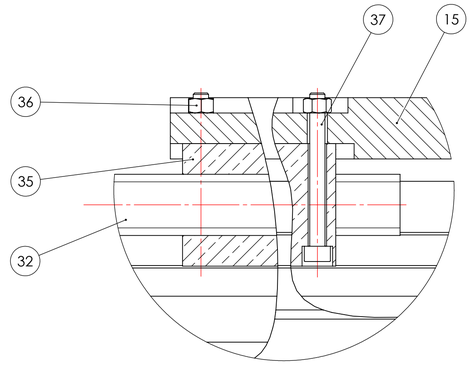

BELT DRIVE TEST RIG			
DEmec FEUP			
Desenho nº	BDTR Conjunto 02		
Desenho de Conjunto			
		NOME	DATA
	DESENHOU	Pedro José de Freitas	25/06/2018
	VERIFICOU		
	APROVOU		
ESCALA:1:5	PÁGINA 2 DE 4	A1	

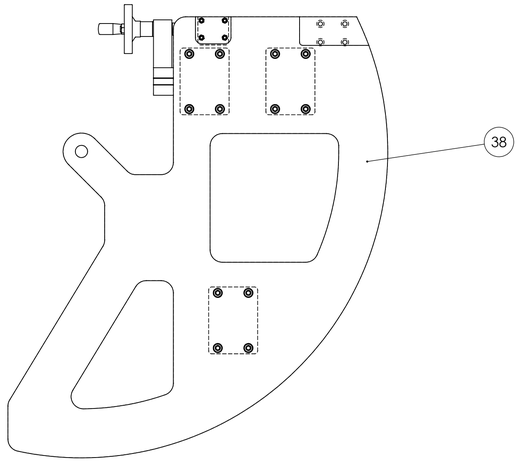

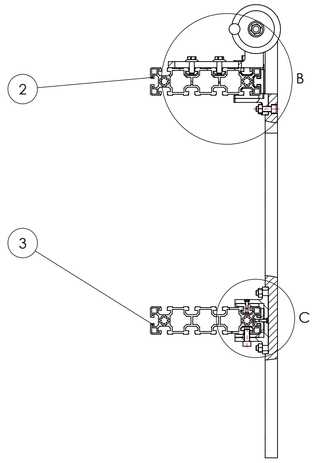

DETAIL B
SCALE 1 : 1

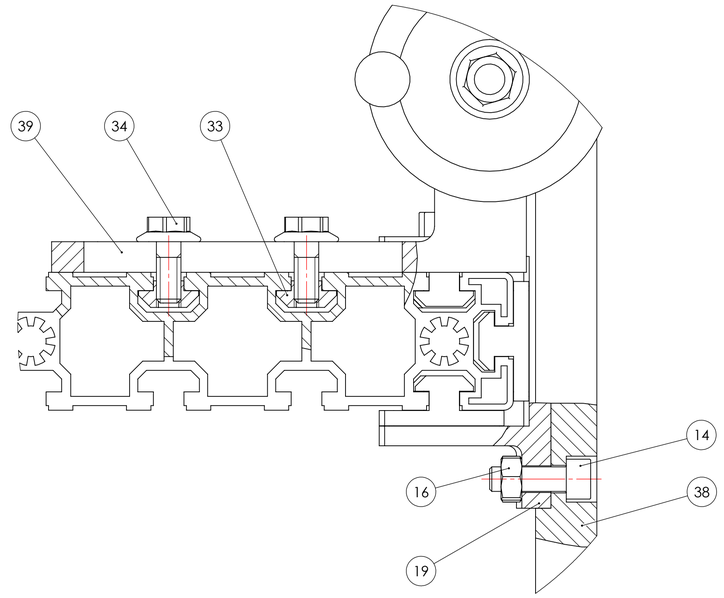

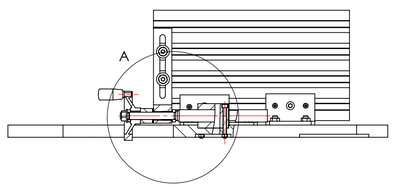

DETAIL A
SCALE 1 : 1

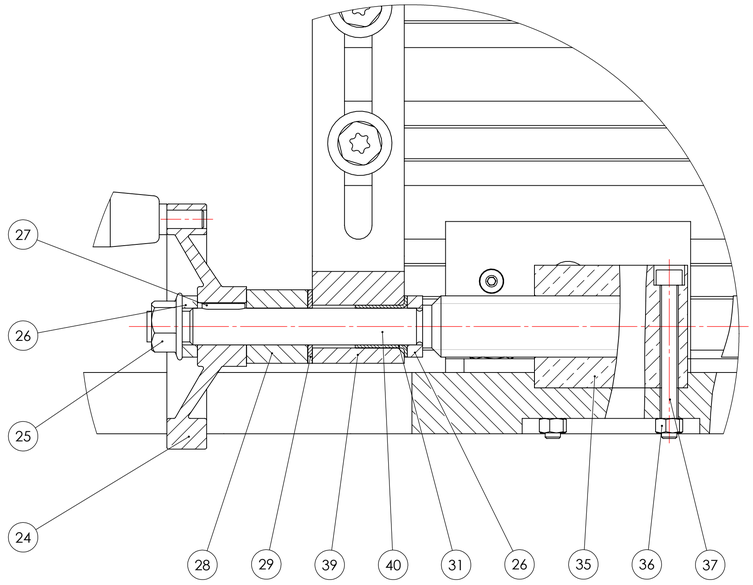

DETAIL C
SCALE 1 : 1

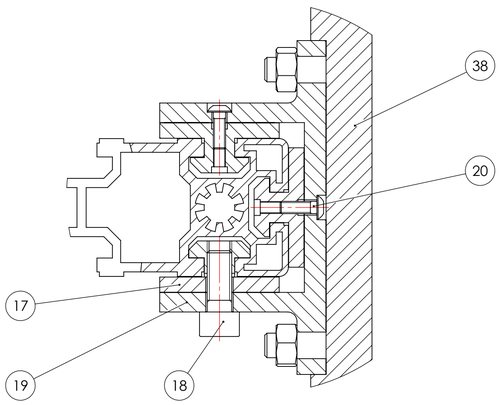

BELT DRIVE TEST RIG			
DEmec FEUP			
Desenho nº	BDTR Conjunto 03		
Desenho de Conjunto			

	NOME	DATA
DESENHOU	Pedro José de Freitas	25/06/2018
VERIFICOU		
APROVOU		

ESCALA:1:5	PÁGINA 3 DE 4	A1

DETAIL A
SCALE 1 : 1

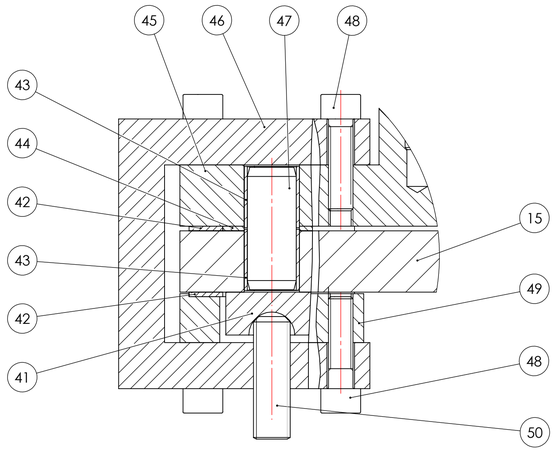

DETAIL B
SCALE 1 : 1

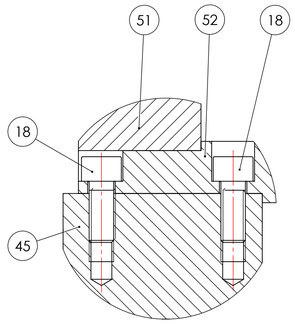

DETAIL C
SCALE 1 : 1

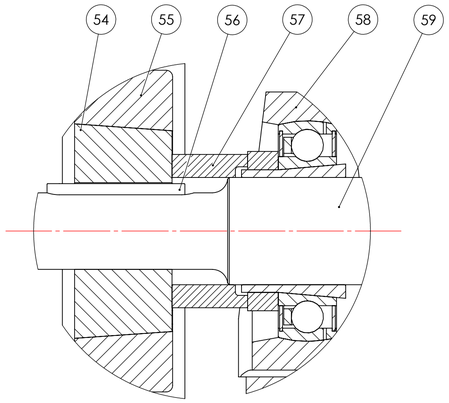

DETAIL D
SCALE 1 : 1

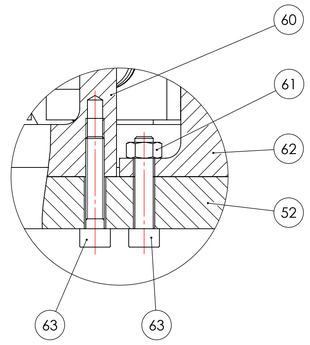

DETAIL E
SCALE 2 : 5

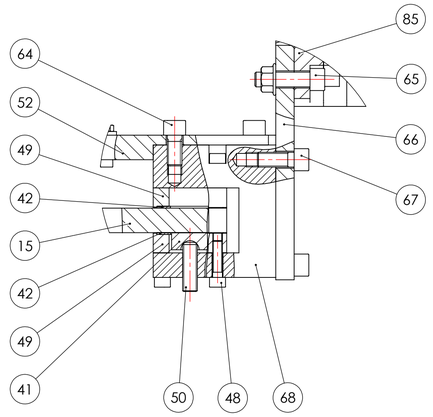

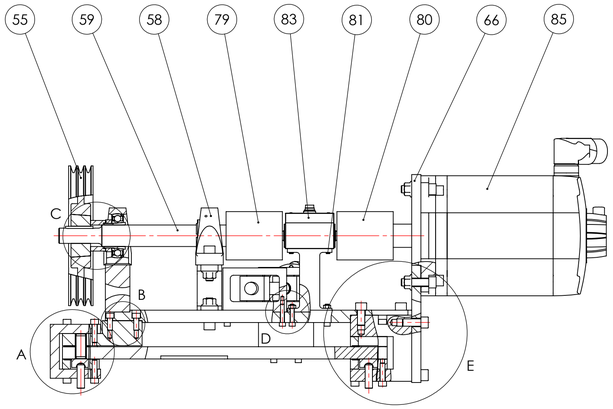

SCALE 1 : 5

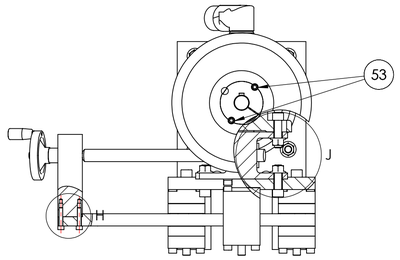

DETAIL H
SCALE 1 : 1

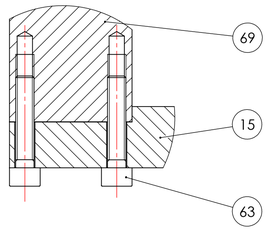

DETAIL J
SCALE 1 : 1

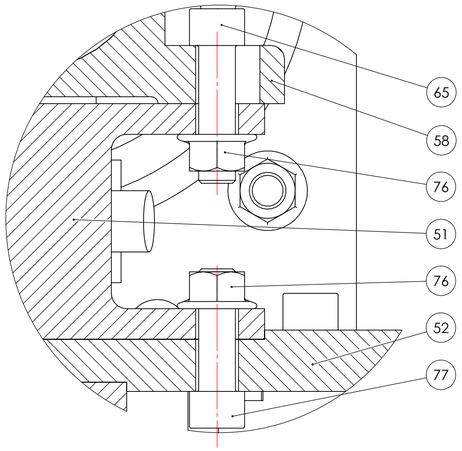

DETAIL F
SCALE 1 : 1

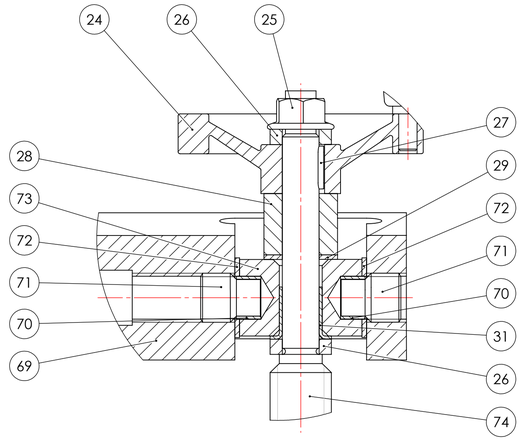

DETAIL G
SCALE 1 : 1

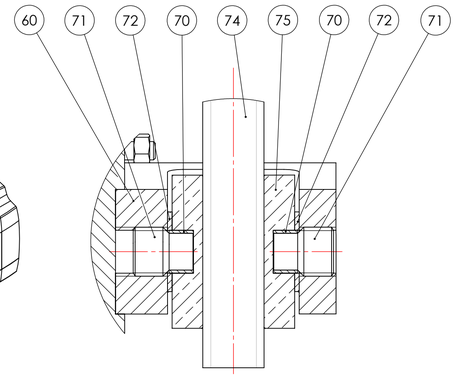

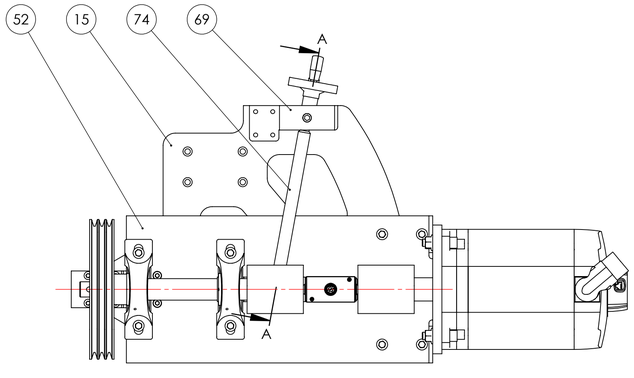

SECTION A-A

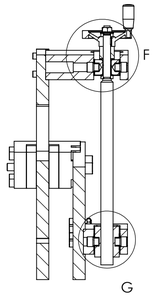

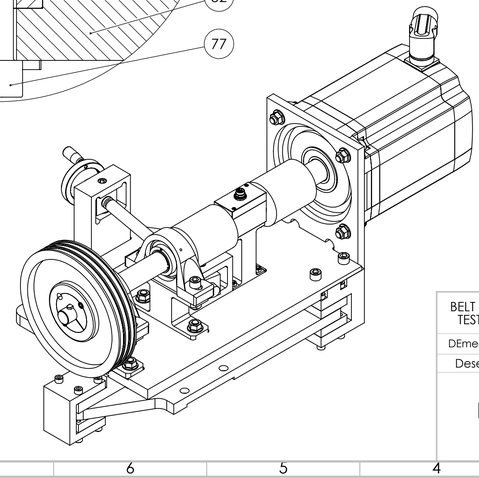

BELT DRIVE TEST RIG			
DEmec FEUP			
Desenho nº	BDTR Conjunto 04		
Desenho de Conjunto			
		NOME	DATA
	DESENHOU	Pedro José de Freitas	25/06/2018
	VERIFICOU		
	APROVOU		
	ESCALA:1:5	PÁGINA 4 DE 4	A1

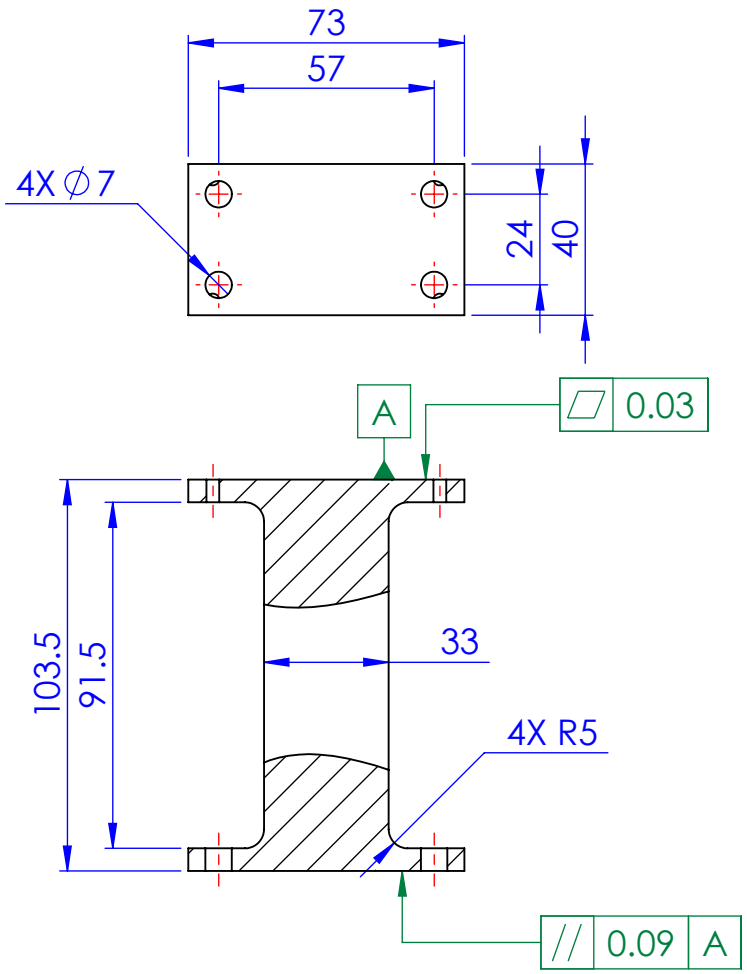

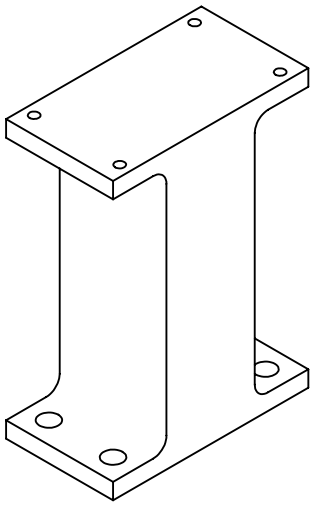

Ra 3,2

Raios não cotados : R=1
Chanfros não cotados : 1x45°

BELT DRIVE TEST RIG	Toleranciamento ISO 8015 Toleranciamentos gerais ISO 2768 - mK Rugosidades gerais ISO 1302 Cantos e chanfors gerais ISO 13175	
DEmec FEUP		
Desenho nº	BDTR Item 62	Quantidade: 2

	NOME	DATA
DESENHOU	Pedro José de Freitas	25/06/2018
VERIFICOU		
APROVOU		

Base células de carga

SCALE:1:2 | SHEET 1 OF 1 | A4

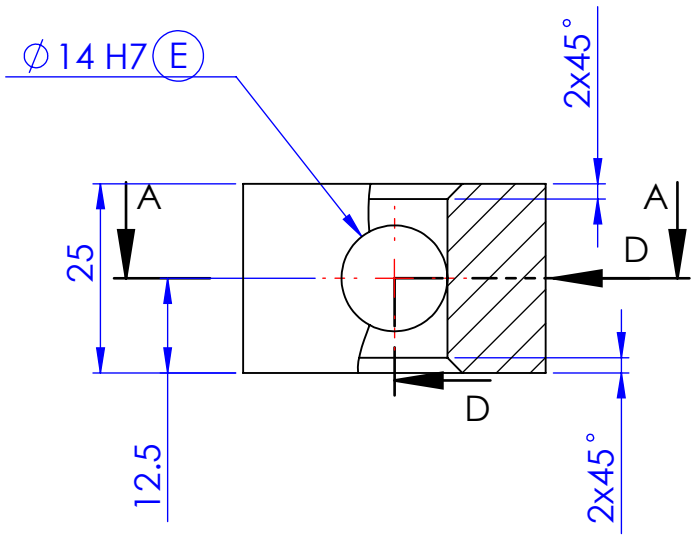

D-D

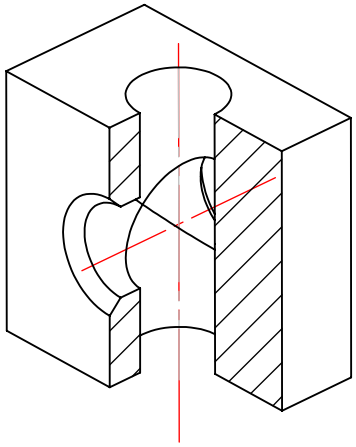

A-A

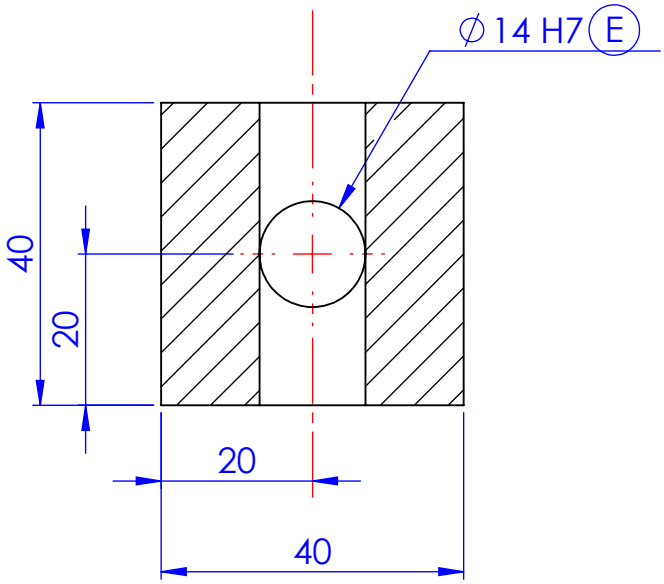

Ra 3,2

Raios não cotados : R=1
Chanfros não cotados : 1x45°

BELT DRIVE TEST RIG	Toleranciamento ISO 8015 Toleranciamentos gerais ISO 2768-mK Rugosidades gerais ISO 1302 Cantos e chanfors gerais ISO 13175	
DEmec FEUP		
Desenho nº	BDTR Item 73	Quantidade: 2

	NOME	DATA
DESENHOU	Pedro José de Freitas	25/06/2018
VERIFICOU		
APROVOU		

Bloco rotativo

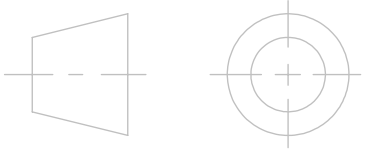

SCALE:1:1 | SHEET 1 OF 1 | A4

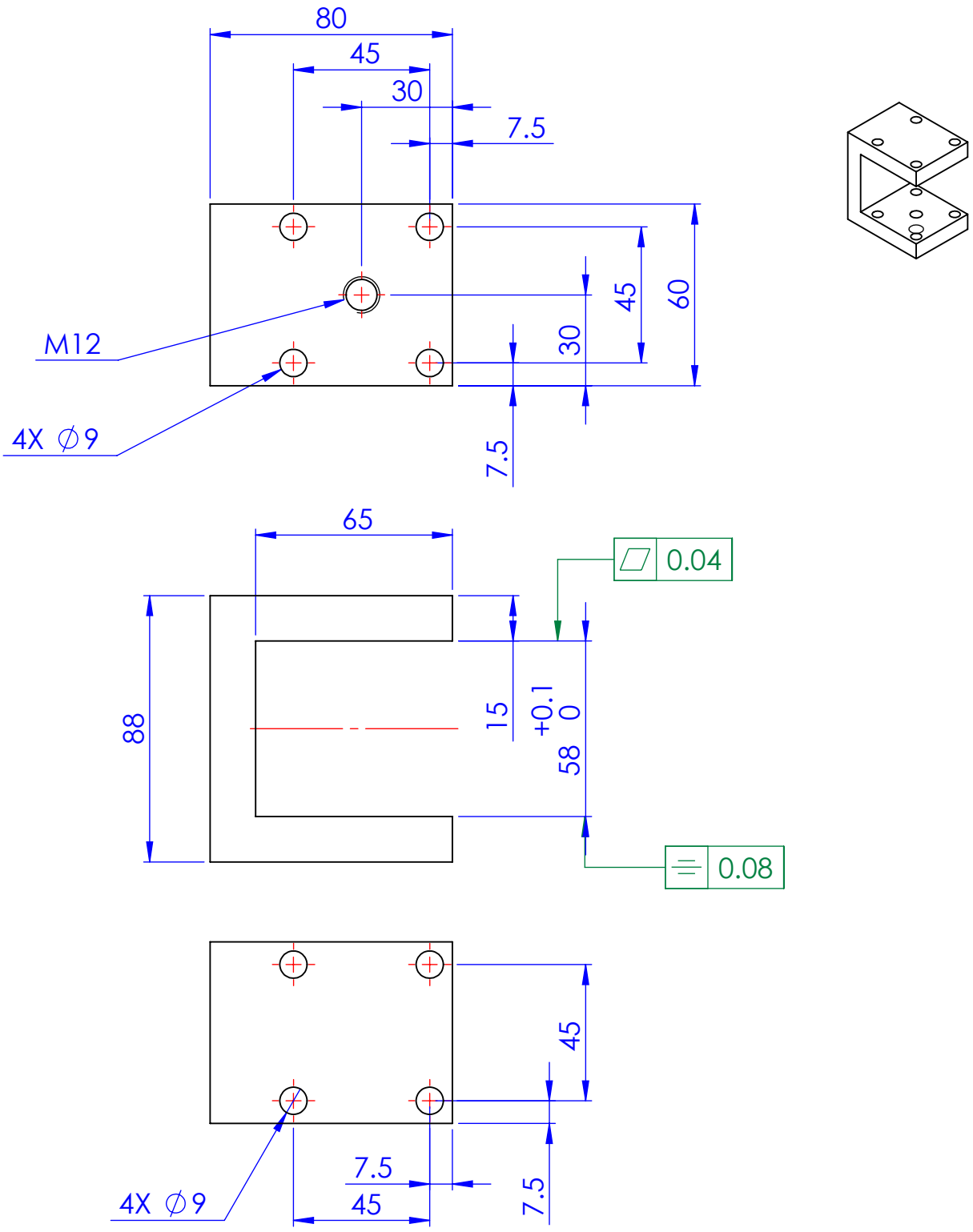

Ra 3,2

Raios não cotados : R=1

Chanfros não cotados : 1x45°

BELT DRIVE TEST RIG	Toleranciamento ISO 8015 Toleranciamentos gerais ISO 2768-mK Rugosidades gerais ISO 1302 Cantos e chanfors gerais ISO 13175	
DEmec FEUP		
Desenho nº	BDTR Item 46	Quantidade: 2

	NOME	DATA
DESENHOU	Pedro José de Freitas	25/06/2018
VERIFICOU		
APROVOU		

C de frente

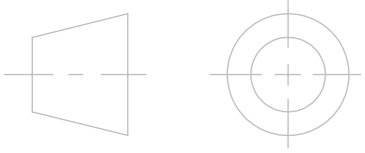

SCALE:1:2 | SHEET 1 OF 1 | A4

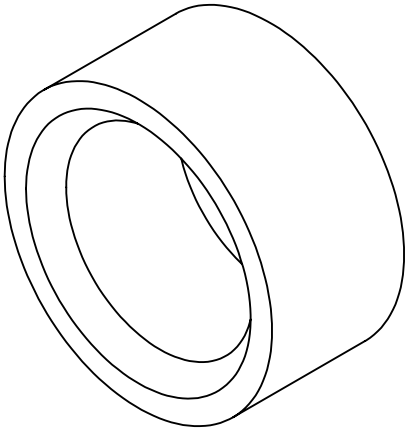

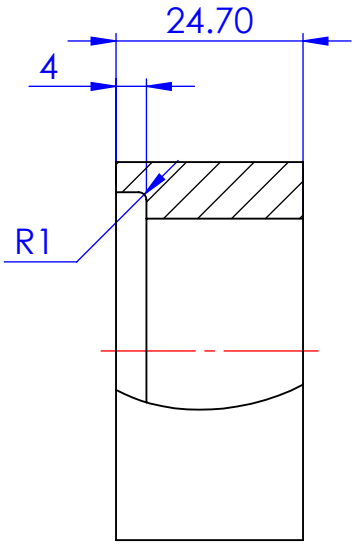

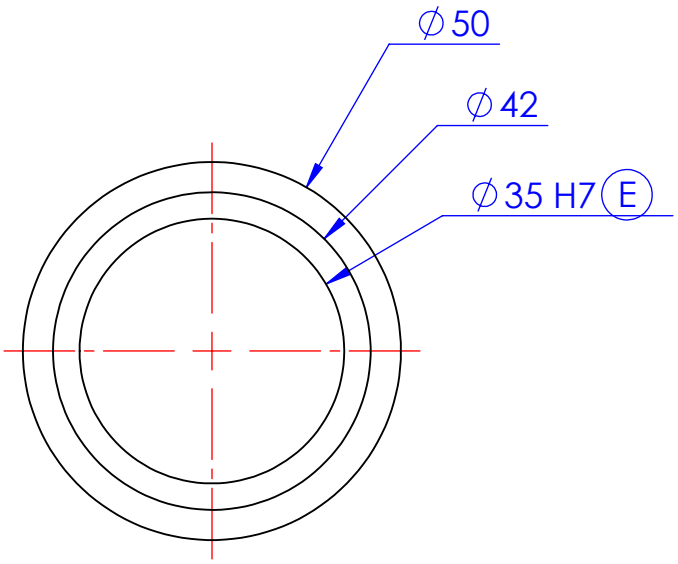

Ra 3,2

Raios não cotados : R=0.5
Chanfros não cotados : 0.5x45°

BELT DRIVE TEST RIG	Toleranciamento ISO 8015 Toleranciamentos gerais ISO 2768-mK Rugosidades gerais ISO 1302 Cantos e chanfors gerais ISO 13175	
DEmec FEUP		
Desenho nº	BDTR Item 57	Quantidade: 2

	NOME	DATA
DESENHOU	Pedro José de Freitas	25/06/2018
VERIFICOU		
APROVOU		

Casquilho da polia

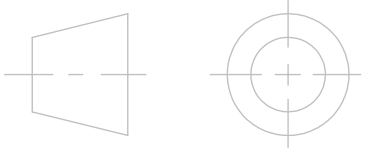

SCALE:1:1	SHEET 1 OF 1	A4

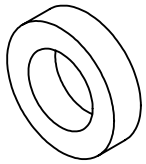

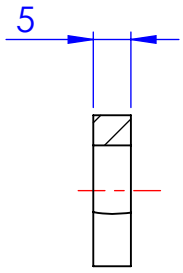

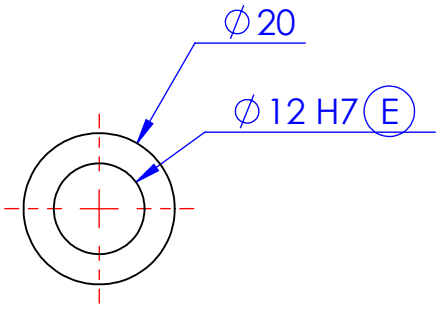

Ra 3,2

Raios não cotados : R=0.5
Chanfros não cotados : 0.5x45°

BELT DRIVE TEST RIG	Toleranciamento ISO 8015 Toleranciamentos gerais ISO 2768-mK Rugosidades gerais ISO 1302 Cantos e chanfors gerais ISO 13175	
DEmec FEUP		
Desenho nº	BDTR Item 26	Quantidade: 8

Casquilho

	NOME	DATA
DESENHOU	Pedro José de Freitas	25/06/2018
VERIFICOU		
APROVOU		

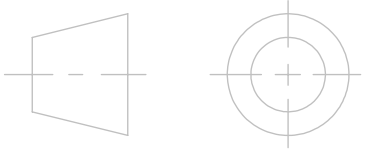

SCALE:1:1 | SHEET 1 OF 1 | A4

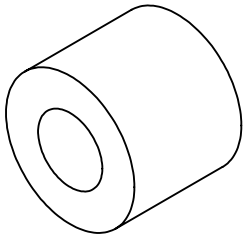

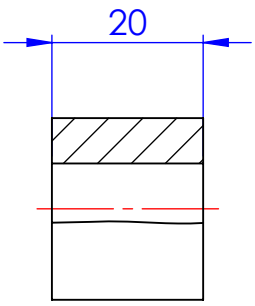

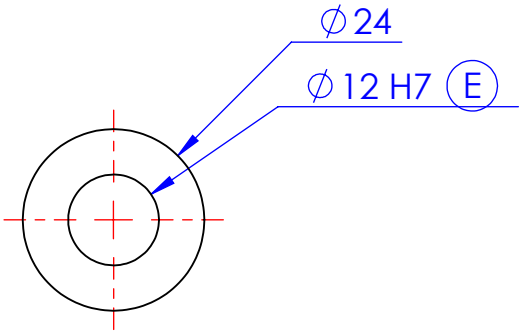

Ra 3,2

Raios não cotados : R=0.5
Chanfros não cotados : 0.5x45°

BELT DRIVE TEST RIG	Toleranciamento ISO 8015 Toleranciamentos gerais ISO 2768-mK Rugosidades gerais ISO 1302 Cantos e chanfors gerais ISO 13175	
DEmec FEUP		
Desenho nº	BDTR Item 28	Quantidade: 4

Casquilho

	NOME	DATA
DESENHOU	Pedro José de Freitas	25/06/2018
VERIFICOU		
APROVOU		

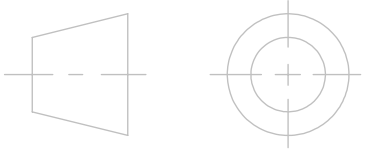

SCALE:1:1 | SHEET 1 OF 1 | A4

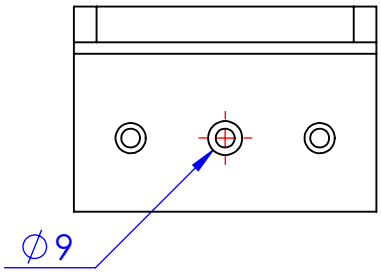

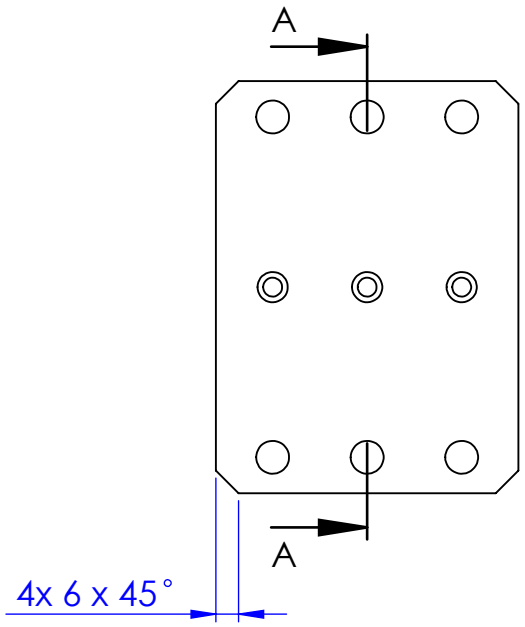

A-A

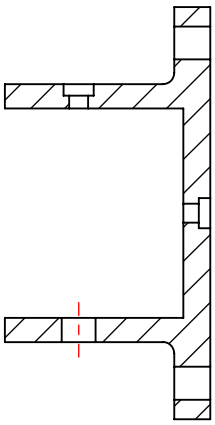

Ra 3,2

Raios não cotados : R=1
Chanfros não cotados : 1x45º

BELT DRIVE TEST RIG	Toleranciamento ISO 8015 Toleranciamentos gerais ISO 2768-mK Rugosidades gerais ISO 1302 Cantos e chanfors gerais ISO 13175	
DEmec FEUP		
Desenho nº	BDTR Item 19	Quantidade: 5

EcoSlide 45x45x80

	NOME	DATA
DESENHOU	Pedro José de Freitas	25/06/2018
VERIFICOU		
APROVOU		

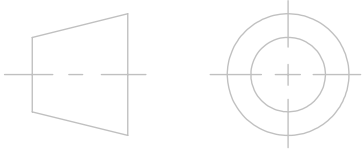

SCALE:1:2 | SHEET 1 OF 1 | A4

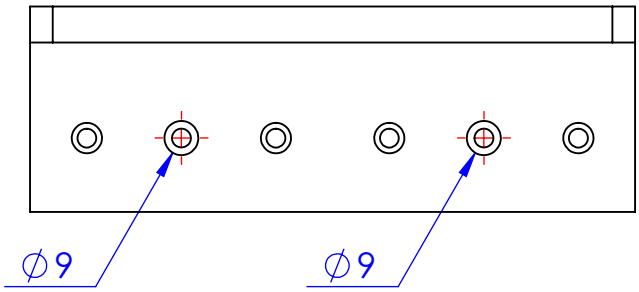

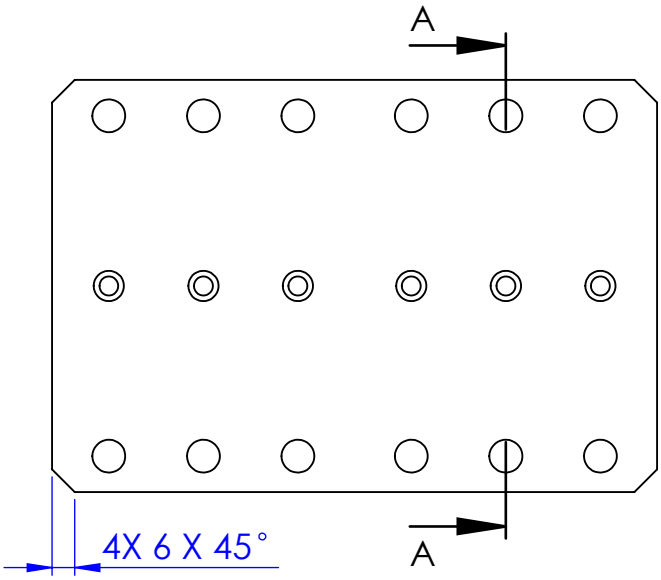

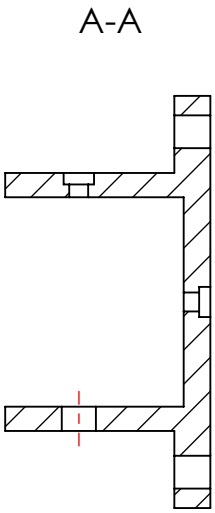

Ra 3,2

Raios não cotados : R=1
Chanfros não cotados : 1x45º

BELT DRIVE TEST RIG	Toleranciamento ISO 8015 Toleranciamentos gerais ISO 2768-mK Rugosidades gerais ISO 1302 Cantos e chanfors gerais ISO 13175	
DEmec FEUP		
Desenho nº	BDTR Item 13	Quantidade: 1

	NOME	DATA
DESENHOU	Pedro José de Freitas	25/06/2018
VERIFICOU		
APROVOU		

EcoSlide_45x45x160

SCALE:1:2 | SHEET 1 OF 1 | A4

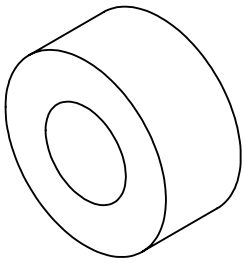

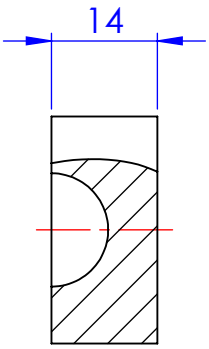

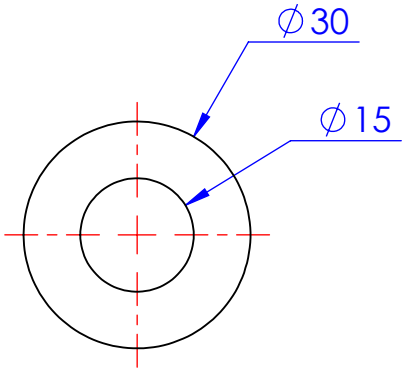

Ra 3,2

Raios não cotados : R=0.5
Chanfros não cotados : 0.5x45°

BELT DRIVE TEST RIG	Toleranciamento ISO 8015 Toleranciamentos gerais ISO 2768-mK Rugosidades gerais ISO 1302 Cantos e chanfors gerais ISO 13175	
DEmec FEUP		
Desenho nº	BDTR Item 41	Quantidade: 6

Encosto de aperto

	NOME	DATA
DESENHOU	Pedro José de Freitas	25/06/2018
VERIFICOU		
APROVOU		

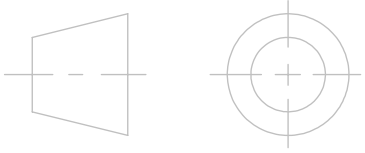

SCALE:1:1 | SHEET 1 OF 1 | A4

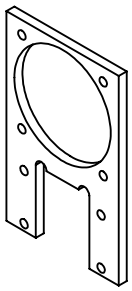

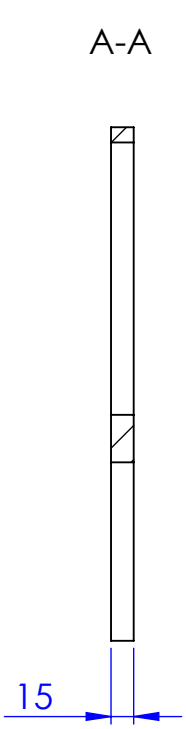

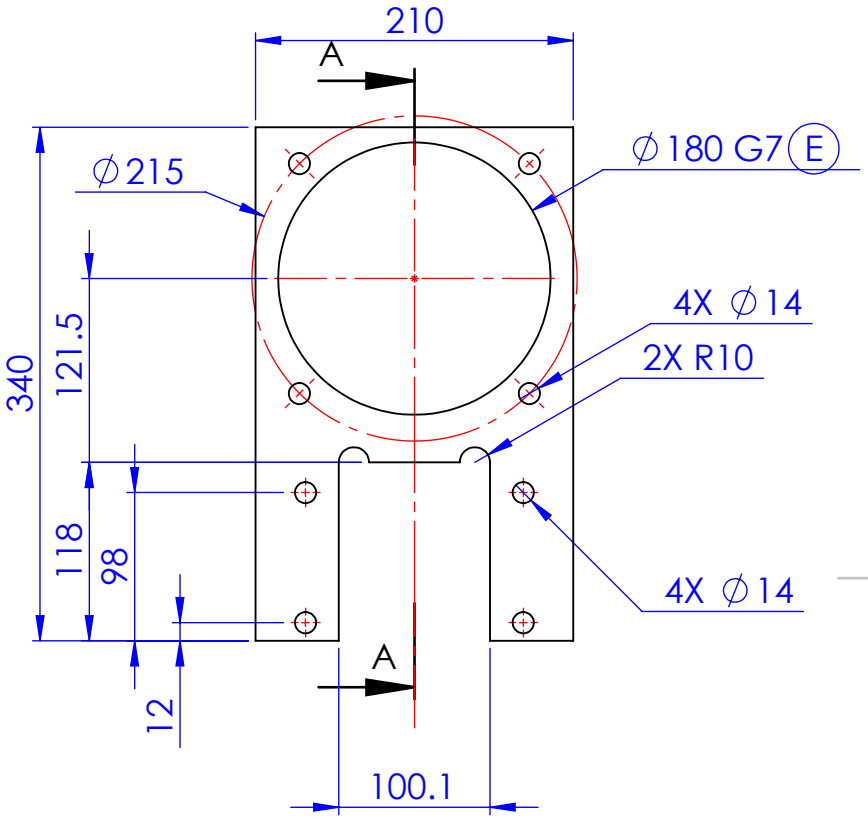

Raios não cotados : R=1
Ra 3,2 Chanfros não cotados : 1x45°

BELT DRIVE TEST RIG	Toleranciamento ISO 8015 Toleranciamentos gerais ISO 2768-mK Rugosidades gerais ISO 1302 Cantos e chanfors gerais ISO 13175	
DEmec FEUP		
Desenho nº	BDTR Item 66	Quantidade: 2

	NOME	DATA
DESENHOU	Pedro José de Freitas	25/06/2018
VERIFICOU		
APROVOU		

Flange

SCALE:1:5 SHEET 1 OF 1 A4

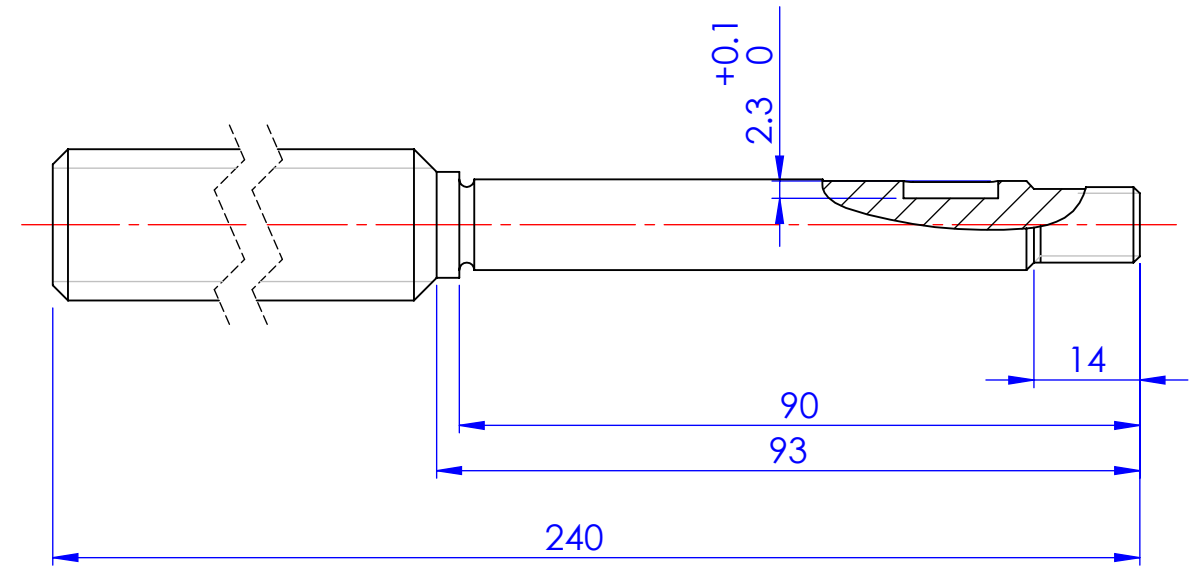

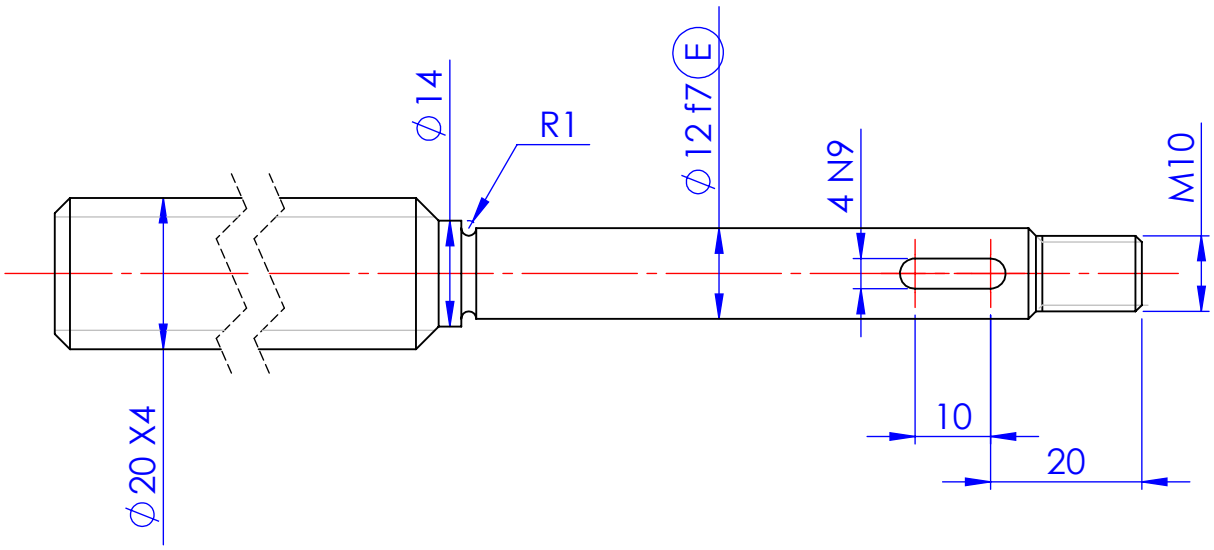

Rosca de Fuso ISO 2901/2903
(DIN 103)

Ra 3,2

Raios não cotados : R=1
Chanfros não cotados : 1x45º

BELT DRIVE TEST RIG	Toleranciamento ISO 8015 Toleranciamentos gerais ISO 2768-mK Rugosidades gerais ISO 1302 Cantos e chanfors gerais ISO 13175	
DEmec FEUP		
Desenho nº	BDTR Item 40	Quantidade: 1

	NOME	DATA
DESENHOU	Pedro José de Freitas	25/06/2018
VERIFICOU		
APROVOU		

Fuso Axial offset

SCALE:1:5 | SHEET 1 OF 1 | A4

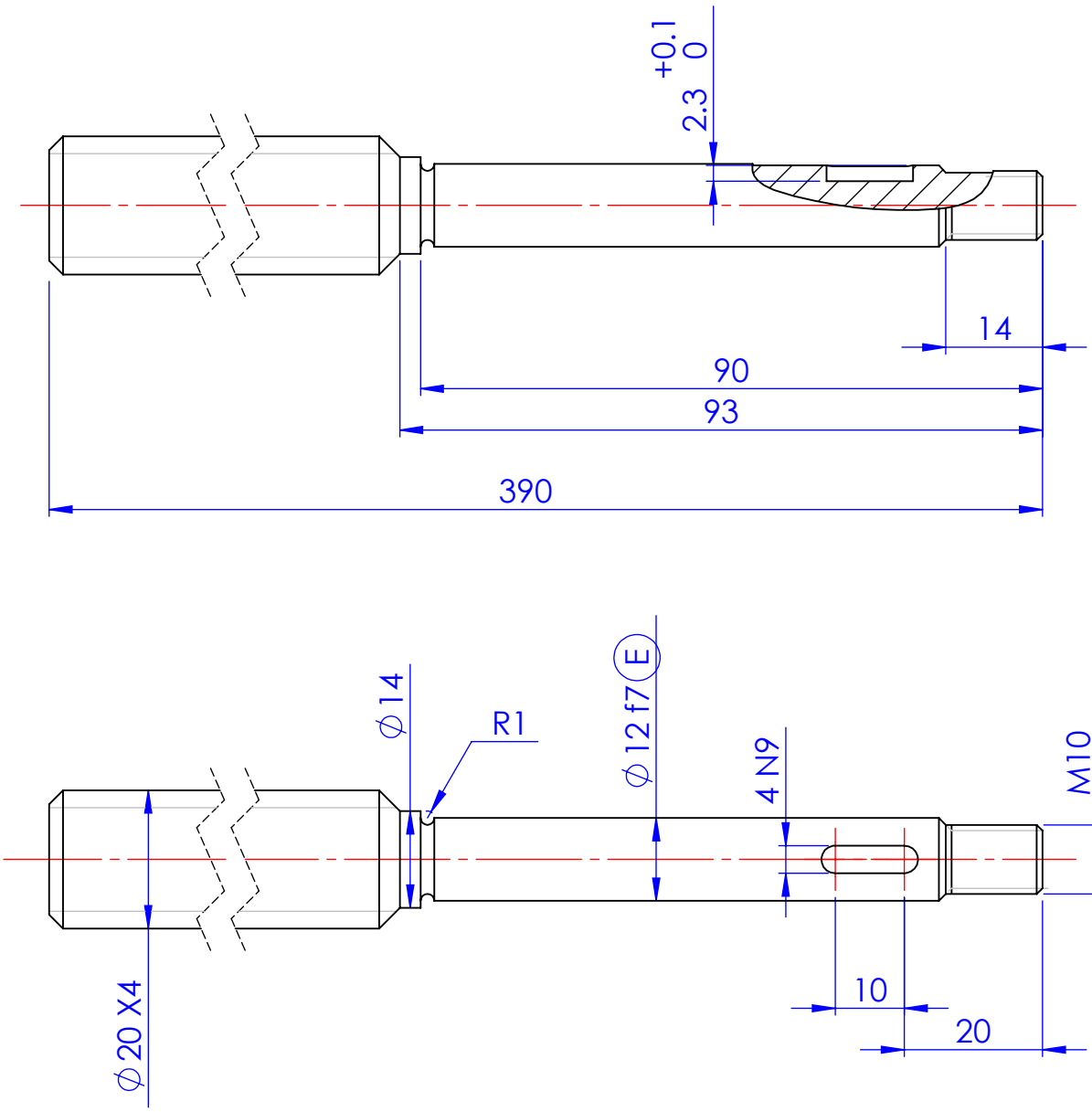

Rosca de Fuso ISO 2901/2903
(DIN 103)

Ra 3,2

Raios não cotados : R=1
Chanfros não cotados : 1x45°

BELT DRIVE TEST RIG	Toleranciamento ISO 8015 Toleranciamentos gerais ISO 2768-mK Rugosidades gerais ISO 1302 Cantos e chanfors gerais ISO 13175	
DEmec FEUP		
Desenho nº	BDTR Item 74	Quantidade: 1

	NOME	DATA
DESENHOU	Pedro José de Freitas	25/06/2018
VERIFICOU		
APROVOU		

Fuso Toe

SCALE:1:5 | SHEET 1 OF 1 | A4

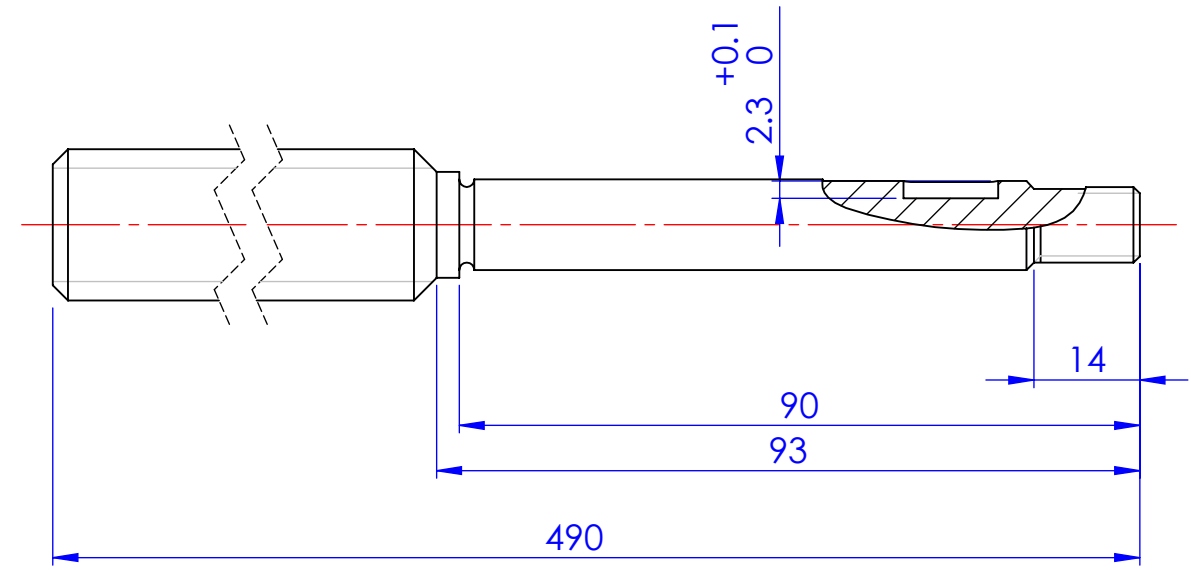

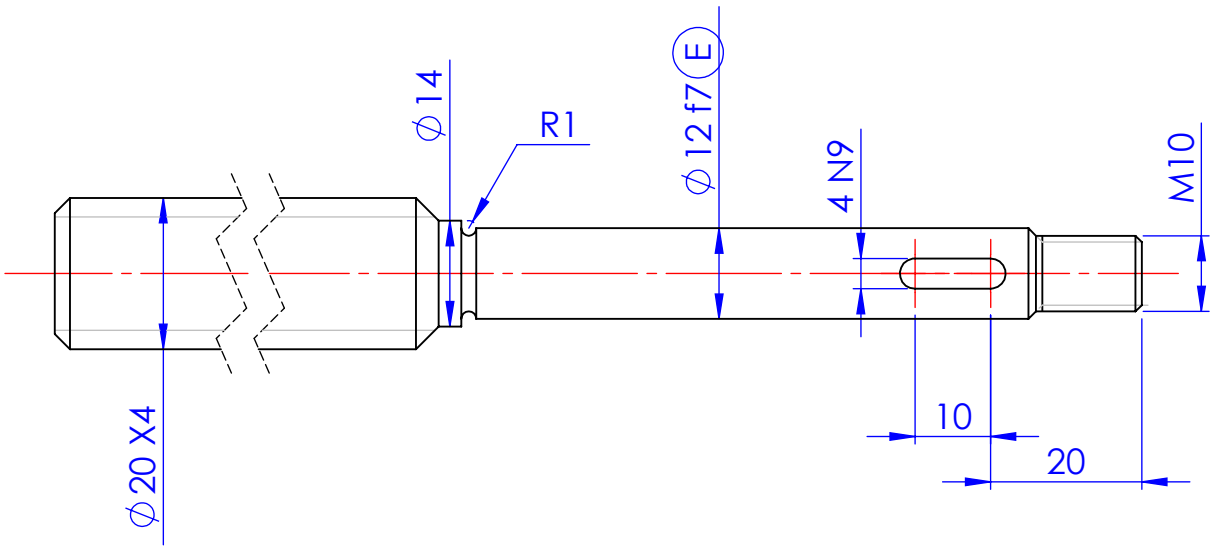

Rosca de Fuso ISO 2901/2903
(DIN 103)

Ra 3,2

Raios não cotados : R=1
Chanfros não cotados : 1x45º

BELT DRIVE TEST RIG	Toleranciamento ISO 8015 Toleranciamentos gerais ISO 2768-mK Rugosidades gerais ISO 1302 Cantos e chanfors gerais ISO 13175	
DEmec FEUP		
Desenho nº	BDTR Item 32	Quantidade: 1

	NOME	DATA
DESENHOU	Pedro José de Freitas	25/06/2018
VERIFICOU		
APROVOU		

Fuso entreeixo

SCALE:1:5 | SHEET 1 OF 1 | A4

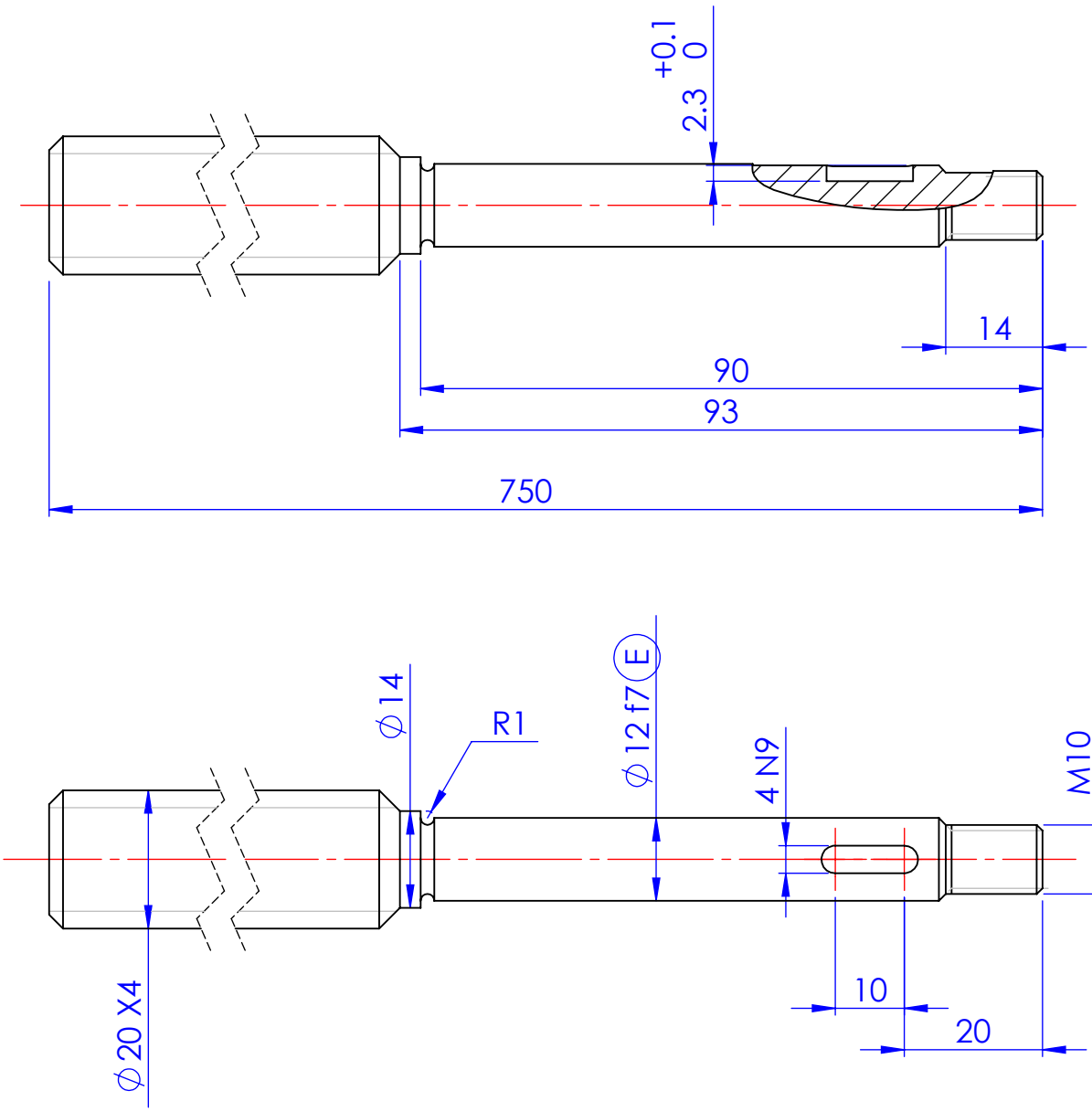

Rosca de Fuso ISO 2901/2903
(DIN 103)

Ra 3,2

Raios não cotados : R=1
Chanfros não cotados : 1x45º

BELT DRIVE TEST RIG	Toleranciamento ISO 8015 Toleranciamentos gerais ISO 2768-mK Rugosidades gerais ISO 1302 Cantos e chanfors gerais ISO 13175	
DEmec FEUP		
Desenho nº	BDTR Item 78	Quantidade: 1

	NOME	DATA
DESENHOU	Pedro José de Freitas	25/06/2018
VERIFICOU		
APROVOU		

Fuso Camber

SCALE:1:5 | SHEET 1 OF 1 | A4

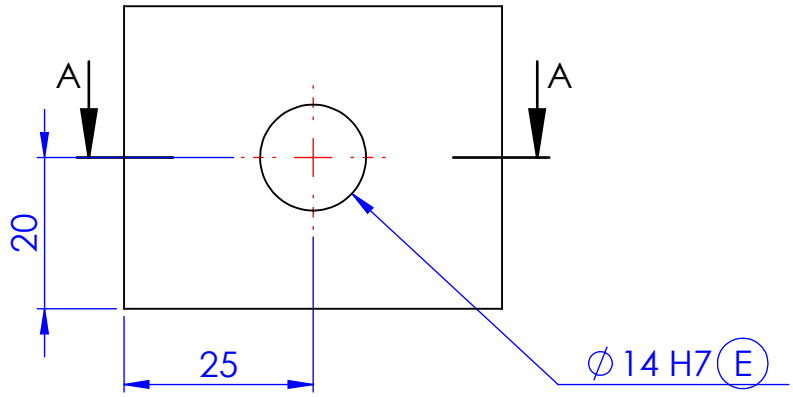

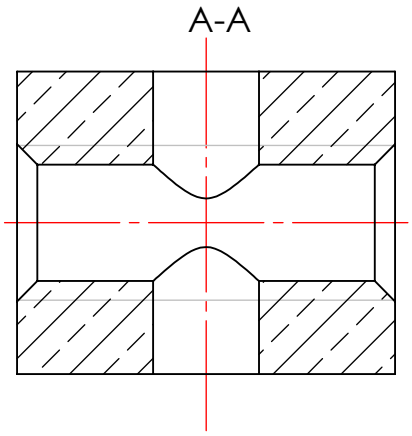

Rosca de Fuso ISO 2901/2903
(DIN 103)

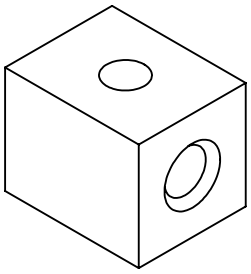

Ra 3,2

Raios não cotados : R=1
Chanfros não cotados : 1x45º

BELT DRIVE TEST RIG	Toleranciamento ISO 8015 Toleranciamentos gerais ISO 2768-mK Rugosidades gerais ISO 1302 Cantos e chanfors gerais ISO 13175	
DEmec FEUP		
Desenho nº	BDTR Item 75	Quantidade: 2

	NOME	DATA
DESENHOU	Pedro José de Freitas	25/06/2018
VERIFICOU		
APROVOU		

Porca de fuso GdL angular

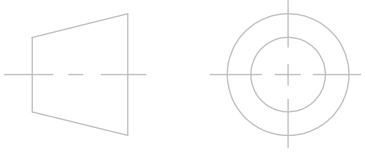

SCALE:1:1 | SHEET 1 OF 1 | A4

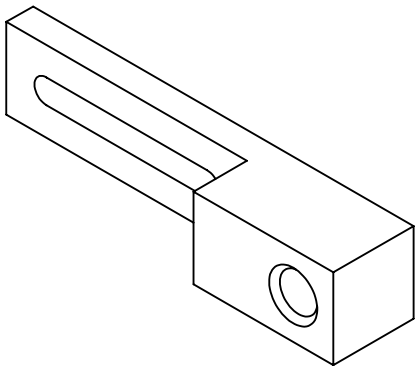

A-A

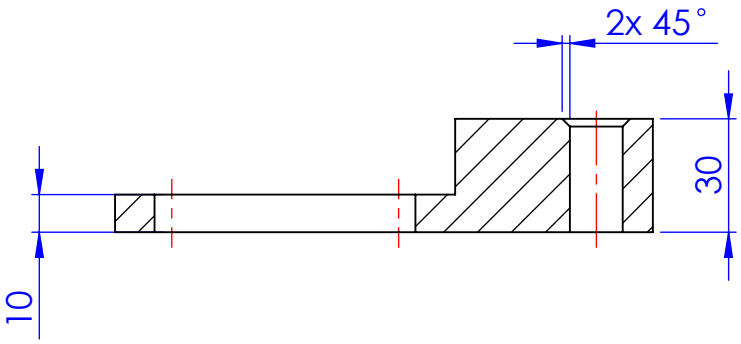

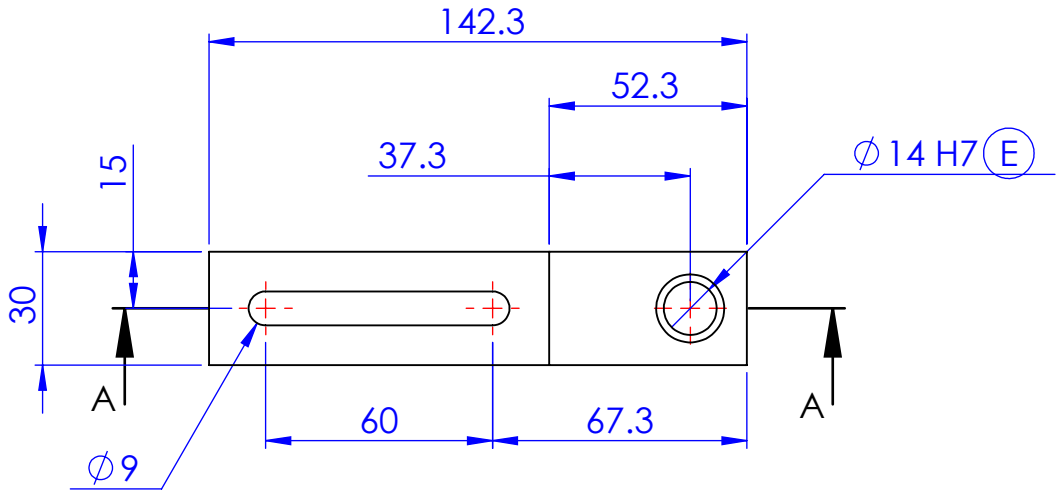

Ra 3,2

Raios não cotados : R=1
Chanfros não cotados : 1x45°

BELT DRIVE TEST RIG	Toleranciamento ISO 8015 Toleranciamentos gerais ISO 2768-mK Rugosidades gerais ISO 1302 Cantos e chanfors gerais ISO 13175	
DEmec FEUP		
Desenho nº	BDTR Item 30	Quantidade: 1

Suporte fuso entreixo

	NOME	DATA
DESENHOU	Pedro José de Freitas	25/06/2018
VERIFICOU		
APROVOU		

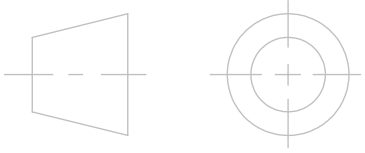

SCALE:1:2 | SHEET 1 OF 1 | A4

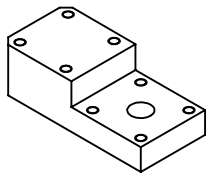

SECTION A-A

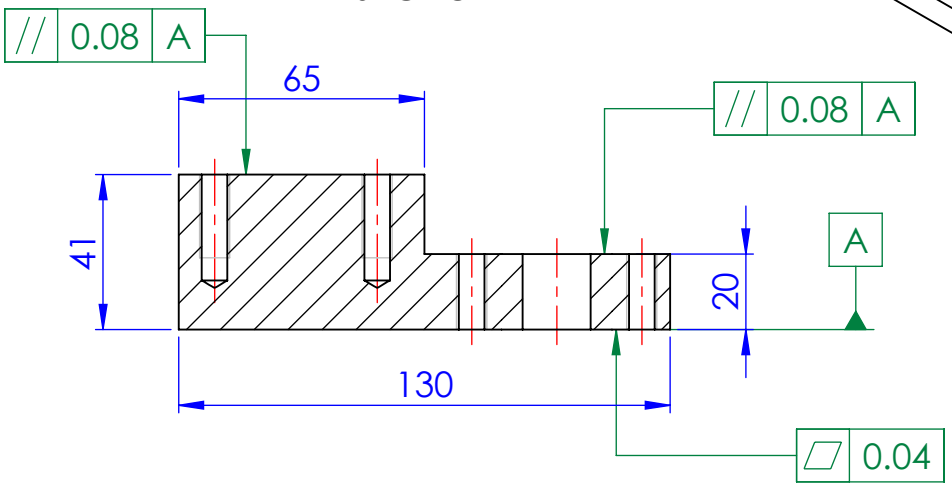

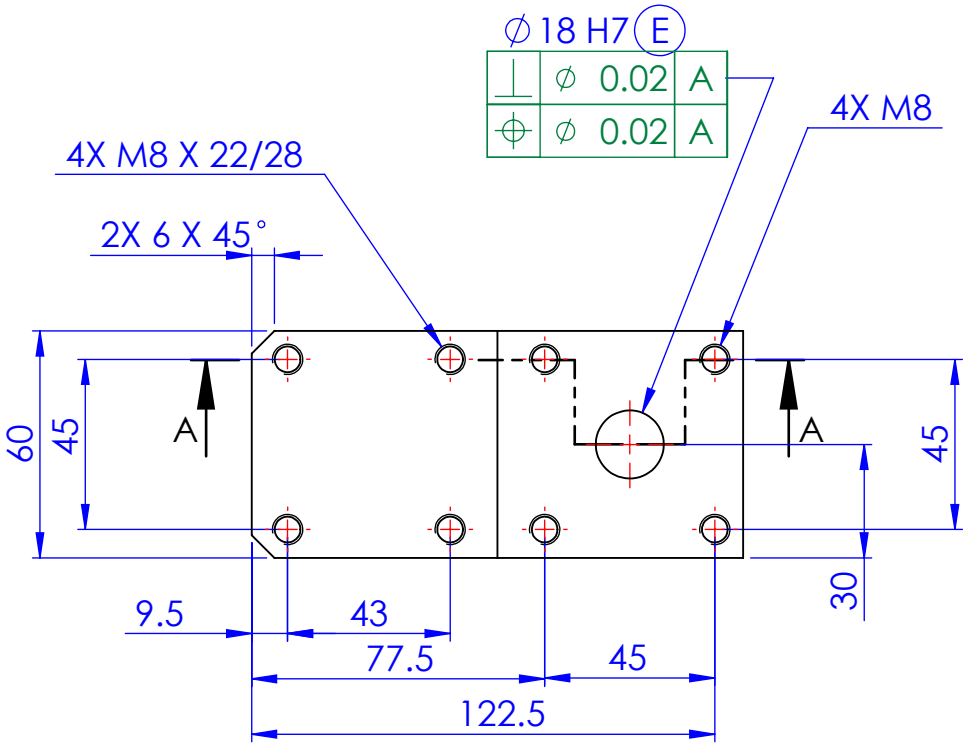

Ra 3,2

Raios não cotados : R=1

Chanfros não cotados : 1x45º

BELT DRIVE TEST RIG	Toleranciamento ISO 8015 Toleranciamentos gerais ISO 2768-mK Rugosidades gerais ISO 1302 Cantos e chanfors gerais ISO 13175	
DEmec FEUP		
Desenho nº	BDTR Item 45	Quantidade: 2

	NOME	DATA
DESENHOU	Pedro José de Freitas	25/06/2018
VERIFICOU		
APROVOU		

Suporte pino

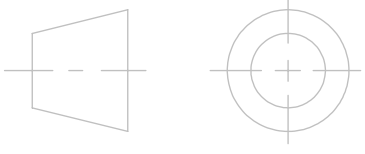

SCALE:1:2 | SHEET 1 OF 1 | A4

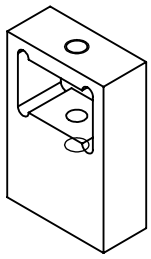

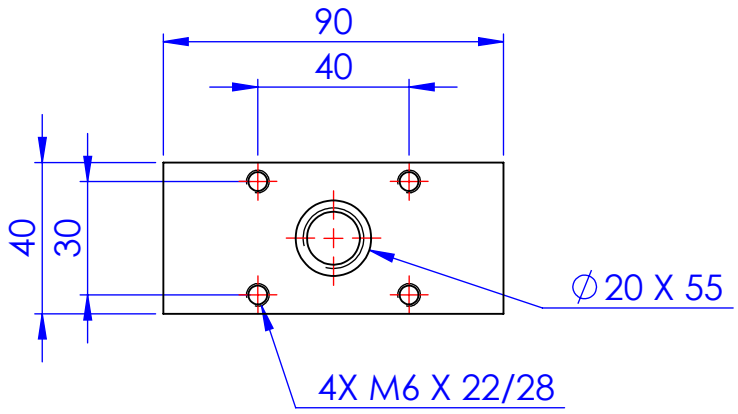

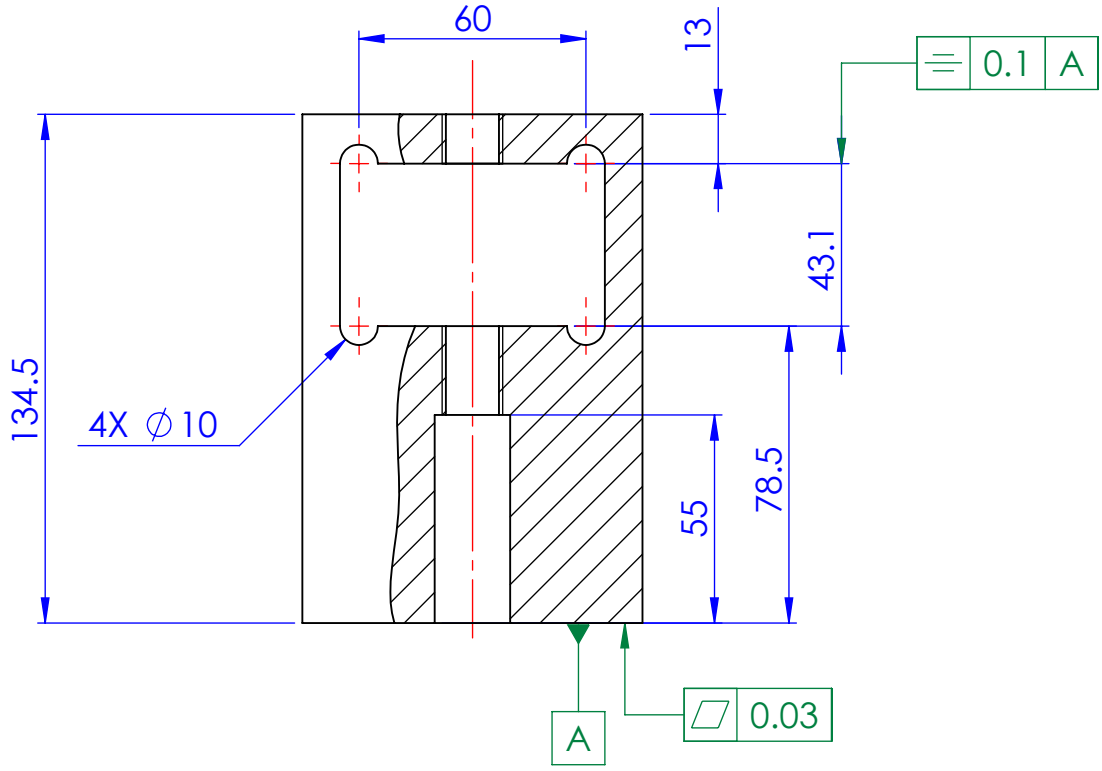

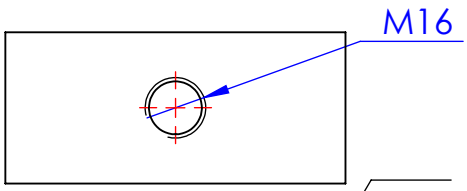

Ra 3,2

Raios não cotados : R=1
Chanfros não cotados : 1x45º

BELT DRIVE TEST RIG	Toleranciamento ISO 8015 Toleranciamentos gerais ISO 2768-mK Rugosidades gerais ISO 1302 Cantos e chanfors gerais ISO 13175	
DEmec FEUP		
Desenho nº	BDTR Item 69	Quantidade: 2

	NOME	DATA
DESENHOU	Pedro José de Freitas	25/06/2018
VERIFICOU		
APROVOU		

Suporte fuso angular

SCALE:1:2 | SHEET 1 OF 1 | A4

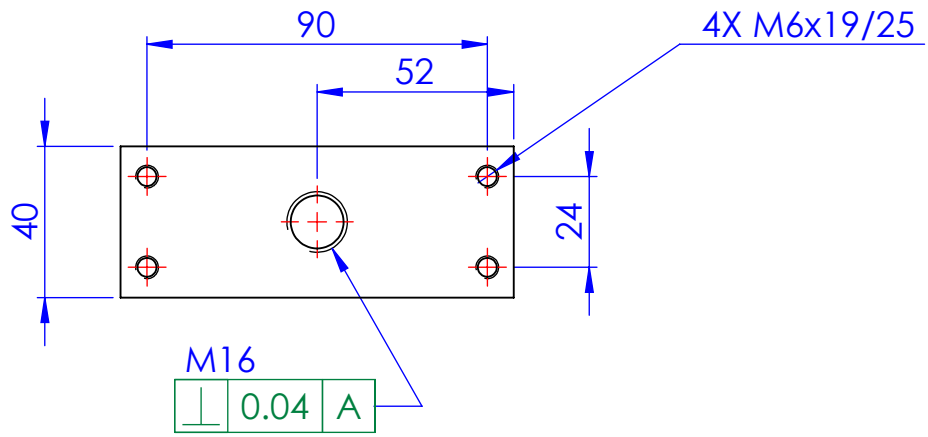

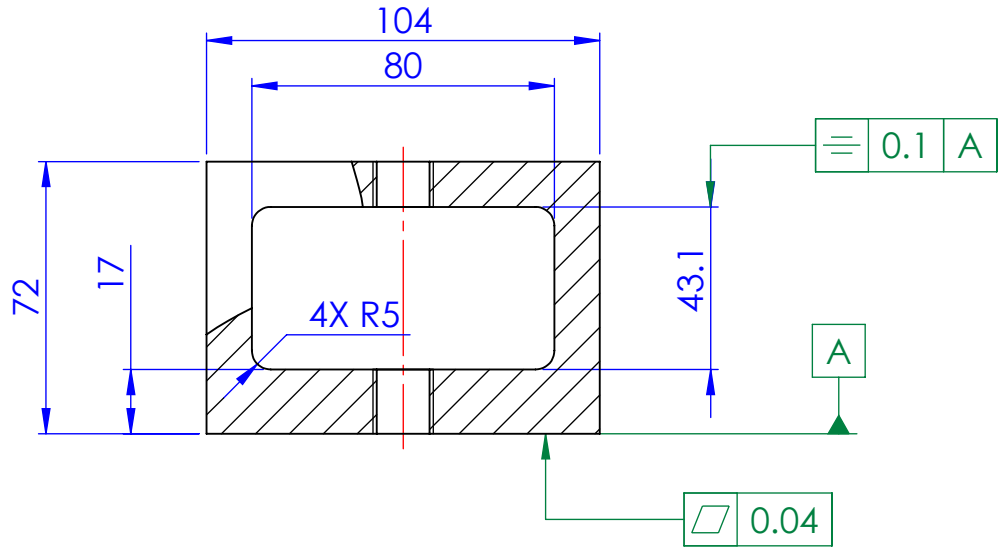

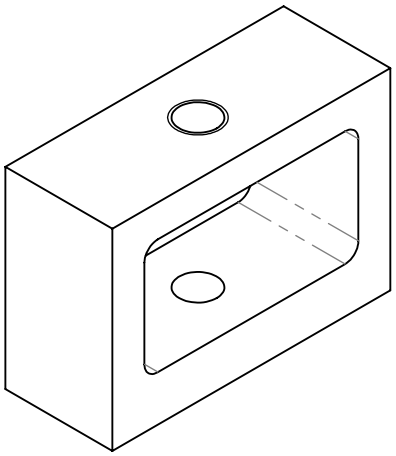

Ra 3,2

Raios não cotados : R=1
Chanfros não cotados : 1x45°

BELT DRIVE TEST RIG	Toleranciamento ISO 8015 Toleranciamentos gerais ISO 2768-mK Rugosidades gerais ISO 1302 Cantos e chanfors gerais ISO 13175	
DEmec FEUP		
Desenho nº	BDTR Item 60	Quantidade: 2

	NOME	DATA
DESENHOU	Pedro José de Freitas	25/06/2018
VERIFICOU		
APROVOU		

Suporte porca GdL angular

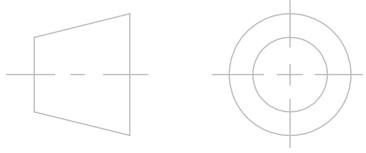

SCALE:1:2 | SHEET 1 OF 1 | A4

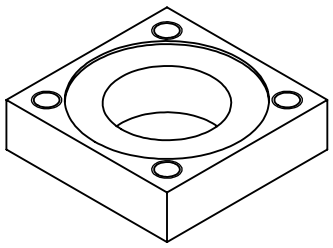

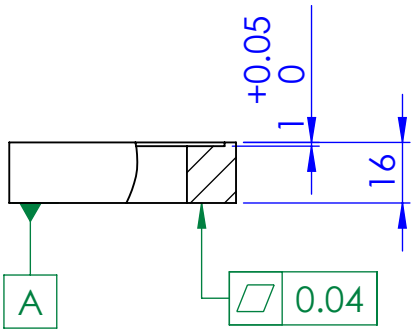

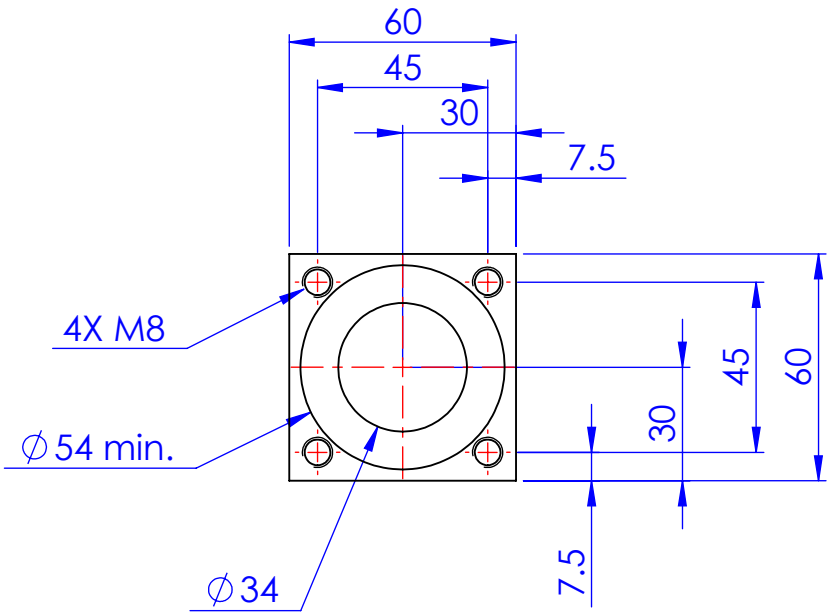

Raios não cotados : R=1
Ra 3,2 Chanfros não cotados : 1x45º

BELT DRIVE TEST RIG	Toleranciamento ISO 8015 Toleranciamentos gerais ISO 2768-mK Rugosidades gerais ISO 1302 Cantos e chanfors gerais ISO 13175	
DEmec FEUP		
Desenho nº	BDTR Item 49	Quantidade: 10

Suporte chumaceira plana

	NOME	DATA
DESENHOU	Pedro José de Freitas	25/06/2018
VERIFICOU		
APROVOU		

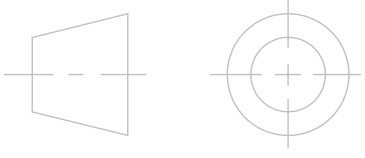

SCALE:1:2 | SHEET 1 OF 1 | A4

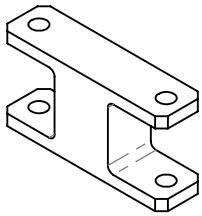

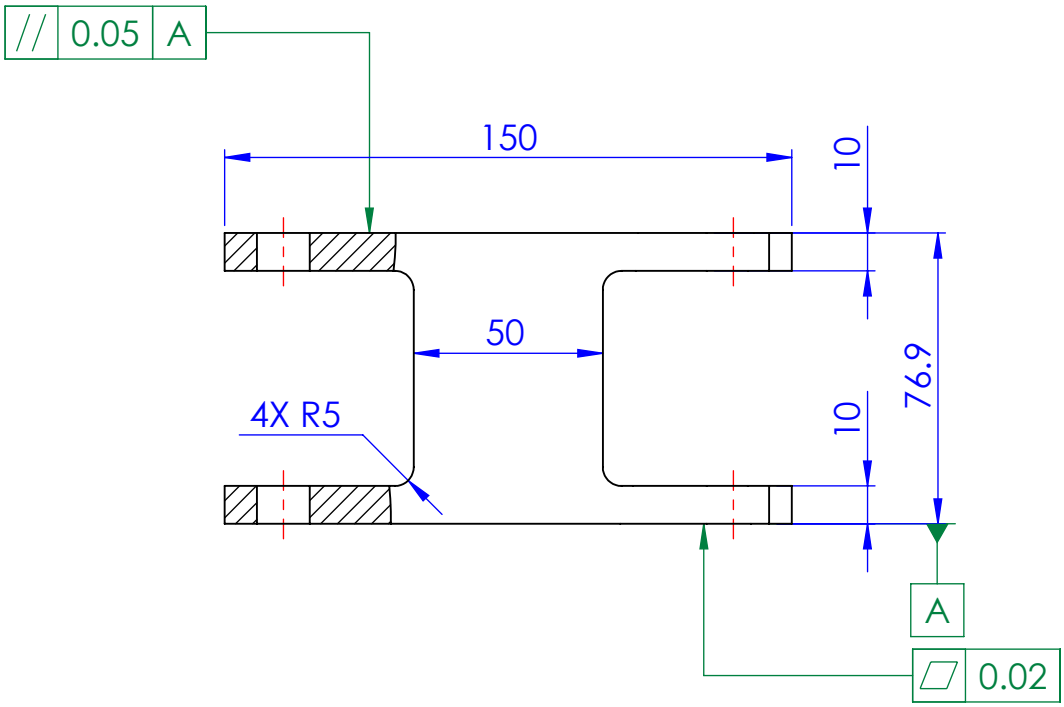

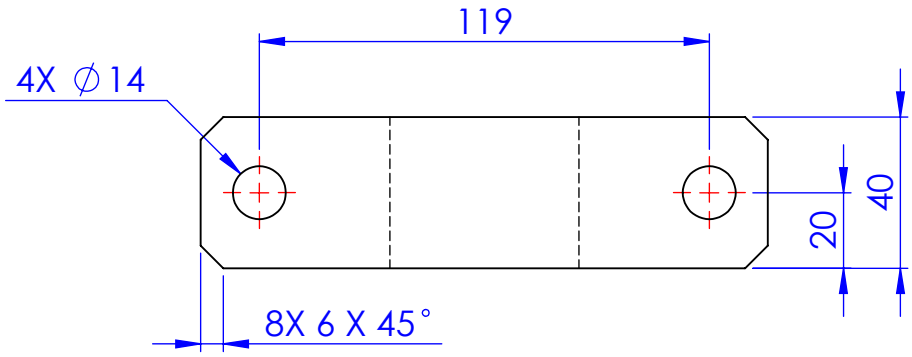

Ra 3,2

Raios não cotados : R=1

Chanfros não cotados : 1x45º

BELT DRIVE TEST RIG	Toleranciamento ISO 8015 Toleranciamentos gerais ISO 2768-mK Rugosidades gerais ISO 1302 Cantos e chanfors gerais ISO 13175	
DEmec FEUP		
Desenho nº	BDTR Item 51	Quantidade: 4

	NOME	DATA
DESENHOU	Pedro José de Freitas	25/06/2018
VERIFICOU		
APROVOU		

Suporte chumaceira

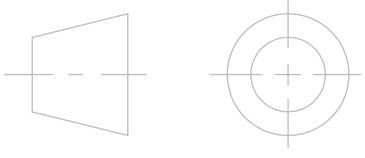

SCALE:1:2 | SHEET 1 OF 1 | A4

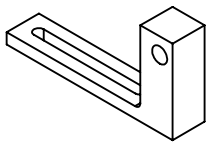

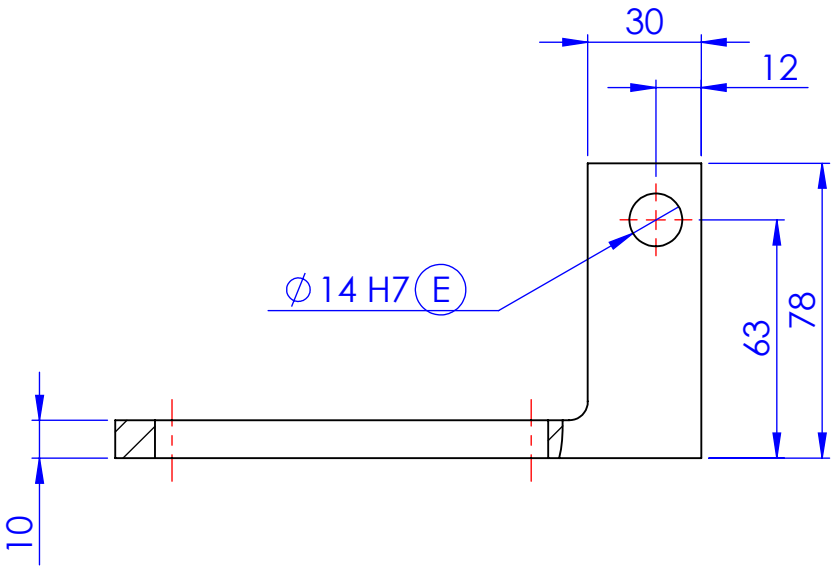

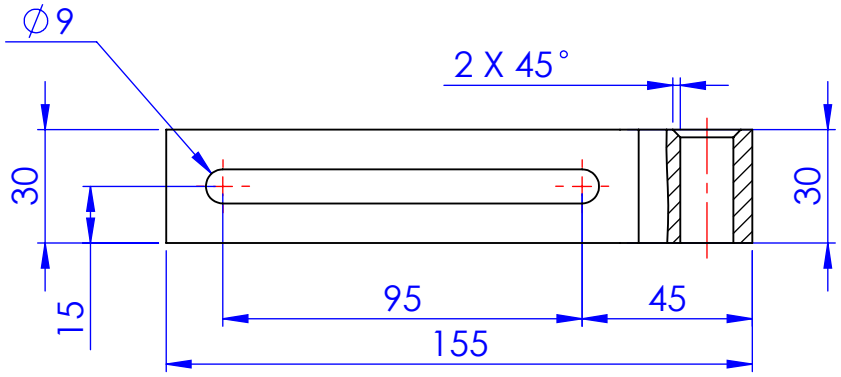

Ra 3,2

Raios não cotados : R=1

Chanfros não cotados : 1x45°

BELT DRIVE TEST RIG	Toleranciamento ISO 8015 Toleranciamentos gerais ISO 2768-mK Rugosidades gerais ISO 1302 Cantos e chanfors gerais ISO 13175	
DEmec FEUP		
Desenho nº	BDTR Item 39	Quantidade: 1

	NOME	DATA
DESENHOU	Pedro José de Freitas	25/06/2018
VERIFICOU		
APROVOU		

Suporte de fuso Axial offset

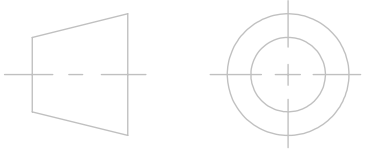

SCALE:1:2 | SHEET 1 OF 1 | A4

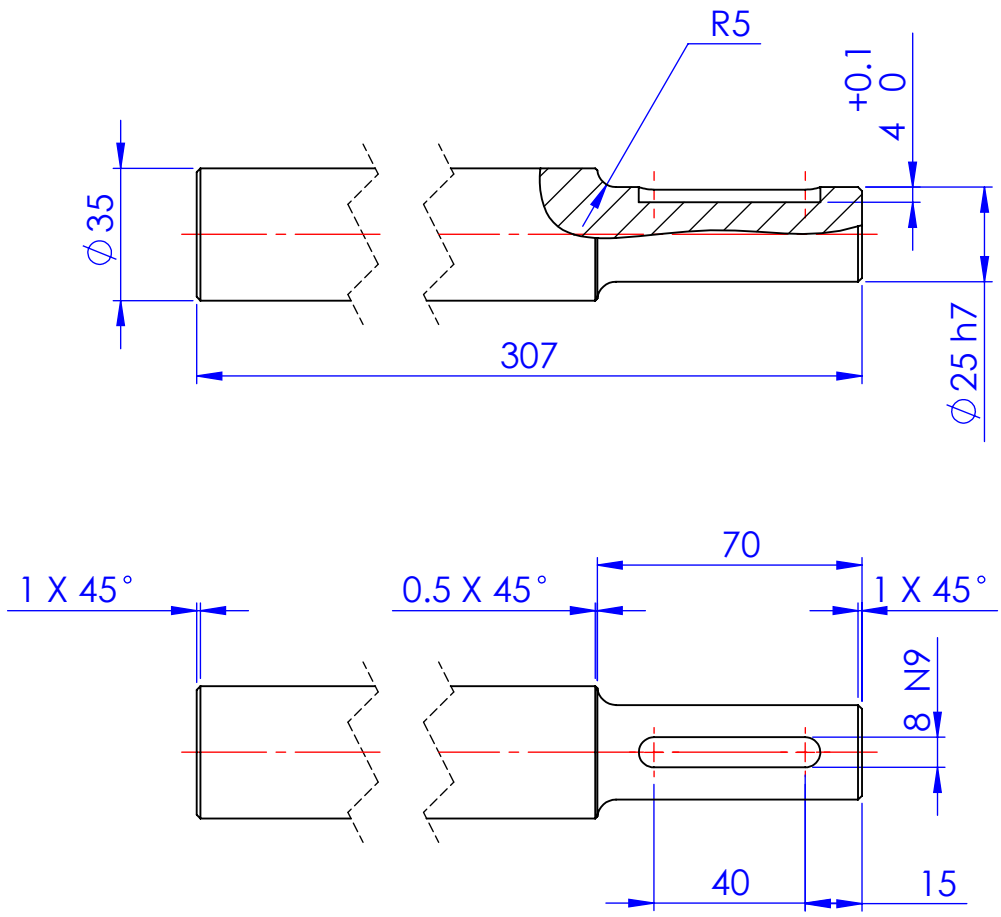

Ra 3,2

Raios não cotados : R=1
Chanfros não cotados : 1x45º

BELT DRIVE TEST RIG	Toleranciamento ISO 8015 Toleranciamentos gerais ISO 2768-mK Rugosidades gerais ISO 1302 Cantos e chanfors gerais ISO 13175	
DEmec FEUP		
Desenho nº	BDTR Item 59	Quantidade: 2

Veio

	NOME	DATA
DESENHOU	Pedro José de Freitas	25/06/2018
VERIFICOU		
APROVOU		

SCALE:1:5 | SHEET 1 OF 1 | A4

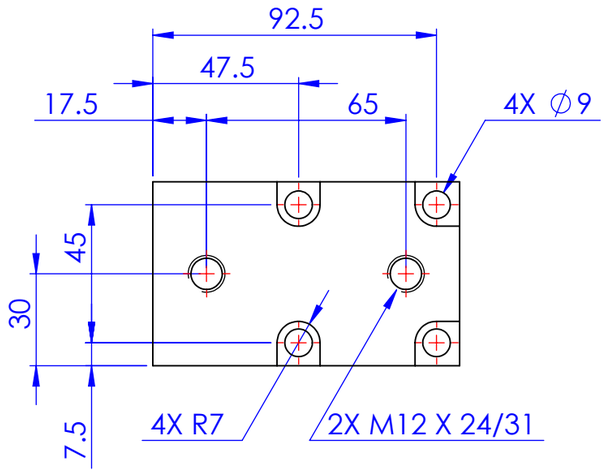

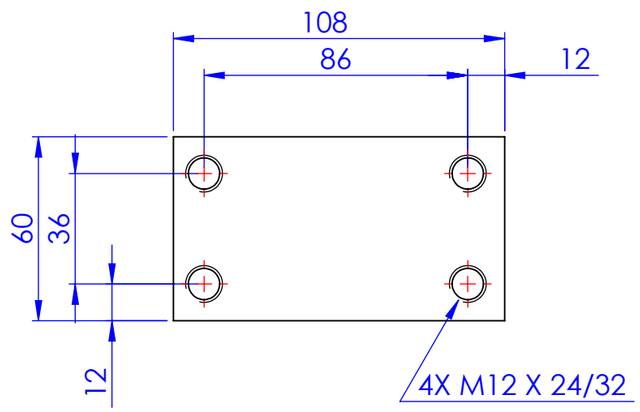

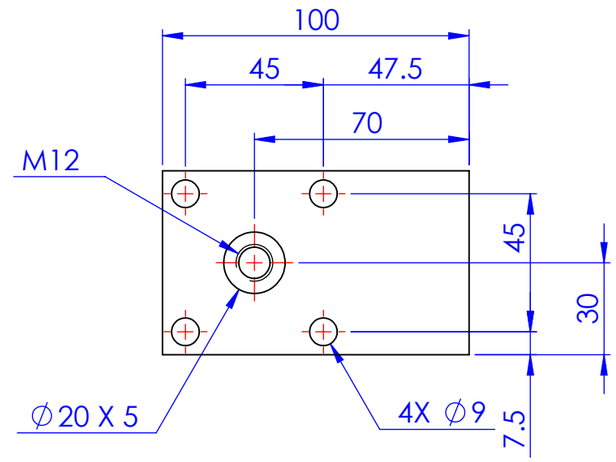

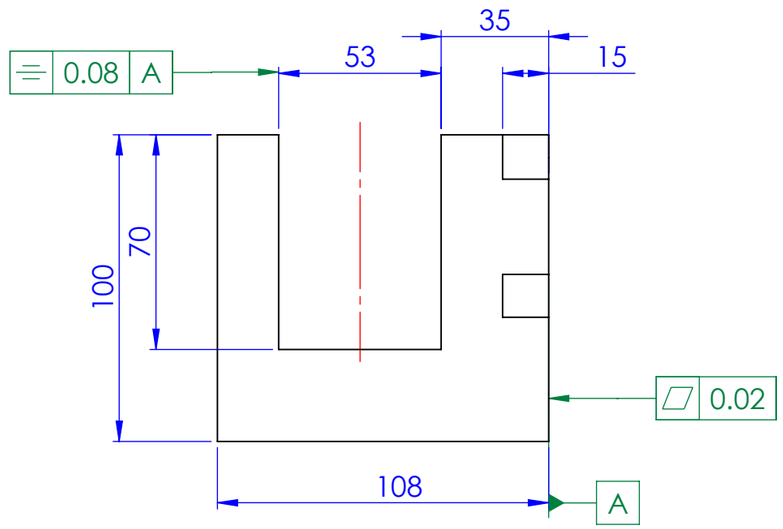

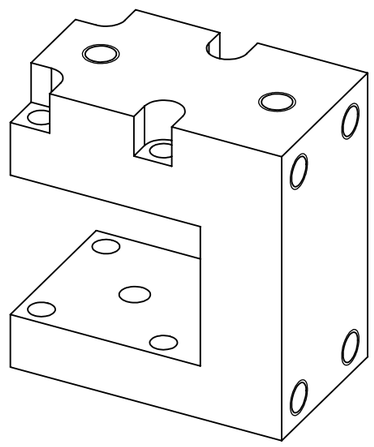

Raios não cotados : R=1
Chanfros não cotados : 1x45º
Ra 3,2

BELT DRIVE TEST RIG	Toleranciamento ISO 8015 Toleranciamentos gerais ISO 2768-mK Rugosidades gerais ISO 1302 Cantos e chanfors gerais ISO 13175	
DEmec FEUP		
Desenho nº	BDTR Item 68	Quantidade: 4

	NOME	DATA
DESENHOU	Pedro José de Freitas	25/06/2018
VERIFICOU		
APROVOU		

C de trás

SCALE:1:2 | SHEET 1 OF 1 | A3

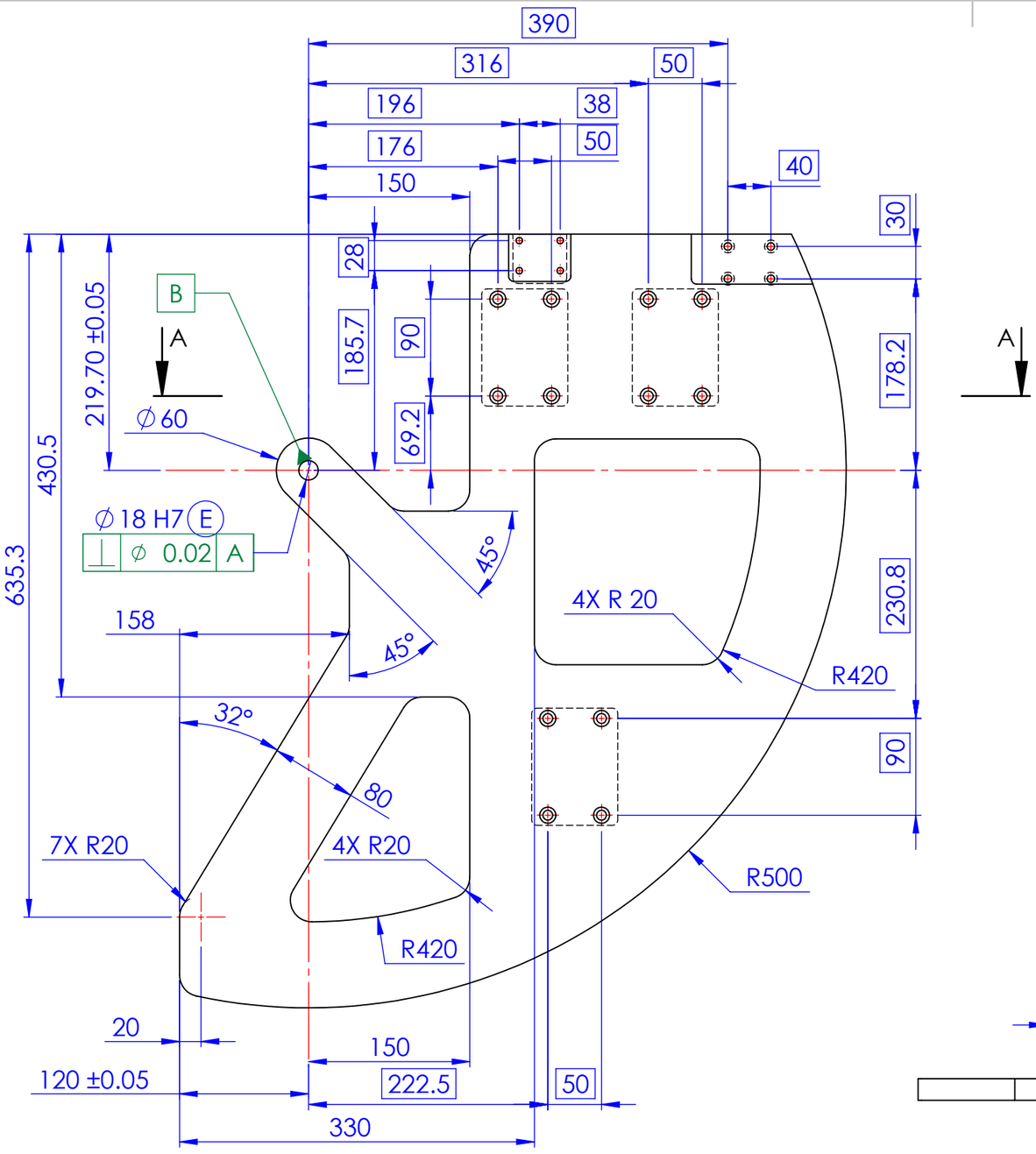

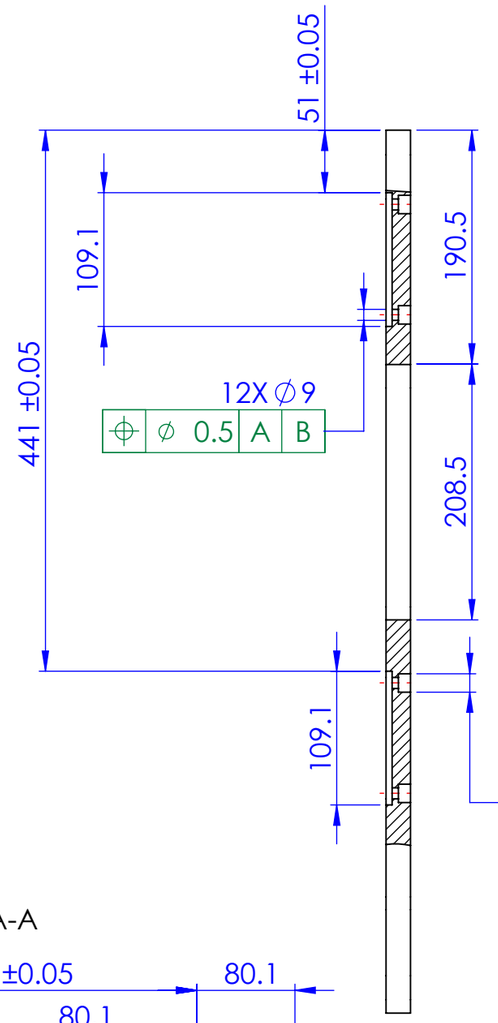

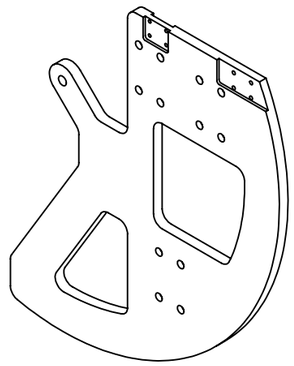

A-A

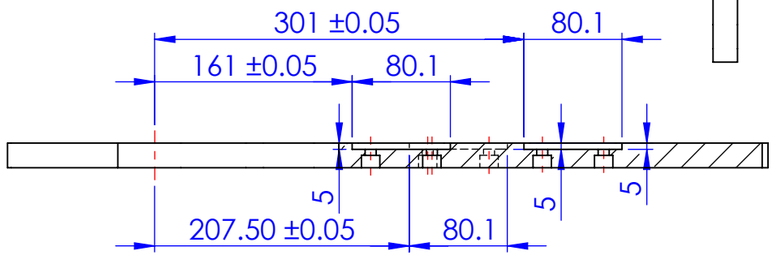

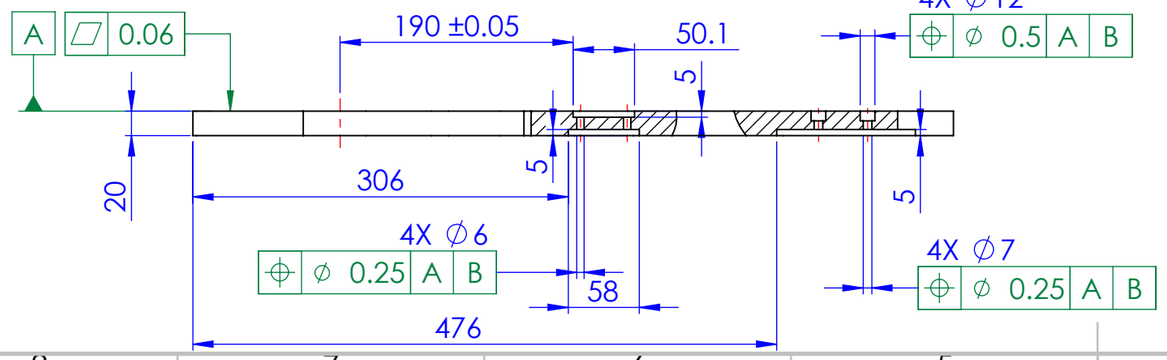

Ra 3,2

Raios não cotados : R=5
Chanfros não cotados : 1x45°

BELT DRIVE TEST RIG	Toleranciamento ISO 8015 Toleranciamentos gerais ISO 2768-mK Rugosidades gerais ISO 1302 Cantos e chanfors gerais ISO 13175	
DEmec FEUP		
Desenho nº	BDTR Item 38	Quantidade: 1

Base axial offset

	NOME	DATA
DESENHOU	Pedro José de Freitas	25/06/2018
VERIFICOU		
APROVOU		

SCALE:1:5 | SHEET 1 OF 1 | A3

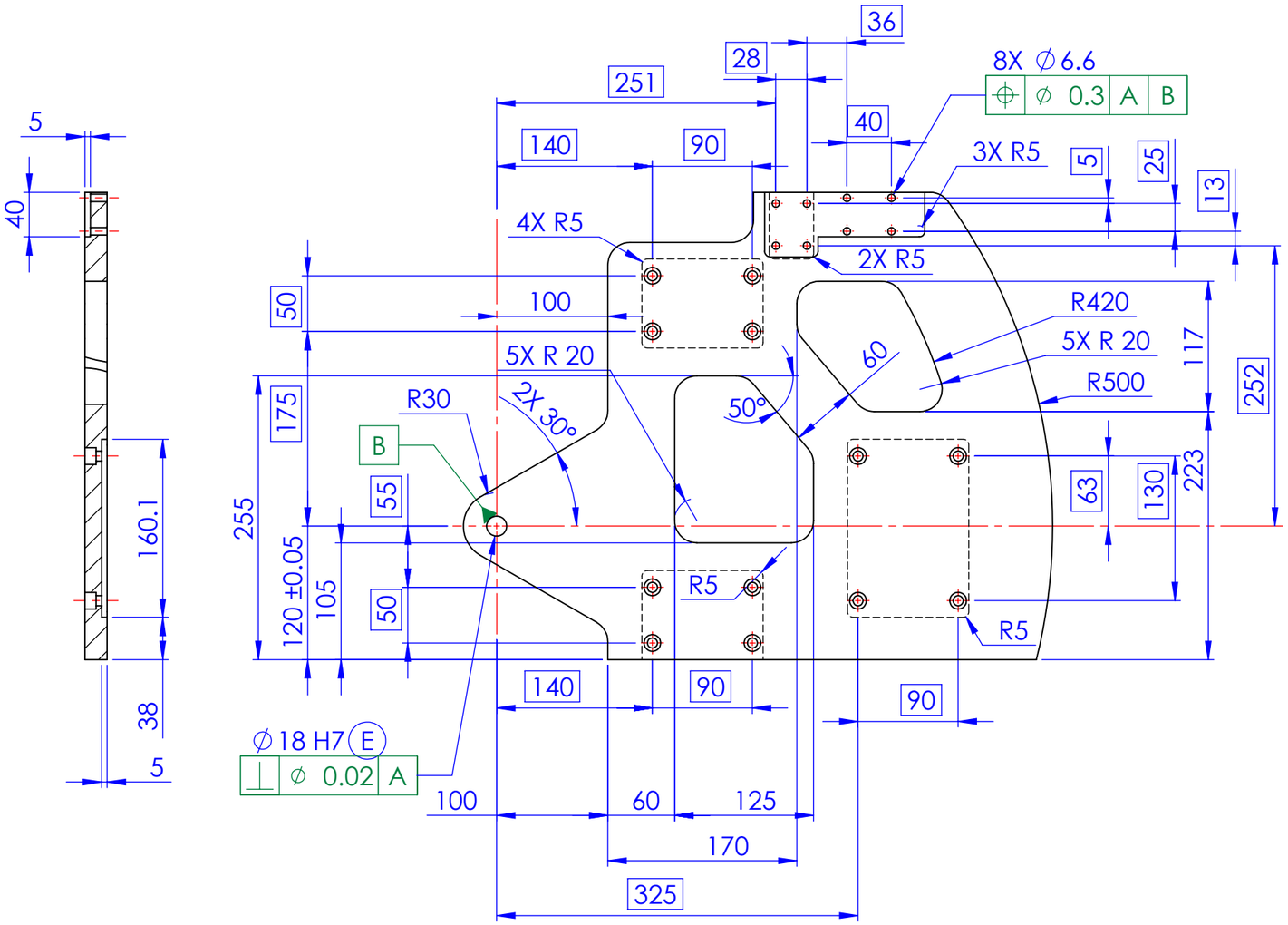

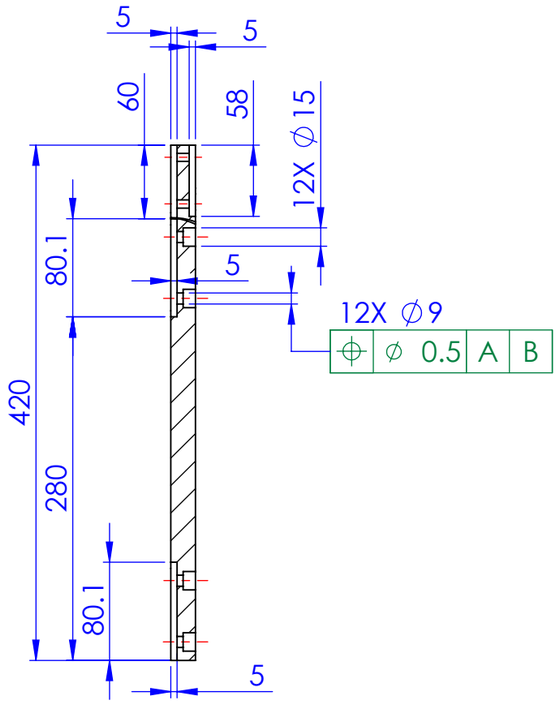

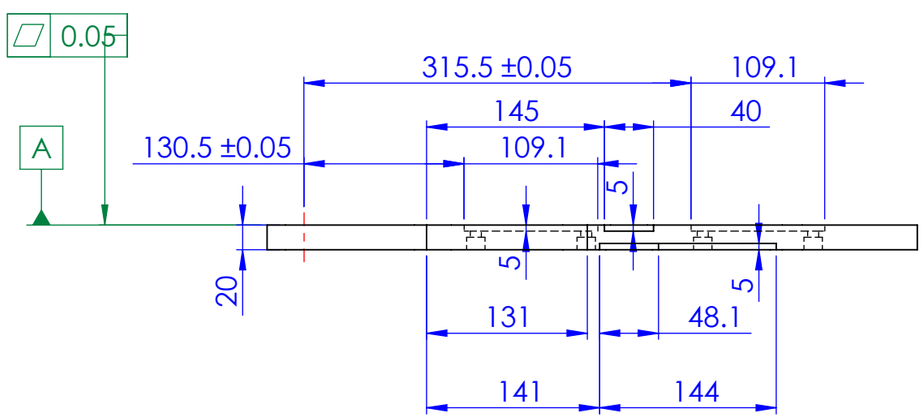

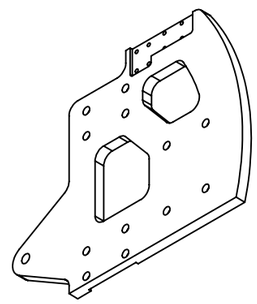

Ra 3,2

Raios não cotados : R=1
Chanfros não cotados : 1x45°

BELT DRIVE TEST RIG	Toleranciamento ISO 8015 Toleranciamentos gerais ISO 2768-mK Rugosidades gerais ISO 1302 Cantos e chanfors gerais ISO 13175	
DEmec FEUP		
Desenho nº	BDTR Item 15	Quantidade: 2

Base enteixo

	NOME	DATA
DESENHOU	Pedro José de Freitas	25/06/2018
VERIFICOU		
APROVOU		

SCALE:1:5 | SHEET 1 OF 1 | A3

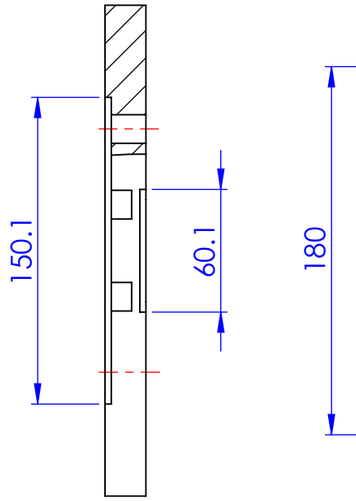

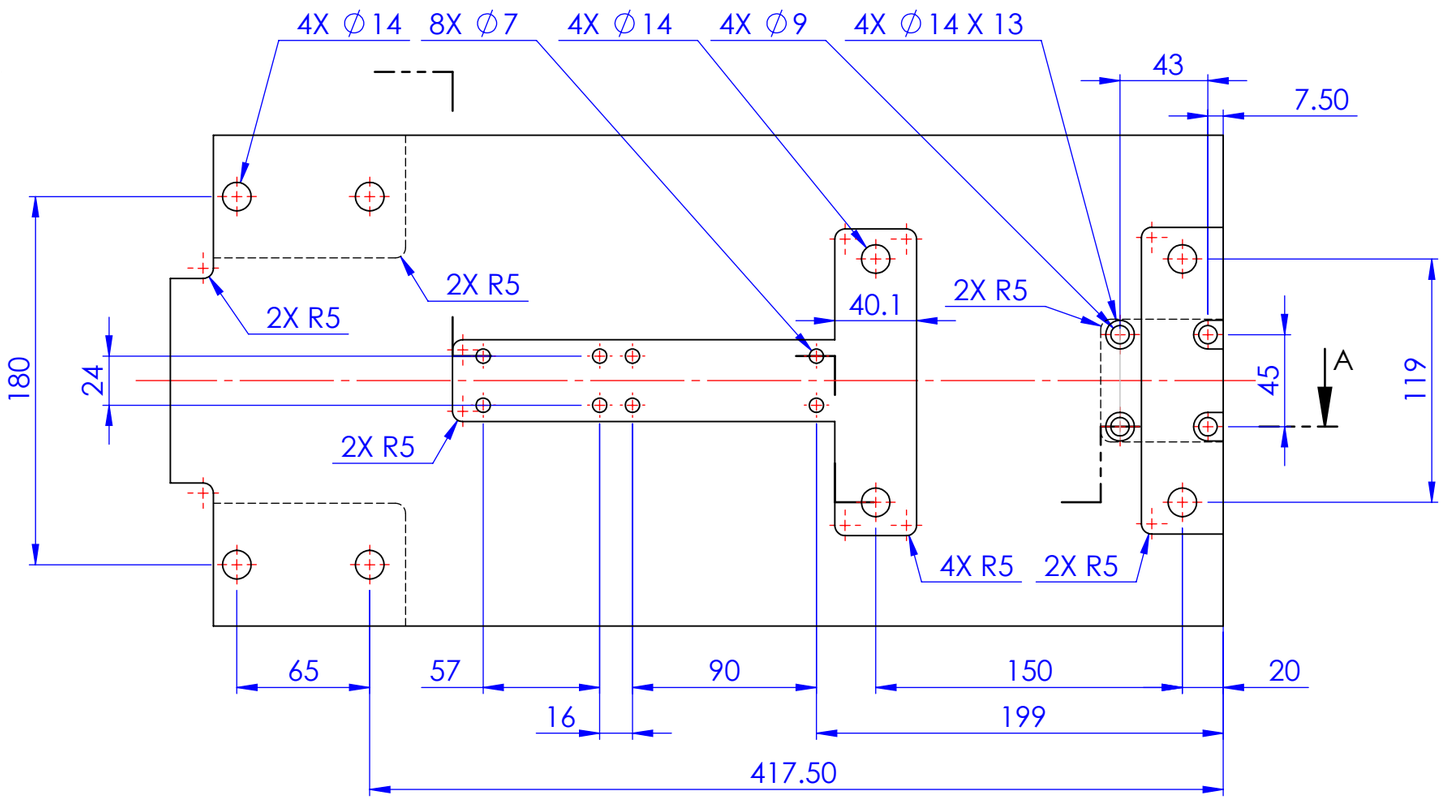

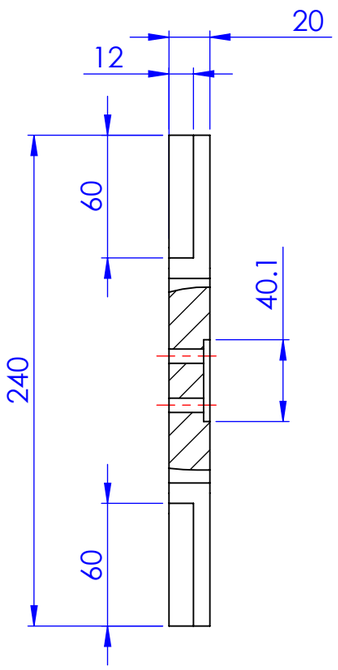

A-A

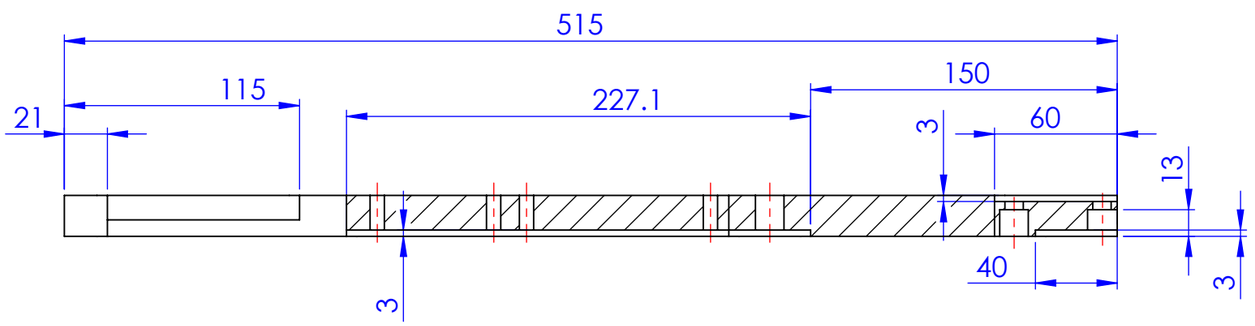

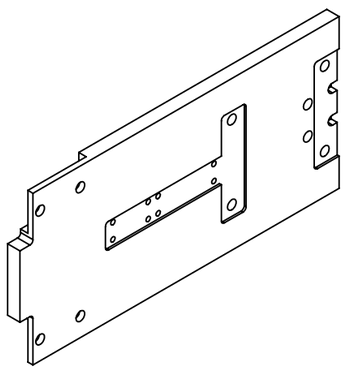

Ra 3,2

Raios não cotados : R=1
Chanfros não cotados : 1x45º

BELT DRIVE TEST RIG	Toleranciamento ISO 8015 Toleranciamentos gerais ISO 2768-mK Rugosidades gerais ISO 1302 Cantos e chanfors gerais ISO 13175	
DEmec FEUP		
Desenho nº	BDTR Item 52	Quantidade: 2

	NOME	DATA
DESENHOU	Pedro José de Freitas	25/06/2018
VERIFICOU		
APROVOU		

Base angular

SCALE:1:3 | SHEET 1 OF 1 | A3